January-March 2025 Vol. 39 No. 1 ISSN 0970-5953

Physics Education

Quarterly e-Journal Devoted to Physics Pedagogy

Navigating the Intersections of Physics Education and Innovation

www.physedn.in www.indapt.org.in

Volume 39, Number 1

In this Issue:

Editorial

Navigating the Intersections of Physics Education and Innovation

Welcome to the first issue of Physics Education in 2025—a fresh beginning in our shared pursuit of nurturing minds, questioning assumptions, and unlocking the wonders of nature through the lens of physics.

As the discipline continues to grow in complexity and relevance, this journal embraces its role as a platform where educators and learners alike can explore the edges of knowledge and pedagogy. Our contributors this quarter exemplify this spirit of exploration, presenting articles that blend theoretical depth with practical teaching relevance:

Semi-Magic Numbers from Sub-shell Closures in Shell Model Energy Levels: Shikha Awasthi, O.S.K.S Sastri & Vandna Luthra

This article offers a compelling exploration of nuclear structure, illuminating how subshell closures lead to the emergence of semi-magic numbers. The findings not only expand theoretical physics but also offer fresh classroom narratives about nuclear stability and shell model symmetry.

Gravity in Undergraduate Thermal Physics Courses: Kartik Tiwari

Tiwari's contribution challenges conventional curriculum boundaries by integrating gravity into thermal physics discussions. By highlighting gravitational influence on thermodynamic systems—often overlooked at the undergraduate level—it opens pedagogical avenues that foster deeper interdisciplinary engagement.

SOL-GEL: A Simple Method of Thin Film Deposition and Nano-particle Growth: Sharmistha Lahiry

With lucid exposition and rich context, Lahiry brings the sol-gel technique into focus—a gateway to hands-on experimentation in materials science. The work strikes a balance

between theoretical grounding and experimental accessibility, making it especially valuable for physics educators venturing into nanoscience.

Some Applications of Lorentz Oscillator Model: Vishwamittar

This article revisits the Lorentz oscillator model with renewed vigor, detailing its applications in fields ranging from optics to quantum electronics. Its clarity and instructional value make it a standout resource for educators seeking to link historical models with contemporary insights.

Looking Beyond the Pages

As educators, researchers, and students continue to push boundaries and challenge norms, Physics Education is proud to offer a canvas for ideas that empower and enlighten. Whether you're in a classroom, a lab, or simply curious about the nature of things, this issue is an invitation to expand your horizons, question deeply, and teach boldly.

Let us make 2025 a year where physics doesn't just describe the universe—but helps us understand our place in it.

Prof. OSKS Sastri
Chief Editor
Physics Education (IAPT)

Semi-magic Numbers from Sub-shell Closures in Shell Model Energy Levels

Shikha Awasthi[1], O.S.K.S Sastri[1] & Vandna Luthra[2]

[1]Department of Physical and Astronomical Sciences
Central University of Himachal Pradesh, HP 176215, Bharat(India)
[2]Department of Physics, Gargi College, Delhi University, Bharat(India)
[1]sastri.osks@hpcu.ac.in

Submitted on January 25, 2025

Abstract

The magic numbers associated with shell closures at the β-stability line are a well-established concept. The experimental observation of highly neutron-rich nuclei, such as ^{24}O, ^{42}Si, and ^{54}Ca, exhibiting remarkable stability has inspired a search for new magic and semi-magic numbers based on sub-shell closures. The purpose of this work is to guide graduate-level students in analyzing possible sub-shell closures that could result in magic and semi-magic numbers [1], based on the single-particle energy states of the nuclear shell model. The analysis focuses on doubly magic nuclei near the β-stability line, ranging from $^{16}_{8}$O to $^{310}_{126}$X, by classifying them into various categories-light, medium, heavy, and super-heavy nuclei; to deduce potential magic and semi-magic numbers for neutron number (N) and proton number (Z) [2]. The stability of nuclei with $N = 14, 34, 40$ and $Z = 14, 34$ has been confirmed, while nuclei with $N = 6, 16, 18, 32, 58, 64, 92, 100, 136, 164$, and 172, as well as $Z = 18, 58$, and 76, are predicted to exhibit stability. This analysis is particularly helpful for undergraduate (UG) students to understand why gaps exist between energy levels according to the single-particle shell model scheme.

Keywords: Magic and Semi-magic numbers, Doubly magic nuclei, Shell model, Central Divided Difference (CDD) Method, Gnumeric.

1 Introduction

It is a well-known fact that the atomic nuclei exhibit similar shell structure as that of atomic shells with neutrons and protons forming the shells. These discrete shells are the quantum states of neutrons and protons which are most important in understand-

ing the structure of a nucleus. The large gaps between these single particle energy states exists when there is a shell closure at N or Z equal to 2, 8, 20, 28, 50, 82, 126 and 184 (for neutrons only) i.e the so called 'magic numbers'. The nuclei which have either proton or neutron equal to magic number are known as 'magic nuclei' and the nuclei which have both proton and neutron equal to magic number are known as 'doubly magic nuclei'. Due to the shell gaps in energy states for filled shells at different magic numbers, the nucleons are more tightly bound to the nucleus causing extra stability to the nucleus as compared to the adjacent nuclei [3]. Also magic nuclei are less deformed as compared to their neighbouring nuclei. This results in abundance of elements with neutron number (N) = magic number. But in recent years, the studies have revealed that in some cases the usual shell closures disappear and the new shell closures appear [4], [5]. The appearance and disappearance of these Magic numbers may depend on different mass regions under consideration. The discovery of new magic numbers [6] may help in deciding the existence limit of Superheavy nuclei [7]. Many Magic and Semi-Magic numbers are predicted theoretically [ptu] and experimentally e.g ${}^{24}_{8}O$, ${}^{42}_{16}Si$, ${}^{54}_{20}Ca$ etc. [8, 9, 10] by many groups using separation energy plots, pairing energy plots, binding energy investigations and by using different methods such as Hartree-Fock-Bogoliubov methods [11].

The syllabus of graduate level [12, 13, 14] includes Nuclear Shell model and magic numbers, but it will be easy for students to grasp the essence of how energy levels of different nuclei are formed and how are magic numbers obtained from them. In this work, we are trying to deduce magic and semi-magic numbers using single particle energy states of neutron and proton [1] for doubly magic nuclei from ${}^{16}_{8}O$ to ${}^{310}_{126}X$ in quite an easy manner which is within the approach of graduate level students. This will provide a better understanding for graduate level students about how the single particle energy levels are formed within a nucleus according to nuclear Shell model and also how the magic numbers can be realised from them. Neutron and proton single-particle energy states were determined by solving the time-independent Schrödinger equation, with the Woods-Saxon potential [15] serving as the mean-field. The obtained energy states for neutrons and protons are used to predict the Magic and Semi-Magic numbers by calculating the gaps between the states. The Shell model [3] is very effective model to obtain the ground state energies for all nuclei. The motivation behind this work is how many Magic and Semi-Magic numbers can be deduced by using the single particle energy states for various neutron number (N) and proton number (Z).

In the following section, we present a brief overview of the simulation methodology proposed by D. Hestenes [16], which utilizes the numerical matrix diagonalization technique [17] to determine the single-particle

energy states of neutrons and protons in doubly magic nuclei [18]. Section 3 provides the simulation results along with a detailed discussion. Finally, Section 4 summarizes our conclusions.

2 Simulation Methodology

2.1 Modeling the interaction using Woods-Saxon (WS)potential:

The interaction between nucleons is modelled using a mean field potential i.e Woods-Saxon potential or a simple rounded square well potential. The Woods-Saxon potential is able to predict some magic numbers, but inclusion of Spin-orbit potential is necessary to obtain the entire magic numbers. The Spin-orbit potential is proportional to the derivative of the mean field potential.

The modeling aids in the reduction of the two-body problem to a one-body problem, with the reduced mass of the system acquired as a bound state of the central potential, which is best expressed in spherical polar co-ordinates. The central equation governing the dynamics at the microscopic domain is the Time-Dependent Schrödinger Equation (TDSE) which through separation of variables in and t results in Time-Independent Schrödinger Equation (TISE) [18]. The radial equation governing the system for $\ell = 0$ is given by

$$-\frac{\hbar^2}{2\mu}\frac{d^2u(r)}{dr^2} + V_{eff}(r)u(r) = Eu(r) \qquad (1)$$

Now the effective potential experienced by a neutron or a proton is given by:

$$V_{eff}(r)u(r) = V_{cf}(r) + V_i(r) \qquad (2)$$

Where, $V_{cf}(r)$ is the centrifugal potential given by:

$$V_{cf}(r) = \frac{\ell(\ell+1)\hbar^2c^2}{2\mu c^2 r^2} \qquad (3)$$

Here, μ denotes the reduced mass [1], which varies between the neutron and the proton. The constant $\hbar c$ has a value of 197.327 MeV-fm.

$$\mu = \begin{cases} \frac{m_n \times (Z \times m_p + (N-1) \times m_n)}{(Z \times m_p + N \times m_n)}, & \text{for neutron} \\ \frac{m_p \times ((Z-1) \times m_p + N \times m_n)}{(Z \times m_p + N \times m_n)}, & \text{for proton} \end{cases} \qquad (4)$$

Here, $m_p = 938.272$ and $m_n = 939.565$ are masses of proton and neutron respectively, in units of MeV/c^2. $V_i(r)$ is the net interaction potential; for a neutron, $V_n(r)$ and a proton, $V_p(r)$ respectively given as:

$$V_n(r) = V_{WS}(r) + V_{\ell s}(r) \qquad (5)$$

$$V_p(r) = V_{WS}(r) + V_{\ell s}(r) + V_C(r) \qquad (6)$$

The mean-field potential is modeled as [1]:

- Woods-Saxon potential (rounded square-well potential) given by

$$V_{WS}(r) = \frac{V_0}{1 + \exp\left(\frac{r-R}{a}\right)} \qquad (7)$$

where V_0 is the depth of the well.

$$V_0 = \begin{cases} -51 + 33((N-Z)/A)\ MeV, \\ \qquad\qquad \text{for neutrons} \\ -51 - 33((N-Z)/A)\ MeV, \\ \qquad\qquad \text{for protons} \end{cases} \qquad (8)$$

Where, $R = R_0 A^{1/3}$ ($R_0 = 1.28$) is the radius of the nucleus, a is surface diffuseness parameter (taken = 0.66) [19]

- The Spin-orbit potential is given by

$$V_{ls}(r) = V_1 \left(\frac{r_0}{\hbar}\right)^2 \frac{1}{r}\frac{d}{dr}\left[\frac{1}{1+\exp\left(\frac{r-R}{a}\right)}\right] \textbf{(L.S)} \quad (9)$$

Here, the spin-orbit coupling term is given by $\mathbf{L}\cdot\mathbf{S} = [j(j+1) - \ell(\ell+1) - 3/4], \hbar^2$, where ℓ is the orbital angular momentum quantum number, $j = \ell + s$ represents the total angular momentum quantum number and s is spin angular momentum quantum number (= 1/2 for nucleons). V_1 and r_0 ($V_1 = -0.44V_0$ and $r_0 = 0.90$ [1]) are the proportionality constants.

For protons, the Coulomb interaction is included given by:

$$V_c(r) = \begin{cases} \frac{(Z-1)e^2}{4\pi\epsilon_0 r}, & \text{for } r \geq R_c \\ \frac{(Z-1)e^2}{4\pi\epsilon_0 R_c}\left[\frac{3}{2} - \frac{r^2}{2R_c^2}\right], & \text{for } r \leq R_c \end{cases} \quad (10)$$

Here, R_c denotes the nuclear charge radius, which is assumed to be $\approx$ radius of the nucleus. This potential is multiplied and divided by electron rest mass energy, $m_e c^2 = 0.511\ MeV$ to rephrase it in MeV units. The rephrased potential is given by:

$$V_c(r) = \begin{cases} \frac{(Z-1)*2.839*0.511}{r}, & \text{for } r \geq R_c \\ \frac{(Z-1)*2.839*0.511}{R_c}\left[\frac{3}{2} - \frac{r^2}{2R_c^2}\right], & \text{for } r \leq R_c \end{cases} \quad (11)$$

Equation 1 represents the Time-Independent Schrödinger Equation in the form of an eigenvalue problem, $Hu(r) = Eu(r)$, where H denotes the Hamiltonian operator. The radial wave function $u(r)$ must satisfy the boundary condition $u(0) = 0$ and decay to zero as $r \to \infty$ to ensure it is properly normalized.

2.2 Numerical Technique used :

When deciding to choose a numerical technique for implementaion, there are three crucial factors to consider i.e stability, accuracy, and efficiency. The choice of these techniques also depends on computational efforts and computational time required. In current work, we chose to work with Central divided difference technique (CDD). Due to the truncation of Taylor series to two terms, the accuracy of CDD method is of order $O(h^4)$. CDD method is the simplest and most appealing matrix diagonalisation method which can be easily implemented by students in computer.

So, the main idea behind choosing CDD technique is that we want these calculations accessible to UG level students. Working in free open source software (FOSS) like Gnumeric worksheets is a best way to make students understand the problem easily [20]. Also Gnumeric has an additional advantage as compared to other worksheet environments, to obtain eigen values by giving a simple formula '$eigen()$'.

Unlike other numerical techniques like Matrix Methods (MM) [17] using Sine basis

which can not be solved in Gnumeric worsheets due to inabilty to solve complex integrals and Numerov Matrix Method (NMM) [21], which requires more computational time and effort, CDD is simple method with three easy steps and can be easily implemented in spreadsheets. Also, since the steps to obtain eigenvalues for both MM and NMM methods are more, therefore these methods have a slightly lengthier algorithm as compared to CDD method. Hence obtaining solution through CDD method requires less computational time and effort, and therefore is a good choice for implementation in UG lab projects.

2.2.1 Central Divided Difference (CDD) Method for second order derivative:

The Taylor series expansion of a function $U(x)$ about the point x_j is expressed as follows:

$$f(x) = f(x_j) + f'(x_j)(x - x_j) + \frac{1}{2!}f''(x_j)(x - x_j)^2 + \dots \quad (12)$$

If the point x lies sufficiently close to x_j, the Taylor series converges rapidly, allowing us to retain only the leading terms. By setting $x = x_j + h$, where h is a small step size, the series can be re-expressed in terms of h as:

$$f(x_j + h) = f(x_j) + f'(x_j)h + \frac{1}{2!}f''(x_j)h^2 + O(h^3) + \dots \quad (13)$$

Similarly, the Taylor Series for a point $x = x_j - h$ would be

$$f(x_j - h) = f(x_j) - f'(x_j)h + \frac{1}{2!}f''(x_j)h^2 - O(h^3) + \dots \quad (14)$$

Adding Eqns.(13) and (14), we get

$$f(x_j + h) + f(x_j - h) = 2f(x_j) + f''(x_j)h^2 + O(h^4) + \dots \quad (15)$$

So, expressing $x_j + h$ as x_{j+1} and $x_j - h$ as x_{j-1}, second derivative for the function at point x_j is obtained as

$$f''(x_j) = \frac{f(x_{j-1}) - 2f(x_j) + f(x_{j+1})}{h^2} \quad (16)$$

accurate to $O(h^2)$.
Substituting Eq.(16) in Eq.(12) and rearranging, the wave function ψ can be determined at points x_{j+1} in au as:

$$\psi(j+1) = 2\psi(j) - \psi(j-1) - 2h^2(E - V(j))\psi(j), \quad j = 2, 3, ...N. \quad (17)$$

The wavefunction $\psi(j)$ at all values of x_j (j = 3, 4, . . . , N) can be determined by choosing appropriate values for $\psi(1)$ and $\psi(2)$, for a particular value of energy E.

2.2.2 CDD Method by taking TISE as Matrix equation:

TISE can also be expressed as a tridiagonal matrix equation by writing $N - 2$ simultaneous equations that are the result of applying Eq. (16) to all $N - 2$ intermediate

points, $j = 2, 3, ..., N-1$, within the potential well. Expressing the second derivative of the wave function for intermediate points x_j, as

$$\frac{d^2}{dx^2}\psi(x_j) = \frac{\psi(x_{j-1}) - 2\psi(x_j) + \psi(x_{j+1})}{h^2} \tag{18}$$

and substituting into Time Independent Schrödinger Equation written as eigenvalue equation

$$H\psi(x) = -\frac{\hbar^2}{2m}\frac{d^2\psi(x)}{dx^2} + V(x)\psi(x) = E\psi(x) \tag{19}$$

We obtain,

$$-\frac{\hbar^2}{2mh^2}\psi(x_{j-1}) + \left(\frac{\hbar^2}{mh^2} + V(x_j)\right)\psi(x_j) - \frac{\hbar^2}{2mh^2}\psi(x_{j+1}) = E\psi(x_j). \tag{20}$$

where E denotes the eigenvalues and $\psi(x)$ represents the corresponding eigenfunctions. By letting $V(x_j) = V_j$, $\psi(x_j) = \psi_j$, and introducing

$$f_j = \frac{\hbar^2}{mh^2} + V_j = f + V_j,$$
$$g = -\frac{\hbar^2}{2mh^2} = -f/2, \tag{21}$$

the equation simplifies to:

$$g\psi_{j-1} + f_j\psi_j + g\psi_{j+1} = E\psi_j, \quad j = 2, 3, \ldots, N-1. \tag{22}$$

Also, $\psi_1 = 0$ and $\psi_N = 0$, the following equations result for $j = 2, 3, \ldots, N-1$ as:

$f_2\psi_2 + g\psi_3 + 0\psi_4 + \ldots + 0\psi_{N-3} + 0\psi_{N-2} + 0\psi_{N-1} = E\psi_2, \quad j = 2,$

$g\psi_2 + f_3\psi_3 + g\psi_4 + \ldots + 0\psi_{N-3} + 0\psi_{N-2} + 0\psi_{N-1} = E\psi_3, \quad j = 3,$

$\vdots \qquad\qquad \vdots$

$0\psi_2 + 0\psi_3 + 0\psi_4 + \ldots + g\psi_{N-3} + f_{N-2}\psi_{N-2} + g\psi_{N-1} = E\psi_{N-2}, \quad j = N-2,$

$0\psi_2 + 0\psi_3 + 0\psi_4 + \ldots + 0\psi_{N-3} + g\psi_{N-2} + f_{N-1}\psi_{N-1} = E\psi_{N-1}, \quad j = N-1.$

Rewriting these equations in matrix form :

$$\begin{bmatrix} f_2 & g & 0 & \ldots & 0 & 0 & 0 \\ g & f_3 & g & \ldots & 0 & 0 & 0 \\ \vdots & \vdots & \vdots & \ddots & \vdots & \vdots & \vdots \\ 0 & 0 & 0 & \ldots & g & f_{N-2} & g \\ 0 & 0 & 0 & \ldots & 0 & g & f_{N-1} \end{bmatrix} \begin{bmatrix} \psi_2 \\ \psi_3 \\ \vdots \\ \psi_{N-2} \\ \psi_{N-1} \end{bmatrix}$$

$$= E \begin{bmatrix} \psi_2 \\ \psi_3 \\ \vdots \\ \psi_{N-2} \\ \psi_{N-1} \end{bmatrix}$$

which may be concisely expressed as

$$H_{(N-2)\times(N-2)}\psi_{(N-2)\times 1} = E\psi_{(N-2)\times 1} \tag{23}$$

In Eq. (23), the Hamiltonian matrix is a tridiagonal symmetric matrix and is solved to obtain $(N-2)$ eigen functions and their corresponding eigen functions.

2.3 Implementation in Gnumeric worksheet :

While implementing in Gnumeric worksheet, the step by step procedure to solve Woods-Saxon potential using CDD method is required. An algorithm which will help students to understand the procedure, how to obtain single particle energy states is given below in Fig.(1). In supplementary material (**Appendix 1**), the procedure to solve the given Algorithm for proton states of doubly magic nucleus $^{56}_{28}Ni$ is given in Gnumeric worksheet, which can be easily reproduced. The energy level sequence for all doubly magic nuclei starting from $^{16}_{8}O$ to $^{310}_{126}X$ can be obtained by following the procedure given in **Appendix 1**.

3 Computational Results and Interpretation

The model parameters have been obtained earlier by our group [1] by using Variational Monte Carlo (VMC) technique in tandem with Matrix method [17] and are universally applicable to all the nuclei from lighter to heavy region. The energy level sequence for all the doubly magic nuclei have been obtained by solving TISE using CDD method and is in very good agreement with our previous results using matrix Numerov method [21] and also with experimentally available data [22]. To validate our process, the comparison of numerical results (using CDD method) with our previuos results [23] along with experimental results of doubly magic nucleus $^{40}_{20}Ca$ are given in Table (2).

3.1 Categorizing the nuclei

The gap between energy levels varies depending on the mass region under consideration. For lighter nuclei, the lower magic numbers exhibit larger energy gaps. As we move toward heavier nuclei, the energy gap between the same energy levels decreases, as demonstrated in the plot of energy differences between neutron states of various doubly magic nuclei for a specific magic number (Fig. 2). This trend occurs because, in heavier nuclei, the lower energy levels become inert and are thus suppressed, reducing the gap between filled shells.

To determine the magic and semi-magic numbers from the individual single-particle energy states of protons and neutrons, the doubly magic nuclei have been categorized into distinct mass ranges: light, medium, heavy, and super-heavy. This categorization ensures that the magic numbers are derived appropriately according to the specific mass region under investigation.

A key observation from Fig. 2 is the presence of pronounced energy gaps between consecutive single-particle states, which are crucial for identifying magic numbers. According to the nuclear shell model framework [19], such gaps, typically exceeding approximately 1 MeV; indicate shell closures that correspond to magic numbers. These significant energy separations reflect enhanced nuclear stability arising

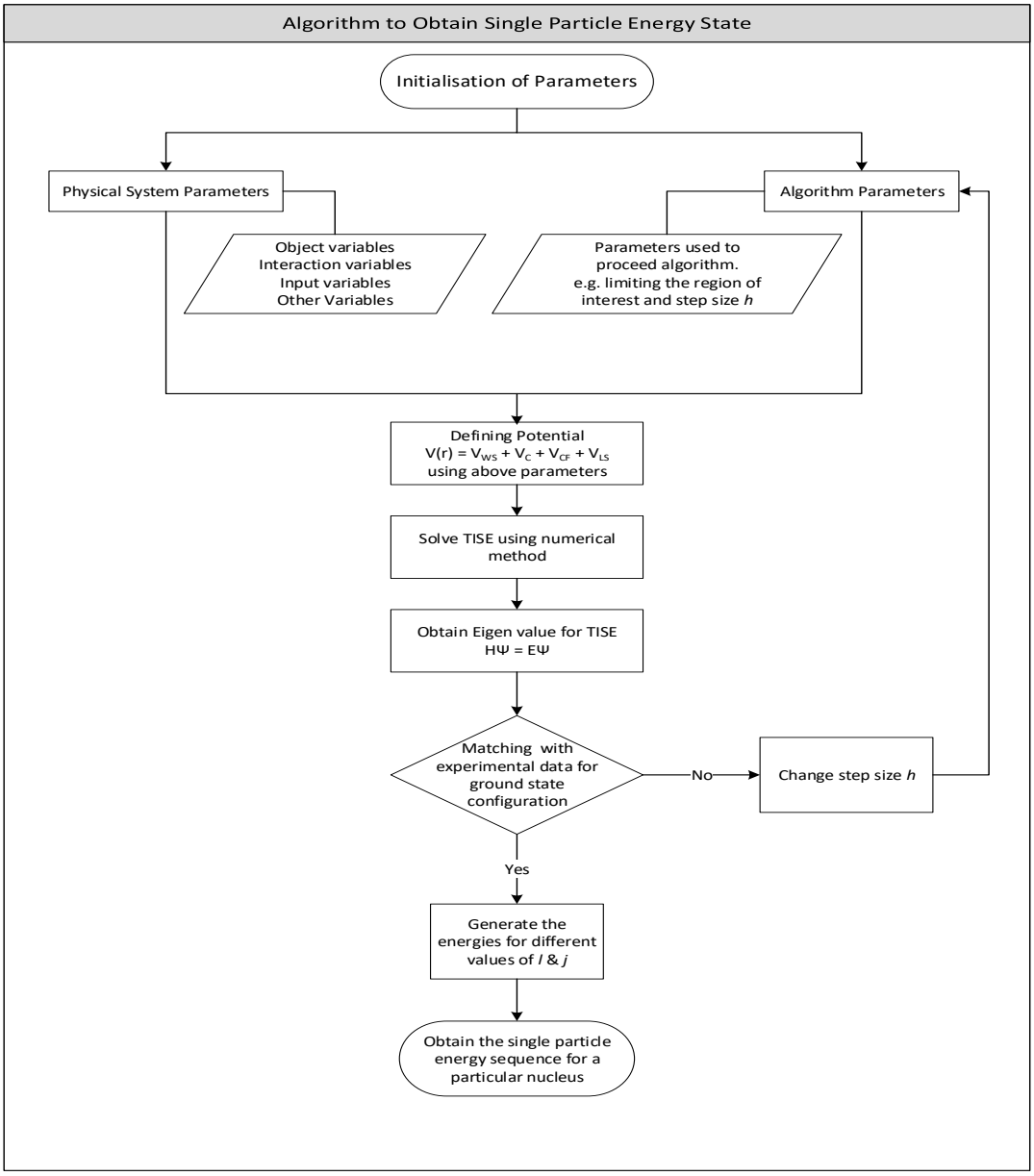

Figure 1: Algorithm to obtain single particle energy states

from filled nucleon shells, as nucleons in closed shells require a substantial amount of energy to be excited to higher states.

The energy differences between states have been calculated for both neutron and proton levels and are presented in **Appendix 2**. The plots of energy differences (in MeV) with respect to the energy level sequence for various doubly magic nuclei clearly demonstrate that at magic and semi-magic numbers, the gap between filled shells is significantly larger compared to adjacent lev-

Table 1: Comparison of single-particle energy levels (in MeV) for **protons** and **neutrons** in the doubly magic nucleus $^{40}_{20}$Ca, as obtained in the present study (*via the CDD method*), with corresponding experimental data [22] and previously reported numerical results from our group [23] (*using the Matrix Numerov method*)

States	Proton states (MeV)			States	Neutron states (MeV)		
	Exp.	Numerical values			Exp.	Numerical values	
	Ref[22]	NMM[21]	Present work		Ref[22]	NMM[21]	Present work
$1d5/2$	-15.07	-12.19	-12.19	$1d5/2$	-22.39	-19.54	-19.52
$2s1/2$	-10.92	-8.14	-8.17	$2s1/2$	-18.19	-15.54	-15.54
$1d3/2$	-8.33	-6.85	-6.85	$1d3/2$	-15.64	-14.28	-14.26
$1f7/2$	-1.09	-2.33	-2.33	$1f7/2$	-8.36	-9.15	-9.12
$2p3/2$	0.69	1.00	0.98	$2p3/2$	-5.84	-5.42	-5.42
$2p1/2$	2.38	2.94	2.93	$2p1/2$	-4.20	-3.10	-3.09
$1f5/2$	4.96	5.37	5.37	$1f5/2$	-1.56	-1.20	-1.17

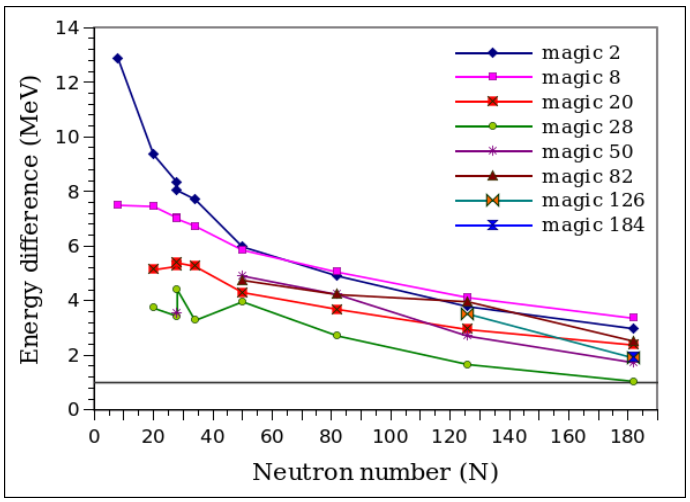

Figure 2: Energy difference vs number of neutrons for magic numbers $2, 8, 20, 28, 50, 82, 125, 184$

els. This graphical representation helps students develop a clearer understanding of the structural gaps in the energy level sequence, offering critical insights into the single-particle shell model framework.

3.2 Light nuclei : $^{16}_{8}O$ to $^{56}_{28}Ni$

Doubly magic nuclei i.e $^{16}_{8}O$, $^{40}_{20}Ca$, $^{48}_{20}Ca$ and $^{56}_{28}Ni$ in lighter mass region are very effective to study the magic numbers 2, 8, 20 and 28.

3.2.1 $^{16}_{8}O$:

If we take the case of $^{16}_{8}O$ which is at $N = Z = 8$ i.e the β-stability line, the magic numbers 2 and 8 are clearly visible for N and Z as the states $1s_{1/2}$ and $1p_{1/2}$ show the filled shells with neutron and proton equal to 2 and 8. Along with these, there is also a significant energy gap (although smaller than gap for 2 and 8) for state $1p_{3/2}$ showing 6 as the promising contender for semi-magic number.

3.2.2 $^{40}_{20}Ca$:

For $^{40}_{20}Ca$, along with magic numbers 2,8,20 for N and Z at energy states $1s_{1/2}$, $1p_{1/2}$ and $1d_{3/2}$ respectively the state $1d_{5/2}$ shows 14 as the candidate for magic number, since the energy gap is comparable to the energy gap for magic number 20. After extrapolating our data, we can also observe magic number 28 at energy level $1f_{7/2}$ for neutron states. Levels $1p_{3/2}$, $2p_{3/2}$ and $2p_{1/2}$ also shows energy gap approximately half the gap for magic numbers and predict 6 (interpolation), 32 and 34 (extrapolation) as semi-magic numbers.

3.2.3 $^{48}_{20}Ca$:

$^{48}_{20}Ca$ is another isotope of Ca having 28 neutrons and 20 protons. The magic numbers 2, 8, 20 and 28 are obtained at states $1s_{1/2}$, $1p_{1/2}$, $1d_{3/2}$ and $1f_{7/2}$ respectively for both N and Z. The state $1d_{5/2}$ shows the shell gap comparable to the state $1f_{7/2}$, again supporting 14 to be the magic number. On extrapolating the data for proton and neutron states, we get 32 as the semi-magic number with shell gap comparable to the state $1p_{3/2}$ showing 6 as the possible semi-magic number.

3.2.4 $^{56}_{28}Ni$:

$^{56}_{28}Ni$ is at the β-stability line with $N = Z = 28$. The magic numbers obtained for both neutrons N and protons Z states $1s_{1/2}$, $1p_{1/2}$, $1d_{3/2}$ and $1f_{7/2}$ are respectively 2, 8, 20 and 28. 14 is again showing its magic character at state $1f_{7/2}$. On extrapolating our data for neutron states, we get 32 as semi-magic numbers and 40 and 50 as magic number. Semi-magic behaviour of number 6 is again visible here at state $1p_{3/2}$.

3.3 Medium range nuclei : $^{100}_{50}Sn$ to $^{132}_{50}Sn$

3.3.1 $^{100}_{50}Sn$:

$^{100}_{50}Sn$ is again at β-stability line with $N = Z = 50$. On observing the energy gaps between filled shells for neutrons and protons, we get different magic and semi-magic numbers for N and Z. Magic numbers for Z = 2, 8, 18, 20, 28 and 34 are observed at states $1s_{1/2}$, $1p_{1/2}$, $1d_{3/2}$, $2s_{1/2}$, $1f_{7/2}$ and $1f_{5/2}$ respectively. For N, the magic numbers observed are 2, 8, 14, 20, 28, 50 and after extrapolation 82 magic number was also observed. Along with magic numbers, few semi-magic numbers are also observed for N = 16, 38,40, 64 and 90 and for Z = 14.

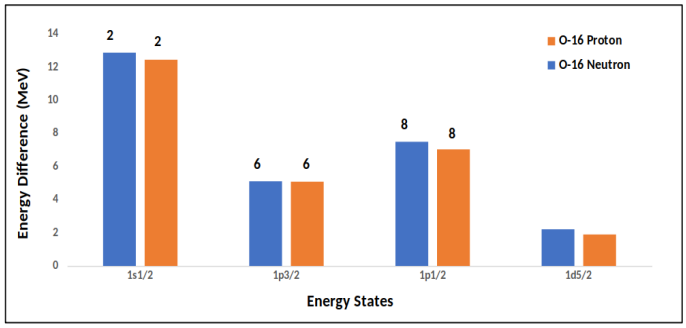

Figure 3: Separation in energy between consecutive single-particle states of $^{16}_{8}O$

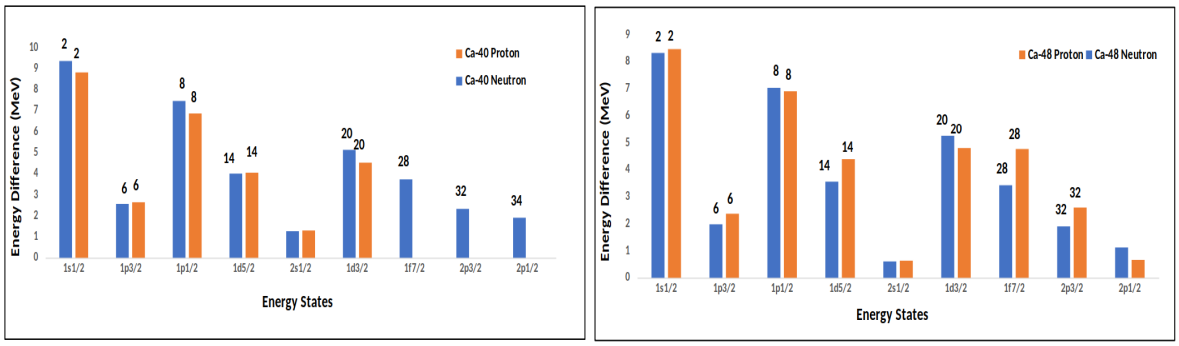

Figure 4: Separation in energy between consecutive single-particle states of (i) $^{40}_{20}Ca$ and (ii) $^{48}_{20}Ca$

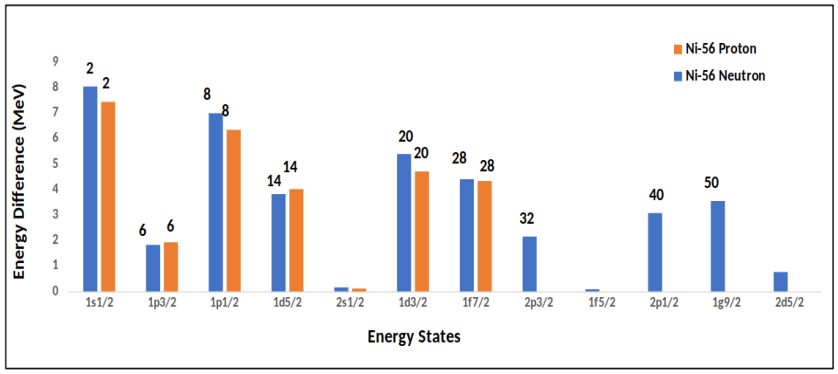

Figure 5: Separation in energy between consecutive single-particle states of $^{56}_{28}Ni$

3.3.2 $^{132}_{50}Sn$:

For $^{132}_{50}Sn$, along with already existing magic numbers 2.8. 20, 28, 50 and 82 (extrapolation), Magic number for N = 40 is observed at state $2p_{1/2}$. Semi-magic numbers for N and Z equal to 14 and 64 are observed at states $1d_{5/2}$ and $2d_{5/2}$ respectively. 18, 34 and 38 are observed semi-magic numbers for Z at states $1d_{3/2}$, 1f5/2 and 2p3/2 respec-

tively.

3.4 Heavy and Super-heavy range nuclei $^{208}_{82}Pb$ and $^{310}_{126}X$:

3.4.1 $^{208}_{82}Pb$:

The single particle neutron and proton energy states for $^{208}_{82}Pb$ show some new magic numbers. For heavy and super-heavy range, the already observed magic and semi magic numbers in the light and medium mass region are also observed for both N and Z. But here, large energy gaps are observed for magic numbers Z= 34 and 114 and N = 34, 40, 64, 100 and 126. Semi-magic numbers are observed for Z= 18, 58 and N= 18, 58, 148 and 164 (extrapolation).

3.4.2 $^{310}_{126}X$:

For $^{310}_{126}Sn$, Z= 18, 34, 58,92, 114 show large energy gaps along with already existing magic numbers. Some new magic numbers are observed at filled shells $1h_{9/2}$, $1j_{15/2}$ and $3d_{3/2}$ and $1k_{17/2}$ for N= 92, 164, 184 and 228 along with 34, 58 and 126. Semi-magic numbers are observed for Z= 76 and N=100, 136 and 172.

4 Conclusions

In this paper, an effort have been made to provide a simple procedure for students at graduate level, to understand the concept of magic and semi-magic number by analysing the energy gap between consecutive states of doubly magic nuclei ($^{16}_{8}O$ to $^{310}_{126}X$). A step wise procedure to calculate single particle energy states have also been given. Studying energy levels of doubly magic nuclei in various mass regions within the Shell model, enables to explain some of the observed sub-shell closures leading to stability in neutron rich nuclei. By calculating the energy difference or energy gap between consecutive energy states, we can deduce magic and semi-magic numbers by considering that the energy difference between two consecutive states must be greater than 1 MeV. It is observed that few numbers can be considered as the magic numbers e.g. N = 14, 34, 40, 164, 184 and 228, Z = 14, 34, 92 and 114 along with already defined magic numbers and some new semi-magic numbers can also be deduced e.g. N = 6, 16, 18, 32, 40, 58, 64, 92, 100, 136, 164 and 172, Z= 18, 58 and 76 by analysing the energy gaps between filled shells of the doubly magic nuclei. The results presented here depends only on the study done for doubly magic nuclei. The study can be further enhanced by taking more nuclei in different mass region.

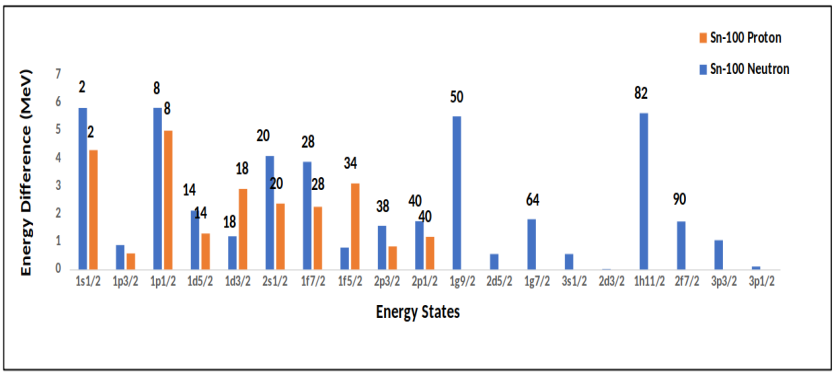

Figure 6: Separation in energy between consecutive single-particle states of $^{100}_{50}Sn$

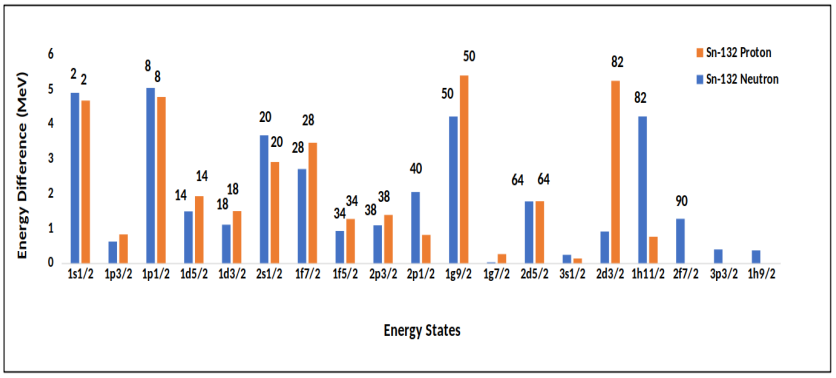

Figure 7: Separation in energy between consecutive single-particle states of $^{132}_{50}Sn$

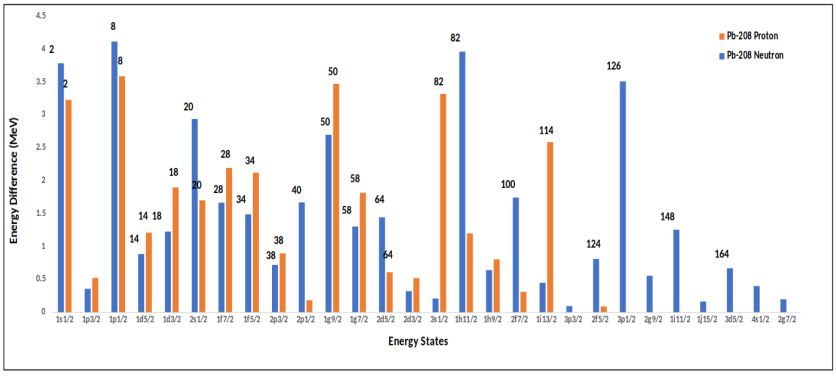

Figure 8: Separation in energy between consecutive single-particle states of $^{208}_{82}Pb$

5 Appendix 1

The various steps involved to implement Central divided difference method (CDD) in Gnumeric spreadsheets, to obtain single particle energy states of $^{56}_{28}Ni$ nucleusare given below. The Woods-Saxon potential have been taken as the as the interaction po-

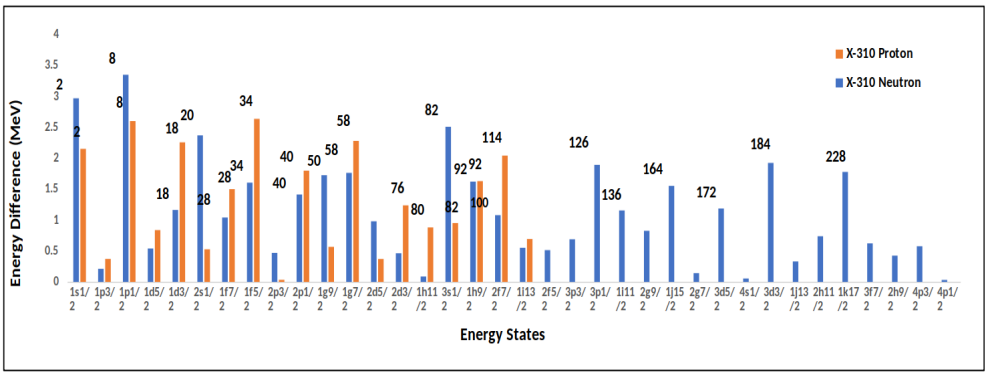

Figure 9: Separation in energy between consecutive single-particle states of $^{310}_{126}X$

tential along with spin-orbit coupling.

1. **Initialisation of parameters:** In order to initialise, we will first describe two set of parameters:
   (a) *Physical system parameters*:
   Object and interaction variables will be the inputs and state variables are the outputs, which we want to determine.
   Figure (1) shows object variables, interaction variables, algorithm variables, input variables and other variables required for the calculations.
   (b) *Algorithm parameters* The discretization of continuous variables and the reduction of infinitely large amounts to finite values, such as region of interest, provide algorithmic parameters. The step size is chosen as $h = 0.1$ and is given in cell F16, shown in Figure (10).

2. **Potential Definition:**
   The values of 'r' are generated from 0.1 to $(3 * R)$ with step-size $h = 0.1$ from A21 to A167, and to get the expected results, corresponding matrix size is 144×144. Then, four potentials are determined using the following formulae for a particular ℓ and j values. The sample sheet has been given in Figure (11)
   (a) Centrifugal potential V_{CF}, in cell B21 type the formula:

```
=($I$7*($I$7+1)*$I$13^2*
 ($A21^(-2)))/(2*$I$12)
```

(b) Woods-Saxon potential V_{WS}, in cell D21 by typing the formula:

```
=$F$8*(1+$C21)^(-1)
```

(c) L.S potential V_{LS}, in cell F21 by typing formula:

```
=-$F$13*$F$12^2*$I$15*$C21*
 $E21*($F$9*$A21)^(-1)
```

where, the L.S term in cell I15 is calculated by formula:

```
=$I$8*($I$8+1)-$I$7*($I$7+1)-3/4
```

(d) Coulomb potential, for proton, is given by typing formula:

	A	B	C	D	E	F	G	H	I	J
1	**Solving Woods-Saxon potential with Spin-orbit coupling (using CDD method)**									
2	***(Ni^{56} proton)***									
3										
4	**Initialzing the Parameters**									
5	***Object variables***				***Interaction variables***			***Input variables***		
6								*To be varied for various energy states*		
7	**Mass of neutron (m_n)**	939.565	MeV/c^2		***Woods-Saxon potential***			**Orbital angular momentum qtm.no. *(l)***	2.00	
8	**Mass of proton (m_p)**	938.272	MeV/c^2		**Potential well depth (V_0)**	−51.00	MeV	**Total angular momentum qtm no. *(j)***	1.50	
9	**Radius prop. Constant (R_0)**	1.28	fm		**Surface diffuseness (a)**	0.66				
10	**Mass of nucleus (A)**	56			**Range (R)**	4.897	fm	***Other variables***		
11	**Charge of nucleus (Z)**	28			***Spin-orbit potential***					
12	**Number of neutrons (N)**	28			**Dimensionality of distance (r_0)**	0.90	fm	**Reduced mass (μ)**	914.831	MeV/c^2
13	**Z-1 (Z_p)**	27			**Dimensionality of energy (V_1)**	22.44	MeV	**$\hbar$*c**	197.329	MeV-fm
14	**Radius of nucleus (R)**	4.897104	fm					**function *f* ($=-\hbar^2*c^2/2\mu c^2$)**	−21.282	$MeV\text{-}fm^2$
15					***Algorithm parameter***			**LS term**	−3.00	
16					**Step size (*h*)**	0.10	fm	**Cut off distance (a_0=3*R)**	14.691	fm

Figure 10: Initializing the parameters for the system

	A	B	C	D	E	F	G	H
18	**Total interaction potential**							
19								
20	**r**	**V_{cf}**	**f_1**	**V_{WS}**	**f_2**	**V_{LS}**	**V_C**	**$V=V_{cf}+V_{WS}+V_{LS}+V_C$**
21	0.1	12769.1517	0.0006973	−50.964464	0.9986	0.5753	11.9961430	12730.7586429
22	0.2	3192.2879	0.0008113	−50.958655	0.9984	0.3346	11.9911401	3153.6550267
23	0.3	1418.7946	0.0009441	−50.951898	0.9981	0.2595	11.9828019	1380.0850426
24	0.4	798.0720	0.0010985	−50.944037	0.9978	0.2264	11.9711284	759.3254726
25	0.5	510.7661	0.0012782	−50.934893	0.9974	0.2107	11.9561197	471.9979694
26	0.6	354.6987	0.0014873	−50.924258	0.9970	0.2042	11.9377756	315.9163748
27	0.7	260.5949	0.0017307	−50.911888	0.9965	0.2036	11.9160963	221.8027032
28	0.8	199.5180	0.0020138	−50.897503	0.9960	0.2071	11.8910817	160.7187139
29	0.9	157.6438	0.0023432	−50.880774	0.9953	0.2141	11.8627319	118.8399115
30	1.0	127.6915	0.0027266	−50.861322	0.9946	0.2240	11.8310467	88.8852892

Figure 11: Defining potentials:

```
=$B$13*0.511*2.839*
 (3*$B$14^2-$A21^2)/(2*$B$14^3)
```

in cell G21 up-to radius 'R' of the nucleus. After that in cell G64, type the formula:

```
=0.511*2.839*$A64^(-1)*$B$13
```

which gives the Coulomb potential outside the range of nuclear radius.
(*e*) In cell H21, the net potential is determined by typing the formula as:

```
=$B21+$D21+$F21+$G21
```

3. **Obtaining Hamiltonian matrix:**
To obtain Hamiltonian matrix, we will first define two functions f_j and g: (*a*) The functions

$$f_j = \frac{\hbar^2}{mh^2} + V_j = f + V_j,$$
$$g = -\frac{\hbar^2}{2mh^2} = -f/2, \qquad (24)$$

are defined as

```
=$H21+(($I$13^2)/($I$12*$F$16^2))
```

and

```
=-(($I$13^2)/(2*$I$12*$F$16^2))
```

	A	B	C	D	E	F
1	**Hamiltonian Matrix**					
2						
3		**1**	**2**	**3**	**4**	**5**
4	**1**	16987.1425	−2128.1919	0.0000	0.0000	0.0000
5	**2**	−2128.1919	7410.0389	−2128.1919	0.0000	0.0000
6	**3**	0.0000	−2128.1919	5636.4689	−2128.1919	0.0000
7	**4**	0.0000	0.0000	−2128.1919	5015.7094	−2128.1919
8	**5**	0.0000	0.0000	0.0000	−2128.1919	4728.3819

Figure 12: Initializing the parameters for the system

in cell I21 and J21 respectively.
(*b*) Now in Sheet 2; named '*Matrix*', generate index values for rows and columns as 1 to 144 from A4:A147 and B3:EO3.
(*c*) In cell B4, type:

```
=if($A4=B$3,Initialization!$J21,
 if($A4=B$3-1,Initialization!$K21,
 if($A4=B$3+1,Initialization!$K21,0)))
```

(*d*) After that drag the formula along the row till EO3 and then downwards up-to EO147 to obtain the tridiagonal Hamiltonian matrix as shown in Figure (12).

4. **Obtaining Eigen values and Eigen vectors:**
(*a*) In Sheet 3, named '*Eigenvalues*', generate index values for rows and columns as 1 to 145 from A4:A148 and 1 to 144 from B3:EO3 to obtain matrix of size 145 × 144. The extra row has been incorporated for eigen values. Below each of the eigen values in the first row, a corresponding eigen vector of size 131 1 will be obtained.
(*b*) In cell B4, type formula

```
=eigen('Matrix'!B4:EO147)
```

After that, press three keys Ctrl+Shift+Enter altogether to obtain the required Eigen values. The result for $d_{3/2}$ state has been shown in Figure (13). The eigen value obtained is $= -10.461$.

5. **Eigen values for different states:**
The bound state energies (i.e. the energies for which eigen values are negative), are obtained for different values of ℓ and j as:
(a) For s-state, $\ell = 0$ and $j = 0.5$ corresponds to $1s_{1/2}$ state.
(b) For p-state, $\ell = 1$ and $j = 0.5, 1.5$ corresponds to states $1p_{1/2}$ and $1p_{3/2}$.
The same procedure is repeated for d, f, g, h, i etc. states to obtain all energy states till any bound state is available.

	A	B	C	D	E	F	EL	EM	EN	EO
1		**Eigen Values (MeV) and eigen vectors**								
2										
3		**1**	**2**	**3**	**4**	**5**	**141**	**142**	**143**	**144**
4	**1**	**17456.457**	**9202.933**	**8530.565**	**8516.251**	**8509.845**	**17.953**	**10.616**	**−10.461**	**6.931**
5	**2**	0.976	−0.143	0.037	0.000	0.001	0.000	0.000	0.000	0.000
6	**3**	−0.215	−0.522	0.149	0.001	0.003	0.000	0.000	0.000	0.000
7	**4**	0.040	0.583	−0.116	−0.001	−0.002	−0.001	−0.001	0.000	0.000
8	**5**	−0.007	−0.454	0.009	0.000	0.000	−0.002	−0.001	0.001	−0.001

Figure 13: Initializing the parameters for the system

6 Appendix 2

In this section, the energy difference corresponding to neutron and proton states of doubly magic nuclei from ${}^{16}_{8}O$ to ${}^{310}_{126}X$ are given in tabular form.

- ${}^{16}_{8}O, {}^{40}_{20}Ca$:
- ${}^{48}_{20}Ca, {}^{56}_{28}Ni$:
- ${}^{100}_{50}Sn, {}^{132}_{50}Sn$:
- ${}^{208}_{82}Pb$ and ${}^{310}_{126}X$:

Table 2: Single particle energies *(in MeV)* and Energy difference (E_D) in *MeV* for neutron and proton states of doubly magic $^{16}_{8}O$ and $^{40}_{20}Ca$

$^{16}_{8}O$						$^{40}_{20}Ca$					
Neutron states			Proton states			Neutron states			Proton states		
States	Energy (*MeV*)	E_D	States	Energy (*MeV*)	E_D	States	Energy	E_D	States	Energy (*MeV*)	E_D (*MeV*)
...	...	...	...	...	...	$1f5/2$	-1.20	...	...	...	
...	...	...	...	...	...	$2p1/2$	-3.10	1.90	...	...	
...	...	...	...	...	...	$2p3/2$	-5.42	2.32	...	...	
...	...	...	...	...	...	$1f7/2$	-9.15	3.73	$1f7/2$	-2.33	...
...	...	...	...	...	...	$1d3/2$	-14.28	5.13	$1d3/2$	-6.85	4.52
$2s1/2$	-3.03	...	$2s1/2$	-0.21	...	$2s1/2$	-15.54	1.26	$2s1/2$	-8.17	1.30
$1d5/2$	-5.25	2.22	$1d5/2$	-2.11	1.90	$1d5/2$	-19.54	4.00	$1d5/2$	-12.19	4.04
$1p1/2$	-12.74	7.49	$1p1/2$	-9.14	7.04	$1p1/2$	-26.99	7.45	$1p1/2$	-19.04	6.86
$1p3/2$	-17.85	5.11	$1p3/2$	-14.23	5.09	$1p3/2$	-29.55	2.56	$1p3/2$	-21.68	2.64
$1s1/2$	-30.73	12.88	$1s1/2$	-26.68	12.45	$1s1/2$	-38.90	9.35	$1s1/2$	-30.49	8.81

Table 3: Single particle energies *(in MeV)* and Energy difference (E_D) in *MeV* for neutron and proton states of doubly magic $^{48}_{20}Ca$ and $^{56}_{28}Ni$

$^{48}_{20}Ca$						$^{56}_{28}Ni$					
Neutron states			Proton states			Neutron states			Proton states		
States	Energy (*MeV*)	E_D	States	Energy (*MeV*)	E_D	States	Energy	E_D	States	Energy (*MeV*)	E_D (*MeV*)
...	...	...	...	...	...	$3s1/2$	-0.94	...	...	...	...
...	...	...	...	...	...	$2d5/2$	-1.70	0.76	...	...	...
...	...	...	...	...	...	$1g9/2$	-5.25	3.55	...	...	...
$1f5/2$	-1.87	...	$1f5/2$	-1.71	...	$2p1/2$	-8.32	3.07	...	...	...
$2p1/2$	-3.00	1.12	$2p1/2$	-2.38	0.66	$1f5/2$	-8.41	0.09	...	...	...
$2p3/2$	-4.90	1.90	$2p3/2$	-4.98	2.60	$2p3/2$	-10.56	2.15	$2p3/2$	-1.56	...
$1f7/2$	-8.33	3.43	$1f7/2$	-9.75	4.77	$1f7/2$	-14.96	4.40	$1f7/2$	-5.89	4.33
$1d3/2$	-13.58	5.26	$1d3/2$	-14.55	4.80	$1d3/2$	-20.35	5.39	$1d3/2$	-10.60	4.70
$2s1/2$	-14.19	0.61	$2s1/2$	-15.18	0.63	$2s1/2$	-20.51	0.16	$2s1/2$	-10.71	0.11
$1d5/2$	-17.75	3.56	$1d5/2$	-19.57	4.39	$1d5/2$	-24.33	3.82	$1d5/2$	-14.72	4.01
$1p1/2$	-24.78	7.03	$1p1/2$	-26.48	6.90	$1p1/2$	-31.32	6.99	$1p1/2$	-21.06	6.34
$1p3/2$	-26.76	1.98	$1p3/2$	-28.85	2.37	$1p3/2$	-33.14	1.83	$1p3/2$	-22.99	1.93
$1s1/2$	-35.08	8.32	$1s1/2$	-37.31	8.46	$1s1/2$	-41.18	8.04	$1s1/2$	-30.42	7.43

Table 4: Single particle energies *(in MeV)* and Energy difference (E_D) in MeV for neutron and proton states of doubly magic $^{100}_{50}Sn$, $^{132}_{50}Sn$

$^{100}_{50}Sn$						$^{132}_{50}Sn$					
Neutron states			Proton states			Neutron states			Proton states		
States	Energy (MeV)	E_D	States	Energy (MeV)	E_D	States	Energy	E_D	States	Energy (MeV)	E_D (MeV)
$1h9/2$	-0.21	...	...	...	...	$3p1/2$	-0.57	...	...	...	...
$3p1/2$	-0.31	0.10	...	...	...	$1h9/2$	-0.94	0.37	...	...	...
$3p3/2$	-1.36	1.05	...	...	...	$3p3/2$	-1.34	0.40	...	...	...
$2f7/2$	-3.08	1.72	...	...	...	$2f7/2$	-2.61	1.28	$2f7/2$	-1.18	...
$1h11/2$	-8.70	5.62	...	...	...	$1h11/2$	-6.83	4.22	$2d3/2$	-6.43	5.25
$2d3/2$	-8.72	0.02	...	...	...	$2d3/2$	-7.74	0.91	$3s1/2$	-6.56	0.13
$3s1/2$	-9.27	0.55	...	...	...	$3s1/2$	-7.99	0.24	$1h11/2$	-7.32	0.76
$1g7/2$	-11.08	1.81	...	...	...	$2d5/2$	-9.76	1.78	$2d5/2$	-9.10	1.78
$2d5/2$	-11.63	0.55	...	...	...	$1g7/2$	-9.79	0.02	$1g7/2$	-9.37	0.26
$1g9/2$	-17.13	5.50	$1g9/2$	-3.06	...	$1g9/2$	-14.01	4.22	$1g9/2$	-14.77	5.40
$2p1/2$	-18.87	1.74	$2p1/2$	-4.23	1.17	$2p1/2$	-16.06	2.05	$2p1/2$	-15.58	0.81
$2p3/2$	-20.44	1.57	$2p3/2$	-5.05	0.83	$2p3/2$	-17.15	1.09	$2p3/2$	-16.97	1.39
$1f5/2$	-21.22	0.79	$1f5/2$	-8.14	3.09	$1f5/2$	-18.07	0.93	$1f5/2$	-18.24	1.27
$1f7/2$	-25.09	3.87	$1f7/2$	-10.39	2.25	$1f7/2$	-20.78	2.71	$1f7/2$	-21.70	3.47
$2s1/2$	-29.17	4.08	$2s1/2$	-12.76	2.37	$2s1/2$	-24.46	3.68	$2s1/2$	-24.61	2.91
$1d3/2$	-30.36	1.19	$1d3/2$	-15.66	2.89	$1d3/2$	-25.57	1.11	$1d3/2$	-26.11	1.50
$1d5/2$	-32.48	2.11	$1d5/2$	-16.95	1.29	$1d5/2$	-27.06	1.49	$1d5/2$	-28.04	1.93
$1p1/2$	-38.29	5.81	$1p1/2$	-21.94	4.99	$1p1/2$	-32.10	5.04	$1p1/2$	-32.83	4.78
$1p3/2$	-39.16	0.88	$1p3/2$	-22.52	0.58	$1p3/2$	-32.72	0.62	$1p3/2$	-33.65	0.83
$1s1/2$	-44.97	5.81	$1s1/2$	-26.81	4.29	$1s1/2$	-37.63	4.90	$1s1/2$	-38.33	4.68

Table 5: Single particle energies *(in MeV)* and Energy difference (E_D) in MeV for neutron and proton states of doubly magic $^{208}_{82}Pb$ and $^{310}_{126}X$

$^{208}_{82}Pb$						$^{310}_{126}X$					
Neutron states			Proton states			Neutron states			Proton states		
States	Energy (MeV)	E_D	States	Energy (MeV)	E_D	States	Energy	E_D	States	Energy (MeV)	E_D (MeV)
...	...	...	...	...	...	$3f5/2$	-1.40	...	...	...	...
...	...	...	...	...	...	$4p1/2$	-1.43	0.03	...	...	...
...	...	...	...	...	...	$4p3/2$	-2.00	0.58	...	...	...
...	...	...	...	...	...	$2h9/2$	-2.43	0.42	...	...	...
...	...	...	...	...	...	$3f7/2$	-3.05	0.62	...	...	...
...	...	...	...	...	...	$1k17/2$	-4.83	1.78	...	...	...
...	...	...	...	...	...	$2h11/2$	-5.57	0.74	...	...	...
...	...	...	...	...	...	$1j13/2$	-5.90	0.33	...	...	...
$3d3/2$	-0.82	...	...	...	...	$3d3/2$	-7.83	1.93	...	...	...
$2g7/2$	-1.01	0.20	...	...	...	$4s1/2$	-7.88	0.05	...	...	...
$4s1/2$	-1.41	0.40	...	...	...	$3d5/2$	-9.07	1.19	...	...	...
$3d5/2$	-2.07	0.67	...	...	...	$2g7/2$	-9.21	0.14	...	...	...
$1j15/2$	-2.24	0.16	...	...	...	$1j15/2$	-10.76	1.55	...	...	...
$1i11/2$	-3.49	1.25	...	...	...	$2g9/2$	-11.59	0.83	...	...	...
$2g9/2$	-4.04	0.55	...	...	...	$1i11/2$	-12.75	1.16	...	...	...
$3p1/2$	-7.55	3.51	...	...	...	$3p1/2$	-14.64	1.89	...	...	...
$2f5/2$	-8.36	0.81	$3p3/2$	-0.28	...	$3p3/2$	-15.33	0.69	...	...	...
$3p3/2$	-8.45	0.09	$2f5/2$	-0.37	0.09	$2f5/2$	-15.85	0.51	$2f5/2$	-0.31	...
$1i13/2$	-8.90	0.45	$1i13/2$	-2.95	2.58	$1i13/2$	-16.40	0.55	$2f7/2$	-2.36	2.04
$2f7/2$	-10.64	1.74	$2f7/2$	-3.26	0.31	$2f7/2$	-17.48	1.08	$1i13/2$	-3.05	0.69
$1h9/2$	-11.28	0.64	$1h9/2$	-4.26	1.00	$1h9/2$	-19.10	1.62	$1h9/2$	-4.68	1.63
$1h11/2$	-15.24	3.96	$3s1/2$	-7.57	3.32	$3s1/2$	-21.61	2.51	$3s1/2$	-5.63	0.95
$3s1/2$	-15.44	0.21	$2d3/2$	-8.09	0.52	$1h11$	-21.70	0.09	$ih11/2$	-6.52	0.88
$2d3/2$	-15.76	0.32	$1h11/2$	-9.29	1.20	$2d3/2$	-22.16	0.46	$2d3/2$	-7.75	1.24
$2d5/2$	-17.20	1.44	$2d5/2$	-9.89	0.61	$2d5/2$	-23.14	0.98	$2d5/2$	-8.13	0.37
$1g7/2$	-18.50	1.30	$1g7/2$	-11.71	1.81	$1g7/2$	-24.91	1.76	$1g7/2$	-10.41	2.28
$1g9/2$	-21.20	2.70	$1g9/2$	-15.18	3.47	$1g9/2$	-26.63	1.73	$2p1/2$	-12.21	1.80
$2p1/2$	-22.87	1.67	$2p1/2$	-15.36	0.18	$2p1/2$	-28.05	1.41	$1g9/2$	-12.77	0.57
$2p3/2$	-23.59	0.72	$2p3/2$	-16.25	0.89	$2p3/2$	-28.52	0.47	$2p3/2$	-12.81	0.03
$1f5/2$	-25.07	1.49	$1f5/2$	-18.37	2.12	$1f5/2$	-30.12	1.61	$1f5/2$	-15.45	2.64
$1f7/2$	-26.74	1.66	$1f7/2$	-20.56	2.19	$1f7/2$	-31.16	1.04	$1f7/2$	-16.95	1.50
$2s1/2$	-29.67	2.94	$2s1/2$	-22.26	1.70	$2s1/2$	-33.54	2.37	$2s1/2$	-17.47	0.53
$1d3/2$	-30.90	1.22	$1d3/2$	-24.16	1.89	$1d3/2$	-34.70	1.16	$1d3/2$	-19.73	2.26
$1d5/2$	-31.78	0.88	$1d5/2$	-25.37	1.21	$1d5/2$	-35.24	0.54	$1d5/2$	-20.57	0.84
$1p1/2$	-35.89	4.11	$1p1/2$	-28.95	3.59	$1p1/2$	-38.59	3.35	$1p1/2$	-23.17	2.60
$1p3/2$	-36.25	0.36	$1p3/2$	-29.47	0.52	$1p3/2$	-38.80	0.21	$1p3/2$	-23.55	0.37
$1s1/2$	-40.03	3.78	$1s1/2$	-32.70	3.23	$1s1/2$	-41.78	2.97	$1s1/2$	-25.70	2.15

References

[1] Aditi Sharma, Swapna Gora, Jithin Bhagavathi, and O. S. K. S Sastri, "Simulation study of nuclear shell model using sine basis", Am. J. Phys. 88, 576 (2020).

[2] Jouni Suhonen. From nucleons to nucleus: concepts of microscopic nuclear theory. Springer Science & Business Media, 2007.

[3] Eugene Meyer, "Shell model of nuclear structure," Am. J. Phys. 36, 250–257 (1968).

[4] Steppenbeck, D., Takeuchi, S., Aoi, N., Doornenbal, P., Matsushita, M., Wang, H., ... & Yoneda, K. (2013). Evidence for a new nuclear 'magic number'from the level structure of 54Ca. Nature, 502(7470), 207-210.

[5] Warner, D. (2004). Not-so-magic numbers. Nature, 430(6999), 517-519.

[6] Ali A. Alzubadi, and Redhab A. Allawi. "Investigation of the magicity in some even–even Ca isotopes by using shell model and Hartree–Fock–Bogoliubov method." Indian Journal of Physics 96, 4, 1205-1216 (2022).

[7] Nakada, H., & Sugiura, K. (2014). Predicting magic numbers of nuclei with semi-realistic nucleon–nucleon interactions. Progress of Theoretical and Experimental Physics, 2014(3).

[8] Fridmann, J., I. Wiedenhöver, A. Gade, L. T. Baby, D. Bazin, B. A. Brown, C. M. Campbell et al. "Magic'nucleus 42Si." Nature 435, no. 7044 (2005): 922-924.

[9] Steppenbeck, David, Satoshi Takeuchi, Nori Aoi, P. Doornenbal, Masafumi Matsushita, H. Wang, Hidetada Baba et al. "Evidence for a new nuclear 'magic number'from the level structure of 54Ca." Nature 502, no. 7470 (2013): 207-210.

[10] Janssens, Robert VF. "Unexpected doubly magic nucleus." Nature 459, no. 7250 (2009): 1069-1070.

[11] Alzubadi, Ali A., and Redhab A. Allawi. "Investigation of the magicity in some even–even Ca isotopes by using shell model and Hartree–Fock–Bogoliubov method." Indian Journal of Physics 96, no. 4 (2022): 1205-1216.

[12] `https://www.ugc.ac.in/pdfnews/7870779_B.SC.PROGRAM-PHYSICS.pdf`.

[13] Krane, S.Kenneth, *Introductory Nuclear Physics*(Jon Wiley & Sons, New York, 1988).

[14] Samuel S.M. Wong, *Introductory nuclear physics*(New Jersey: Prentice Hall, 1990).

[15] R. D. Woods and D. S. Saxon, "Diffuse Surface Optical Model for Nucleon-Nuclei Scattering". Physical Review. 95 (2): 577–578(1954).

[16] David Hestenes. "Toward a modeling theory of physics instruction." American journal of physics 55, 5, 440-454 (1987).

[17] Jugdutt, B. A., & Marsiglio, F. (2013). Solving for three-dimensional central potentials using numerical matrix methods. American Journal of Physics, 81(5), 343-350.

[18] O. S. K. S. Sastri, Aditi Sharma, Swapna Gora, and Richa Sharma. "Comparative Analysis of Woods-Saxon and Yukawa Model Nuclear Potentials." Journal of Nuclear Physics, Material Sciences, Radiation and Applications 9, 1, 73-79 (2021).

[19] Aage Bohr and Ben R. Mottelson, Nuclear Structure (World Scientific,Singapore, 1998).

[20] Aditi Sharma and O. S. K. S. Sastri, "Numerical simulation of quantum anharmonic oscillator, embedded within an infinite square well potential, by matrix methods using gnumeric spreadsheet", European Journal of Physics (2020):1-20.

[21] Mohandas Pillai, Joshua Goglio, and Thad G. Walker, "Matrix Numerov Method for Solving Schrödinger's Equation", American Journal of Physics. 80, 1017 (2012).

[22] N. Schwierz, I. Wiedenhover, and A. Volya, "Parameterization of the Woods-Saxon potential for shell-model calculations," preprint arXiv:0709.3525 (2007).

[23] Awasthi, Shikha, Aditi Sharma, Swapna Gora, and O. S. K. S. Sastri. "Numerical Simulation of Shell Model Single Particle Energy States using Matrix Numerov Method in Gnumeric Worksheet." arXiv preprint arXiv:2205.10335 (2022).

Gravity in Undergraduate Thermal Physics Courses

Kartik Tiwari[1]
[1]Department of Physics, Ashoka University, Delhi-NCR 131029, India.
krtk.twri@gmail.com

Submitted on July 18, 2021

Abstract

A pedagogical aid is proposed for undergraduate thermal physics courses to introduce students to how the inclusion of gravity challenges the conventional formulations of the laws of thermodynamics. The aim is to stimulate deeper interest in thermal physics by revealing its conceptual overlap with general relativity—an intersection often overlooked in standard curricula.

1 Introduction

From cosmology to information theory, thermal physics has quietly shaped some of the most profound developments in modern science. Yet one of its most surprising intersections—that between thermodynamics and gravity—remains largely inaccessible to undergraduate students, obscured by the technical prerequisites of general relativity.

This paper proposes a pedagogical aid that can be incorporated into standard undergraduate thermal physics courses shortly after the introduction of the second law. Building on a reformulation by Santiago and Visser [2], which casts the Tolman–Ehrenfest effect in the language of special relativity, this framework opens a window into deep conceptual terrain without requiring a formal background in general relativity.

I present three interconnected arguments that invite students to rethink thermal equilibrium in the presence of gravity. The first is a classical argument, attributed to Maxwell, which shows that temperature gradients at equilibrium lead to a violation of the second law. The second argument, from Santiago and Visser, demonstrates that such gradients must in fact exist in gravitational fields—a result consistent with relativistic effects, not classical intuitions. The third considers whether electric fields might also induce equilibrium temperature gradients, ultimately revealing that while electromagnetism is not universal, its effects can influence equilibrium indirectly—through gravity itself.

2 Maxwell's Argument

Maxwell argued, on purely physical grounds, that temperature gradients cannot exist within bodies at thermal equilibrium [1].

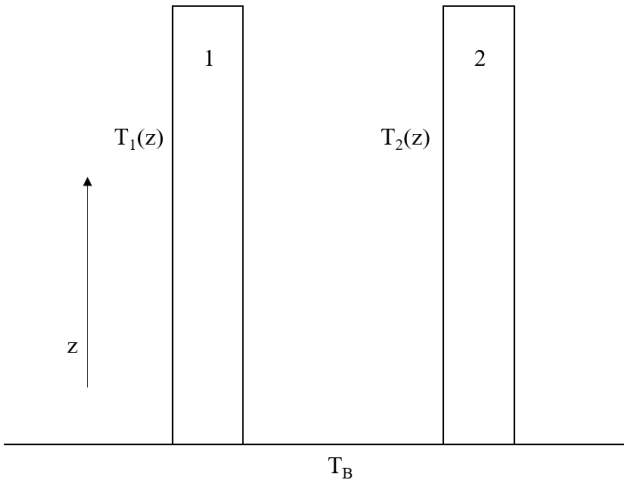

Figure 1: The hypothetical two column setting for Maxwell's argument

Imagine two vertical columns placed atop a thermally conducting surface. The base of each column is in thermal contact with this surface, ensuring equilibrium at $z = 0$ (see Fig. 1). Now suppose, hypothetically, that despite the system being in thermal equilibrium, both columns exhibit temperature gradients along the z-axis.

If, at any height z, we find that $T_1(z) > T_2(z)$ (or vice versa—the labeling is arbitrary), we could insert a horizontal conducting rod between the two columns at that level. Heat would then flow from the hotter to the cooler column. Part of this heat would descend through column 2 to its base, and from there conduct laterally through the shared surface, eventually heating the base of column 1. That in turn drives heat upward through column 1—completing a cycle (see Fig. 2).

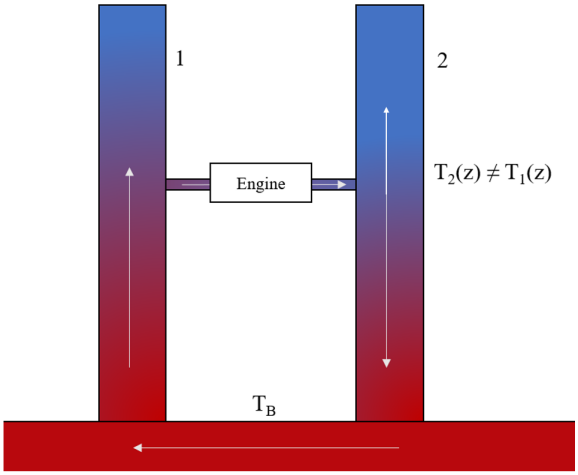

Figure 2: Inequality in temperature gradient creating a perpetual motion engine

We may now place a heat engine on the conducting rod at height z. The columns, under our assumption, act perpetually as thermal reservoirs at different temperatures—even while the system is nominally in equilibrium. This would allow us to extract work indefinitely, constructing a perpetual motion machine of the second kind—an absurdity that directly violates the second law of thermodynamics. Therefore, our initial assumption that $T_1(z) \neq T_2(z)$ must be false.

Maxwell reinforces this theoretical argument with an empirical observation: since we do not observe temperature gradients in columns of ideal gas at equilibrium, no substance ought to exhibit such gradi-

ents. If such a gradient existed, one could exploit the difference to violate Clausius's formulation of the second law (and, because Clausius' and Kelvin's formulations are logically equivalent, students are encouraged to reflect on how the same hypothetical apparatus would violate Kelvin's version as well).

3 (Modified) Santiago-Visser's Argument

I now present a modified version of a proof—originally due to Santiago and Visser [2]—demonstrating the existence of temperature gradients in a photon gas column. In their foundational work[4], Tolman and Ehrenfest showed that temperature at thermal equilibrium need not remain constant in curved spacetime, but instead varies with gravitational potential. Their derivation, however, relied on the machinery of general relativistic hydrodynamics—well beyond the scope of most undergraduate thermal physics curricula.

Santiago and Visser offered a more accessible approach, using only the concept of gravitational redshift to reach the same conclusion. Since redshift can be derived within the framework of special relativity, students already familiar with undergraduate electromagnetism should be able to grasp the argument with minimal additional background.

In adapting their proof, I depart slightly from the original treatment: instead of assuming a uniform gravitational field, I consider a spherically symmetric one. This choice streamlines the transition to the third argument in this paper, which addresses electromagnetic contributions to equilibrium gradients.

Let us now outline the setup. Consider a photon gas column situated within a spherically symmetric gravitational field, offset slightly from the radial direction (see Fig. 3). Suppose an observer located far from the column measures the spectral radiance of each segment and finds that the peak wavelength remains constant over time and position. By Wien's displacement law, the observer concludes that the system is in thermal equilibrium: the temperature of the column appears spatially and temporally uniform.

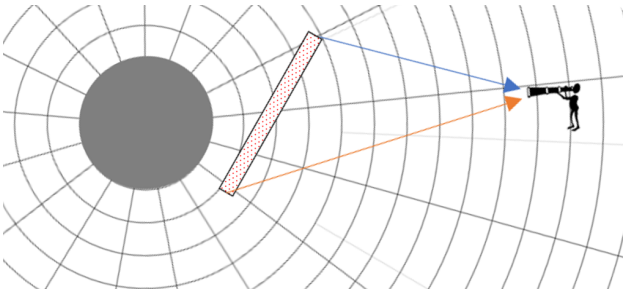

Figure 3: An observer observing the photons leaking from a photon gas column near a massive body

However, it is well known that as photons traverse a gravitational well, they lose energy and undergo a redshift in wavelength. In the case of a static, spherically symmetric gravitational field—that is, Schwarzschild geometry—the expression

for gravitational redshift is well established and takes the form:

$$\frac{\lambda_\infty}{\lambda_e} = \left(1 - \frac{R_s}{r}\right)^{-1/2}$$

where λ_e is the wavelength at emission, λ_∞ is the wavelength observed at infinity, $R_s = 2GM/c^2$ is the Schwarzschild radius of the massive body and r is the radius at which the photon was initially emitted. For our observer situated a large distance away from the body, $\lambda_o = \lambda_\infty$ is given by -

$$\lambda_o = \lambda_e \left(1 - \frac{2GM}{c^2 r}\right)^{-1/2}$$

From Wien's Displacement Law, we know $\lambda_{o_{max}} T_o = \lambda_{e_{max}} T_e$. Therefore, the temperature recorded by the observer would be off by a factor of -

$$T_e = \frac{T_o}{\sqrt{1 - \frac{2GM}{c^2 r}}}$$

In our hypothetical scenario, however, different segments of the photon column reside at varying distances from the center of the massive body. As a result, photons originating from different heights should experience differing amounts of gravitational redshift. This variation would manifest in the observed blackbody spectra: rather than a uniform spectral distribution, the observer would detect intensity peaks shifted differently along the column.

This presents a clear contradiction. The assumption of thermal equilibrium implies a spatially constant temperature, yet the differential redshift demands otherwise. The only resolution is that the column must possess a temperature gradient—one that precisely compensates for the gravitational redshift. Only then would the observer perceive a consistent peak wavelength and, by extension, a constant temperature.

Thus, we are led to the conclusion that although the temperature of the photon gas is constant in time, it must vary with position. The locally measured temperature is, in equilibrium, a spatial function shaped by the geometry of the gravitational field.

$$T(r) = \frac{T_o}{\sqrt{1 - \frac{2GM}{c^2 r}}}$$

We were working in the Schwarzschild Geometry, the metric ($g_{\mu\nu}$) for which is

$$ds^2 = -\alpha c^2 dt^2 + \alpha^{-1} dr^2 + r^2(d\theta^2 + \sin^2\theta d\phi^2)$$

where,

$$\alpha(r) = \left(1 - \frac{R_s}{r}\right)$$

On comparing with our expression for locally measured temperature, it becomes clear that the Temperature gradient of the photon gas column follows the expression -

$$T(r) = \frac{T_o}{\sqrt{-g_{tt}(r)}} \tag{1}$$

where T_o is constant as described earlier (g_{tt} is the component of the metric tensor that serves as the coefficient of $c^2 dt^2$ term). It is important to note that the temperature gradient derived here is independent of time. This result is deeply counter-intuitive: although a spatial temperature gradient exists within the photon gas column, no heat flows

from the hotter to the cooler regions. Thermal equilibrium is preserved—not through uniform temperature, but through a precise balance between thermal variation and spacetime curvature.

As is often the case in relativity, one must be attentive to the distinction between what is measured locally and what is defined globally. Just as notions of length and time differ between frames, so too must we distinguish between local temperature—measured by an observer comoving with the system—and coordinate temperature, which describes the system in a broader geometric frame. While not standard terminology, this distinction helps clarify why a temperature gradient does not, in this context, imply thermal disequilibrium.

3.1 Connecting the Two Pieces

Earlier, using Maxwell's argument, we established that the presence of unequal temperature gradients between two columns at equilibrium would enable the construction of a perpetual motion machine—an outcome forbidden by the second law of thermodynamics. Separately, we showed that a photon gas must exhibit a temperature gradient in a gravitational field in order to remain in thermal equilibrium with respect to an external observer. By connecting these two observations, we arrive at a general result: the temperature gradient described by Eq.1 must hold for all materials in static spacetimes—not just photon gases.

The proof follows the same logic as before. Suppose, hypothetically, that only the photon gas column exhibits a temperature gradient, while a second column—say, one composed of an ideal gas—maintains uniform temperature at equilibrium. Placing the two columns parallel and in close proximity (see Fig. 4), and thermally connecting their bases, we recreate the conditions described in Fig. 2. Once again, a horizontal conducting rod between the two at some height would permit continuous heat flow and indefinite work extraction—a direct violation of the second law.

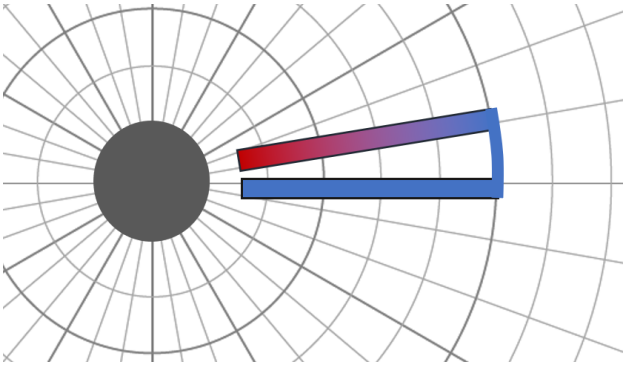

Figure 4: An observer observing the photons leaking from a photon gas column near a massive body

3.2 Universality of Gravity

To avoid the paradox of perpetual motion, we must conclude that all temperature gradients at thermal equilibrium within a given geometry must obey the same relation—namely, that described by Eq. 1. It is important to note, however, that this expression holds only in static spacetimes. The gradient itself arises from spacetime curva-

ture: gravity alters the conditions of thermal equilibrium, and therefore any form of matter or radiation that couples to gravity must experience the same temperature gradient. In the non-relativistic limit $c \to \infty$ the gradient would be indeed in the limit $\nabla T(r) \to 0$. This convergence reaffirms what we may now call the universality of gravity—its unique role in shaping equilibrium without violating thermodynamic laws.

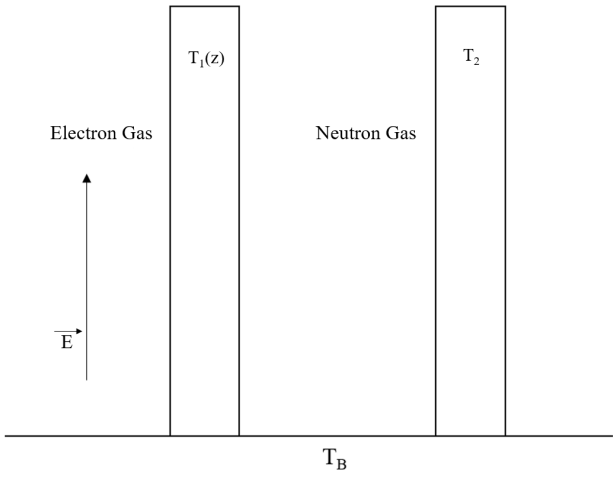

Figure 5: Electron Gas and Neutron Gas Columns Exposed to $\vec{E}$

Having established gravity's universality and its influence on equilibrium temperature distributions, we now turn to a natural question: can other fields, such as electromagnetism, give rise to similar temperature gradients? This next argument, adapted from [2], builds again on Maxwell's two-column setup. We consider a similar apparatus as described earlier with a few minor adjustments. Suppose one of the columns is filled with very low density electron gas and the entire apparatus is subjected to an Electric Field $\vec{E}$ as in Fig. 5. Does $\vec{E}$ produce a temperature gradient at thermal equilibrium? Let us begin, as before, by assuming that it does—and follow the consequences.

If there is a temperature gradient produced due to the electric field then it must only affect those particles that interact with $\vec{E}$ to have any causal relationship in the first place. If the adjacent column is made of non-interacting particles (such as Neutron Gas) then $\vec{E}$ has no causal influence over the second column. We are thus led to an unsettling situation: one column (electron gas) exhibits a temperature gradient at thermal equilibrium, while the other (neutron gas) does not. Having now invoked Maxwell's argument twice, this should raise immediate concern. But to make the contradiction explicit: if, at any given height in the apparatus, the two columns maintain unequal temperatures while in thermal equilibrium, one could insert a heat engine between them and extract work ad infinitum. This would violate the second law of thermodynamics.

The lesson generalizes: any force that does not act universally cannot produce temperature gradients at thermal equilibrium. Gravity alone satisfies this condition—coupling to all forms of energy and matter—and thus gives rise to the Tolman–Ehrenfest effect. The electric field, by contrast, is selective in its coupling, and therefore cannot reshape thermal equilibrium in this way.

4 Influence of Electric Fields on Temperature Gradients

It is important to note that in the preceding argument, the influence of gravity was deliberately set aside in order to isolate the effect of the electric field. Let us now reintroduce gravity and ask: Does the presence of an electric field modify the temperature gradient at thermal equilibrium once gravitational effects are taken into account?

Santiago and Visser have argued that electric fields do not directly contribute to the development of temperature gradients. However, to probe this question more carefully, we must turn our attention to how electric fields and gravity are intertwined in relativistic physics. Specifically, let us recall two of Maxwell's equations.

$$\nabla.\vec{E} = \frac{\rho}{\epsilon_0} \text{ and } \nabla \times \vec{E} = -\frac{\partial \vec{B}}{\partial t}$$

To sustain an electric field, there must exist either a charge density or a time-varying magnetic field. In other words, electric field lines must either terminate on electric charges or form closed loops governed by Faraday's law.

4.1 Reissner–Nordström Geometry

In general relativity, any entity possessing energy and momentum contributes to the curvature of spacetime. This includes not only massive particles, but also fields—such as the electromagnetic field. The simplest setting in which to study the gravitational influence of a massive, charged object is the Reissner–Nordström metric: a static, spherically symmetric solution to the Einstein-Maxwell equations. The spacetime geometry around such an object—a charged, non-rotating black hole—is described by the following line metric element:

$$ds^2 = -\Delta c^2 dt^2 + \Delta^{-1} dr^2 + r^2(d\theta^2 + \sin^2\theta d\phi^2)$$

where the coefficient Δ is

$$\Delta(r) = \left(1 - \frac{R_s}{r} + \frac{R_Q^2}{r^2}\right)$$

Like earlier, $R_s = 2GM/c^2$ is the Schwarzschild radius and $R_Q = (Q^2G)/(4\pi\epsilon_0 c^4)$ is a characteristic length defined by the net charge content of the body. Clearly, when we set $Q = 0$, we simply get a Schwarzschild geometry. If the black hole is also spinning, the geometry generalizes to the Kerr–Newman solution.

4.2 Are temperature gradients affected by $\vec{E}$?

We now return back to the original question - are temperature gradients at equilibrium (in static spacetime) affected by the presence of electric field? If the electric field could influence the temperature gradient at thermal equilibrium then it would allow for the existence of perpetual motion machines. Therefore, we rule out the possibility of a contribution by the electric field at thermal equilibrium. However, in static spacetimes, electric fields do not exist in isolation—they require a source, namely, electric charge. And

the presence of charge, as we have seen, alters the spacetime geometry. Since the metric affects the temperature gradient, the presence of $\vec{E}$ does indeed contribute to the temperature gradient-indirectly, through its gravitational imprint on spacetime.

In routine thermodynamic contexts, the resulting temperature gradients are extraordinarily small—whether or not charge is present. For all practical purposes, they can be neglected. But for the sake of logical consistency—and for the coherence of thermodynamics in curved spacetime—the Tolman gradient must exist. It is a quiet but essential feature of any complete theory.

5 Conclusion

This paper proposed a pedagogical aid to help early undergraduate students engage with the limitations of the conventional formulations of thermodynamic laws. It also offered a conceptual clarification regarding the causal relationship between temperature gradients at thermal equilibrium and the presence of electric fields. Upon carefully analyzing the role of electric fields—while keeping the universality of gravity in view—it was shown that electric fields can influence temperature gradients, but only indirectly, through their effect on spacetime geometry. Since this influence is mediated by gravity itself, the conclusion remains consistent with the broader principle: gravity is the only force capable of producing temperature gradients at equilibrium.

Although the magnitudes of these gradients are negligible in routine experiments, their very existence requires a reconsideration of the foundational statements of thermodynamics. The zeroth law's definition of temperature is not compatible with relativity, and the second law's prescription for the direction of heat flow is challenged by the possibility of stable gradients in equilibrium. Fortunately, the field of relativistic thermodynamics is mature, and such foundational tensions have been addressed within its framework.

6 Discussion

Talks based on this work that were delivered to undergraduate physics audience received encouraging feedback, particularly in stimulating interest in relativistic thermodynamics and introducing concepts not typically covered in undergraduate thermal physics courses. While a structured assessment (such as a short quiz following a dedicated lecture) could offer insight into the accessibility and comprehension of these ideas at the undergraduate level, a detailed data-driven pedagogical analysis lies outside the scope of the present paper.

Nonetheless, any effective teaching module should invite both forward and backward modes of self-directed learning. A forward approach builds on results presented in class, encouraging students to apply newly acquired tools to extended problems. This might involve reformulating

standard textbook exercises to include equilibrium temperature gradients, or exploring the role of relativistic thermodynamics in cosmology. A backward approach, by contrast, challenges foundational premises introduced without proof, prompting students to seek deeper theoretical grounding. This could involve studying Einstein's field equations to understand the gravitational role of the stress-energy tensor, or generalizing the Tolman result to stationary spacetime. The material presented here supports both trajectories, offering students an accessible yet conceptually rich path into the deeper structure of thermodynamics in curved spacetime.

Acknowledgments

The author would like to thank Prof. Vikram Vyas who suggested to me the Santiago and Visser reference [2] and Naxxatra for organizing a public lecture on the contents of this paper.

References

[1] Maxwell, James Clerk (1868) The London, Edinburgh, and Dublin Philosophical Magazine and Journal of Science 35

[2] Santiago, Jessica and Matt Visser (2018) Physical Review D 98

[3] Santiago, Jessica and Matt Visser (2018) The European Journal of Physics 40

[4] Tolman, Richard C and Paul Ehrenfest (1930) Physical Review 36

SOL-GEL: A simple method of Thin film deposition and Nano-particle growth

Sharmistha Lahiry[1]

[1]Associate Prof. of Physics, Sri Aurobindo College, University of Delhi, Delhi, INDIA
sharmistha.lahiry@gmail.com

Submitted on 02-06-2022

Abstract

Recent trend of miniaturization has emphasized the importance of thin films. This has led to development of various methods of thin film deposition. In this paper, Sol-Gel method of thin film deposition is discussed. It is a chemical method and does not require heavy or expensive equipments for thin films deposition. Moreover, it provides easy compositional control and modification, excellent control of stoichiometry, room temperature deposition with relatively low annealing temperature and possibility of film deposition on large area substrates. Interestingly, sol-gel method is being extensively used in preparing nano-particles of various compounds. Thin films, nano-particles, ceramics prepared by this method find industrial applications.

1 Introduction

Historically, sol-gel processing started with studies on silica gel way back in mid-1800s [1, 2]. This method had been widely used to prepare glass and poly-crystalline ceramics both as pellets and fibres. This method was also used to deposit films such as ITO (Indium Tin Oxide) and other similar compositions deposited on glass panes for insulation [3, 4]. The trend toward thin films began, in earnest, during 1970's but has recently accelerated, partly because newer techniques for producing high quality films have been developed and also because of a wide variety of applications of thin films. Thin films of different materials have some important advantages, such as, large capacitance, low switching voltage and the possibility of forming films directly on integrated semiconductor driving circuits [5, 6].

A detailed discussion of one of the fabrication method, namely, sol-gel technique, is presented here. Easy composition control and requirement of simple equipment makes it attractive for thin films fabrication. Recently, nano-particles of various materials have also been successfully prepared by this method. This method has been widely used to prepare oxide films of various materials for various applications like memory

devices, optical sensors, gas sensors, etc. [7].

The objective of this paper is to describe various steps of sol-gel process.

2 Fabrication Techniques

The various techniques used for thin film fabrication can broadly be classified into two categories: [5, 8]

1. Physical methods
2. Chemical methods

- Various Physical methods are:
    1. Thermal evaporation
    2. Sputtering : which can be high electric field (DC) sputtering, radio-frequency field (rf) sputtering and Magnetron sputtering
    3. Pulsed Laser Deposition (PLD)
    4. Molecular Beam Epitaxy (MBE)
- Various Chemical methods are
    1. Spray Pyrolysis
    2. Chemical vapour deposition (CVD). Some variations of this are Metal-Organic chemical vapour deposition (MOCVD) and Plasma enhanced metal-organic chemical vapour deposition (PE-MOCVD).

With the exception of sputtering method, all other fabrication techniques generally produce polycrystalline films which have properties more similar to ceramics than to single crystal.

Sol-Gel process has some important advantages which makes it quite attractive for thin film deposition as well as for forming powders for pellet or ceramic formation.These are :
(i)The excellent control of stoichiometry,
(ii) ease of compositional modifications,
(iii) relatively low annealing temperature,
(iv) possibility of film deposition on large area substrates
(v) simple and inexpensive equipments are required to deposit films on different substrates. The sol-gel method would allow the coating of more complex shapes and forms.
(vi) powders can easily be formed by drying the gel at suitable temperature which can then be pressed into ceramics. This can be accomplished at a lower temperature as compared to traditional ceramic processing methods and glass melting processes.
However, there are some disadvantages also such as substrate sensitive crystallization of films and difficulty of producing high quality films with thickness greater than $1\mu m$ or less than 100nm [9].

Now, we discuss the various steps of sol-gel process.

3 Sol-Gel Process

Let's first define a few terms used in this process, namely, Colloid, Sol and Gel. **Colloids** are solid particles that range in size from 1 to 100 nanometers. Colloidal particle are dispersed in the solvent to form **Sol**. **Gel** represents a colloidal or polymeric solid

containing fluid component which has internal network structure such that both the solid and the liquid components are highly dispersed. [10, 11]

Three methods are generally used to make sol-gel monoliths: (a) gelation of a colloidal powder solution, (b) hydrolysis and polycondensation of metal-nitrate or metal-alkoxide precursors solution. And then the gel is dried, (c) hydrolysis and polycondensation of a solution of metal-alkoxide precursor [10]. The solution is then aged and dried at an ambient condition.

3.1 Brief outline of steps

In the sol-gel technique, synthesis of an inorganic network is carried out by a chemical reaction of precursors in solvent and the solution so formed, at a comparatively lower temperature. The sol-gel process includes several steps [12], [10, 13] as given below:

(i) **Solution preparation** : In the first step, the solutes are dissolved in a suitable solvent to make a solution. The solutes may be inorganic nitrates, inorganic chlorides or a wide variety of metal-organic molecular compounds. The solvent can be water, a short chain aliphatic-alcohol, or an organic acid. For a multi-component composition, this step allows easy composition control.

(ii) **Formation of the sol** : When the solution is allowed to stand for some time sol is formed. Viscosity of the sol is more than that of a clear solution. If colloidal powders are available, they can be dissolved at a suitable pH which prevents precipitation so that a sol is formed directly as in the case of Silica gel [14, 15]. A solution of metal-alkoxide precursors is subjected to hydrolysis and condensation reactions in the solution. These then result in the formation of sufficient number of interconnected bonds which then behave as colloidal particles or sol.

(iii) **Gelation of the sol** :When the sol is allowed to stand for sufficient time, hydrolysis and condensation reactions continue resulting in the formation of gel. This process is called aging. An inorganic network can be formed by these reactions. The extent of cross-linking and the size of the particles affect the physical characteristics of the gel network. Viscosity increases sharply at gelation. Precipitation occurs when the size of the gel network is sufficiently large.

(iv) **Shaping of the gel**: Final gel shapes include spheres, fibres, powders, cubes, thin films etc. The gel can be given different shapes by controlling the time-dependent variation of the viscosity of the sol [16]. It has been shown that fibres can be drawn from a sol only for a range of viscosity greater than 1 Pa-sec [17, 18]. Films can be deposited only when the viscosity is much lower [4, 17, 18] . This is the key step in the sol-gel process.

(v) **Drying and firing of the gel**: The process of removing the solvent phase from the gel is called drying. The liquid in the pores are removed by evaporation. This results in shrinkage. The gel is dried by removing the physically adsorbed solvent. Firing refers to the conversion of the gel to a dense ceramic through pyrolysis. Powders can be formed at this stage which can be pressed to form ceramics. The resulting inorganic solid usually has an amorphous structure.

(vi) **Densification**: A post fired heat treatment of the gel results in further removal of the pores. This is required for further densification, grain growth and to obtain crystalline structure. In the case of thin films, annealing at higher temperatures results in the formation of crystallized films.

Now we discuss the steps enumerated in Section 3.1 a little extensively.

3.2 Solution Preparation

The starting chemicals which are compounds of the relevant components, acting as solutes in the sol-gel process are called precursors. The common compounds such as metal- chlorides, nitrates, acetates, acrylates, amines, hydroxides, if soluble in a solvent like water, aliphatic alcohols like methanol, ethanol, isopropanol, 2-methoxyethanol, etc., can be used as precursors. The requirement of sol-gel precursor is that they are soluble in the solvent and reactive enough to participate in the gel formation process [19].
Now, depending on the nature of the precursors, there are several preparation techniques available for the synthesis of materials by sol-gel processing technique. Some of the techniques are listed below [19].

3.2.1 All Metal Alkoxide Method

Metal alkoxides are regarded as the best precursors for sol-gel processing technique [19, 20, 21, 22]. Almost all metals form alkoxides, which have the general formula: $M(OR)_x$, where M is the metal, R is the alkyl group of the relevant alcohol and x is the valence state of the metal. Alkoxides are very reactive and readily hydrolyze to the corresponding hydroxides or oxides. The steps of hydrolysis can be represented as follows:

$$M(OR)_x + xH_2O \rightarrow M(OH)_x + xROH \quad (1)$$

Usually the product of hydrolysis is a polymeric gel which is formed through hydrolysis and condensation. Once the hydroxides are formed, condensation reaction may start through dehydration and dealcoholisation:

$$M(OH)_x + M(OH)_x \rightarrow M_2O_x + H_2O \quad (2)$$

$$M(OR)_x + M(OH)_x \rightarrow M_2O_x + xROH \quad (3)$$

However, all the above reactions tend to occur simultaneously, so that it is impossible

to describe the process by separate and independent hydrolysis and condensation reactions. The subsequent gelation can be achieved through a cross linking of M_2O_x of the polymer specimen thereby increasing the viscosity, either by removal of the solvent, or aging of the solution [12]. There is also a limited class of compounds known as double alkoxides. These contain two different metals in the same compound and have the general formula : $M'_xM''_y(OR)_z$. M'_x and M''_y are metals, R is an alkyl group and x, y, z are integers. The physical properties of the metal alkoxides can be varied by changing the alkyl group and for most metals, soluble products which can in some cases even be liquid, can be obtained. In addition, many alkoxides are volatile and therefore can easily be purified by distillation to get very pure products. Double alkoxides have the added advantage of not only being volatile but maintaining the exact molecular stoichiometry within the metals [12]. The fabrication of a multicomponent system involves the preparation of a solution using all the metal components as the precursors in a suitable organic solvent and then reacting with water to form the oxide complex. The reaction can be represented for a three component system as follows [23, 3, 4]:

$$M(OR)_a + M'(OR)_b + M''(OR)_c \rightarrow MO_{a/2} + M'O_{b/2} + M''O_{c/2} + yROH \quad (4)$$

As the number of components increases, the mechanism of the hydrolysis and condensation reactions become more complex.

3.2.2 Alkoxide-Salt Method

Alkoxides of some metals are not commercially available due to some preparation problems. In these cases, the metal salts provide an alternative as they can be readily converted to the oxide by thermal or oxidative decomposition and are perfectly soluble in organic solvents. Thomas et.al.[19] found that some metal-acetates react with some metal-alkoxides to form metallometaloxane derivatives with the liberation of alkyl acetate:

$$M(OR)_n + M'(OAc)_m \rightarrow (OR)_{n-1}M- O - M'(OAc)_{m-1} + ROAc \quad (5)$$

where Ac represents the group $-COCH_3$. The reaction then continues with further reaction of acetate and alkoxide groups resulting in an increase molecular weight of the product[24].

Sol-gel technique involving salts are usually more complex than those with only alkoxides because the hydrolysis of the alkoxides is more easily accomplished than the thermal or oxidative degradation required of the metal salts[24].

Rate of hydrolysis and condensation reactions can be controlled by addition of various catalysts. Generally catalysts used are acid, base and acid-base catalysts [25, 26, 27, 28, 29, 30, 31, 32] .

3.3 Shaping of the gel

The gel formed can be used in various forms. Thin films are usually formed by spin coating onto various substrates. The smoothness of the film is controlled by the spin rate and the viscosity of the solution. Thin films can also be formed by dip coating of the gel. At an appropriate viscosity of the solution, the uniformity and the thickness of the film are maintained by controlling the rate at which the film is pulled out of the gel. The gel can also be dried and formed into powders which can be shaped into ceramic discs.

3.4 Thin film Deposition

Spin coating is one of the most commonly used method of sol-gel film deposition. This method is used in deposition of nano-scale or micro-scale thickness films on various substrates like glass, quartz, single crystal substrates, Silicon, Platinized silicon, etc. using a Spinner. It's widely used in photolithography to deposit one-micrometre-thick layers of photoresist and planar photonic structures of polymers [30].

Using a nozzle or a dropper, a little amount of the solution is poured onto the substrate. At this point, an extra amount of coating solution must be put over the substrate in comparison to the final amount of solution necessary for coating, so that the solution completely wets the surface and the substrate is fully covered. The substrate is then spun at speeds up to $10,000$ rpm with a spinner to disperse the coating material by centrifugal force. Thickness of the film is dependent on the concentration and viscosity of the solution as well as on the speed of rotation of the spinner. Thinner films are obtained at a higher speed. As the rotational speed of the substrate is increased from zero to the final required speed, the rotational motion causes aggressive fluid expulsion from the substrate. Spiral vortices can occur briefly as a result of the twisting motion generated by the inertia exerted by the top of the fluid layer as the substrate beneath rotates faster and faster. The fluid eventually thins out to the point where it can entirely co-rotate with the wafer, and any sign of a fluid thickness difference vanishes. The substrate eventually reaches the appropriate speed, and the fluid is thin enough that the rotating accelerations are perfectly balanced by the viscous shear drag. Fluid viscous forces dominate fluid thinning behaviour when the substrate spins at a constant pace, which is slow and generally uniform. Interference colours spinning off can be visible at this point in solutions containing volatile liquids. Since the fluid flows uniformly outward it must form droplets at the edge to be tossed off, and edge effects are also visible at this stage. When the substrate is rotating at a steady speed after this stage, solvent evaporation takes precedence over coating thinning. The evaporation of any volatile solvent becomes the dominat-

ing process in the coating at this time. The coating effectively gels at this point because the residual solution's viscosity rises as the solvents are withdrawn, thus freezing the film in place. The coating thickness is dependent on the rate of spinning, viscosity of the solution [33].

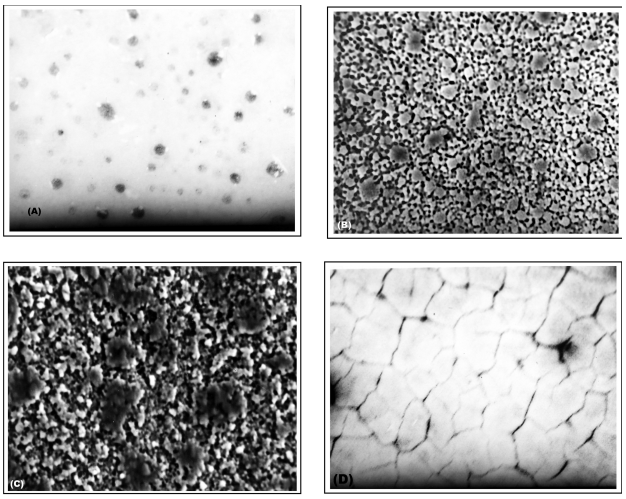

Figure 1: Scanning electron micrographs of Barium-Strontium Titanate $Ba_{0.4}Sr_{0.6}TiO_3$ films (A) amorphous (B) annealed at 700°C, (C) annealed at 800°C, (D) cracked films, deposited by sol-gel method on Pt/Si substrate.

The consistency of the film thickness is an important advantage of spin coating thin films. Thickness does not change by more than 1 % due to self-levelling. However while coating thicker sols of polymers or photoresist films,large edge beads can be formed.

Figure 1 shows the scanning electron micrographs (SEM) of the Barium-Strontium Titanate $Ba_{0.4}Sr_{0.6}TiO_3$ films deposited by sol-gel method on Platinized-Silicon (Pt/Si) substrate [34]. Films shown in figure 1(A), (B),(C) had a thickness of 50nm. Figure 1(A) shows that the as-deposited/as-fired films were amorphous in nature. Crystalline films were obtained by annealing the films at higher temperature. Figure 1(B),(C) show films annealed at 700°C and 800°C respectively. Well formed grains can be seen in both these cases.

3.4.1 Cracking behaviour of Sol-Gel films

A major problem in the sol-gel process is cracking and delamination of films during drying [35]. Cracking occurs mainly due to large shrinkages which occur during drying. And, the shrinkage can occur in two dimension only since the films must attach to the substrate.Viscosity of the solution and thickness of the films are other major factors resulting in cracking. Multiple coating followed by firing of films is done to avoid cracking. Figure 1(D) shows cracked film. The film was 1.2μm thick.

3.5 Synthesis of Nano-particles by Sol-Gel Method

Sol-gel method is one of the industrial methods of preparing nano-particles. When the sol is allowed to stand for sufficient time, a gel is formed. This is also called wet-gel.Depending on the drying conditions of the wet-gel two types of dried-gels can be obtained, namely aerogel and xerogel [36]. If the pore-liquid is removed from the

wet gel under special drying conditions, a highly porous and a low density gel is formed called aerogel [10] [36]. Aerogels have nano-meter scale pores, high internal area and very low density [37] [25]. Drying of wet gel to form areogels is generally done by supercritical method, subcritical method or by sublimation process [25]. In super-critical method the wet gel is dried under critical temperature and pressure to remove the solvent from the system as gas. This process can also be carried out at low temperature or at high temperature. When the process is carried out at low temperature the pore-liquid is first replaced with a liquid such as CO_2 which is then removed at an ambient temperature and pressure [38]. In case of high temperature super-critical drying the solvent is directly removed from the wet-gel at critical temperature and pressure. The pressure and temperature are adjusted in such a way that the network does not collapse and the structure is maintained. Chemical additives like glycerol, formaldehyde, oxalic acid, tetramethylammonium hydroxide are used to control the drying process. In the sublimation or freeze drying method, the liquid inside the gel is first frozen and then dried by sublimation. Drying at ambient pressure is generally used on an industrial scale [36]. Xerogels are formed by drying the gels under normal conditions. The main difference between aerogel and xerogel are in the size and number of the cavities. Aerogels have very low thermal conductivity due to highly porous structure of these nano-materials. Nano-scale powders are formed by this method. Usually the powders so formed are amorphous in nature which can be crystallized by annealing or sintering them at higher temperature.

Wet chemical method has long been used to prepare mixed ferrites. Recently, the method has been specifically used to prepare nano-particles of mixed ferrites. The method is also called co-precipitation method. The method, in brief, involves the preparation of solutions of different metal salts such as sulphates, chlorides, nitrates, etc., in appropriate ratios, which are then mixed to form a solution. An alkali solution of sodium hydroxide or potassium hydroxide or a base like ammonia is prepared in appropriate concentration. For simultaneous or co-precipitation of metal-hydroxides, the prepared metal solution is added dropwise to the alkaline solution.The suspension of metal hydroxides, so obtained, is usually heated to a temperature of $60 - 80^{\circ}C$ and oxygen gas is bubbled through the suspension along with mechanical stirring to convert ferrous iron into ferric state. The precipitate is filtered, washed repeatedly and dried at 130°C. The dried material is sintered at approximately 700°C to obtain the desired mixed ferrites. The nano scale powders of ferrites can be obtained by this method [39, 40, 31, 41, 42, 43]. Jadhav et.al. [39, 40] made a detailed study of the ferrite nano-materials so prepared. A series of substituted ferrites

of composition $Co_{1-x}Zn_xFe_2O_4$ with x varying from 0.0 to 0.7 was prepared by them by wet chemical or co-precipitation method. the samples were characterized by X-ray diffraction and magnetization studies. Results revealed nano size of the ferrites prepared. Jadhav et.al.[26] also reported ferrite nano-particles prepared by sol-gel autocombustion method in which nitrates of suitable metal ions and a suitable chelating agent or fuel, such as citric acid, urea, glycine, etc., were used as starting material. Ammonium hydroxide was added to the aqueous solution of metal nitrates and the chelating agent. Detailed preparation method is given by Shirsath et.al.[26] Singh et.al.[31]. Particle size, magnetic properties depends on the chelating agent to nitrate ratio and type of chelating agent used [26, 44]. Nanoparticles of mixed and simple ferrites were prepared and studied by this method.

3.6 Applications of Sol-Gel Deposited films and nano-particles

Historically sol-gel method was used to make silica gel glasses [1, 2]. Indium TinOxide (ITO) films deposited by sol-gel method were used as anti-reflection coatings [3, 4].

This method has been extensively used to deposit dielectric and ferroelectric films. Those films have found a wide range of applications using the ferroelectric, piezoelectric, pyroelectric, electro-optic properties of these materials [6]. Ferroelectric films in the paraelectric phase at room temperature have been used in large capacitors for DRAM (Dynamic random access memory) and the films in the ferroelectric phase as memory capacitors [6, 5, 45]. These films have applications in tunable phase shifters, integrated microwave devices, optical applications, infra-red detectors, gas sensors, light sensors as photodiode, solar cells, glucose sensors[46, 47, 48, 49, 50, 51, 52, 53, 54, 55, 56]. Materials like alumina prepared by sol-gel method has been used in medical field as carriers for drug delivery [57, 58, 59]. Recently Barium-Strontium-titanate films have been used as glucose-sensor [53].

Recent interest in nano particles makes sol-gel attractive as the particle size is generally in the nano-meter range. Ease of composition control and variation makes sol-gel an attractive method for uniform and ultra-fine ceramic powders. These nano-scale sized particle find applications in biomedical and dental applications, herbicides, agrochemicals, powder abrasives for finishing operations [60]. Also ease of assimilation of various particles makes it easy to incorporate nano-particles in the material modifying the characteristics of the material.

Sol-gel method is used to fabricate various ceramic membranes for microfiltration, nanofiltration, ultrafiltration, reverse osmosis. By drying the gel under suitable condition it is possible to obtain porous solid ma-

trices which can be used as membranes. In 1950's sol-gel process was used to make radioactive powders of UO_2 and ThO_2 for nuclear fuels.

References

[1] M.Ebelmen, "On synthesis of silica gels from alkoxides" Ann. Chimie. Phys., **16**, 129 (1846).

[2] T. Graham, "On the properties of silicic acid and other analogous colloidal substances" J. Chem. Soc., **17**, 318 (1864).

[3] H. Dislich, "Sol-Gel 1984-2004(?)" J. Non-Cryst. Solids, **73**, 599, (1985).

[4] H. Dislich, P. Hinz, "History and principles of sol-gel process, and some new multicomponent oxide coatings" J. Non-Cryst. Solids, **48**, 11, (1982).

[5] Ed. K. L. Chopra, I. Kaur *Thin film Device Applications* (Springer 1983)

[6] N. Setter, D. Damjanovic, L. Eng, G. Fox, S. Gevorgian, S. Hong, a. Kingon, H. Kohlstedt, N. Y. Park, G. B. Stephenson, I. Stolitchnov,A. K. Taganstev, D. V. Taylor, T. Yamada, S. Streiffer, "Ferroelectric thin films : Review of materials, properties and applications" J. Appl. Physics, **100**, 051606 (2006). https://doi.org/10.1063/1.2336999

[7] A. C. Pierre, *Applications of sol-gel processing, Introduction to sol-gel processing, Springer* p597-685 (2020).

[8] Ed. K. Seshan *Handbook of thin film deposition* (Elsevier Publication, 2021)

[9] G. Yi and M. Sayer, "Sol-gel processing of complex oxide films" Ceramic Bulletin ,**70** (7) pp 1173 (1991).

[10] L.L. Hench and J.K. West, "The Sol-Gel process" Chemical Rev., **90**, 32-72, (1990).

[11] B.J.J. Zelinski, D. R. Uhlmann, "Gel technology in Ceramics" Jr. of Phys and Chem. of Solids. (1984)

[12] J. Livage and C. Sanchez, "Sol-gel chemistry" Jr. Non-Cryst. Solids, **145**, 11-19, (1992).

[13] J. Livage, "Sol-gel processes" Current Opinion in Solid State and Material Science, **2**, 132, (1997).

[14] R. K. Iler *The Chemistry of Silica, Wiley, New York* (1955).

[15] R. K. Iler *The Chemistry of Silica, Wiley, New York* (1979).

[16] G. Orcel, L.L. Hench, I. Artaki, J. Jones, T. W. Zerda, "Effect of formamide additive on chemistry of silica sol-gels II, Gel structure" J. Non-Cryst. Solids,**105**, 223 (1988).

[17] S. Sakka, K. Kamiya, "The Sol-Gel transition in the hydrolysis of metalalkoxides in relation to the formation of glass fibers and films" J. Non-Cryst. Solids, **48**, 31-34 (1982).

[18] S. Sakka, K. Kamiya, K. Makita, Y. Yamato,"Formation of sheets and coating films from alkoxide solution" J. Non-Cryst. Solids, **63**, 223-235 (1984).

[19] I. M. Thomas; *Sol-Gel Technology for thin Films and Fibres Reforms, Electronics and Speciality shapes (Noyes, New Jersey)* (1998).

[20] K.Y. Chen, L. L. Lee and D.S. Tsai, "Barium and Strontium Titanate films from hydroxide alkoide precursors" Jr. Mat. Science Lett., **10**, 1000-1002, (1991).

[21] H. Dislich; "New routes to multicomponent oxide glasses" Anjew. Chem., **10**, 363-370 (1971)

[22] B. Samuneva, V. Kozhukharov, C.H. Trapalis and R. Kranold, "Sol-gel processing of titanium containing thin coatings" J. Mat. Science., **28**, 2353-2360, (1993).

[23] H. Schroeder and G. Gliemeroth; US Patent 3597, **252** (1971).

[24] J. Yoon, "Fabrication and characterization of ferroelectric oxide thin films" *Handbook of thin films* (2002).

[25] S. Dervin and S.C. Pillai,"An introduction to sol-gel processing for aerogels" *Sol-gel materials for Energy, Environment and Electronic Applications, Advances in Sol-Gel Derived Material and Technologies* Eds. S.C. Pillai and S. Hehir, Springer Interrnational Publishing, 1-22, (2017). https://DOI 10.1007/978 − 3 − 319 − 50144 − 4 − 1

[26] S.E. Shirsath, D. Wang, S.S. Jadhav, M.L. Mane and S. Li, "Ferrites obtained by sol-gel method" L. Klein (eds.) *Handbook of Sol-Gel Science and Technology*, Springer International Publishing AG, 695-735, (2018). *https* : *//doi.org*/10.1007/978 − 3 − 319 − 32101 − 1 − 125

[27] A.V. Rao, G. Pajonk, N. Parvathy, "Effects of solvents and catalysts on monolithicity and physical properties of silica aerogel"J. Mater. Sci., **29**, 1807-1817 (1994).

[28] B. Karmakar, G. De, D. Ganguli, "Dense silica microsperes from organic and inorganic acid hydrolysis of TEOS", J. Non-Cryst. Solids, **272**, 119-126 (2000).

[29] A.V. Rao and S.D. Bhagat, "Synthesis and physical properrties of TEOS-based silica aerogels prepared by two step (acid-base)sol-gel process" Solid State Sci., **6**, 945-952, (2004).

[30] C. J. Brinker,K. D. Keefer, D.W. Schaefer, C. S. Ashley. "Sol-Gel Transition in Simple Silicates", J. Non-Crystalline Solids, **48**, 47-64 (1982).

[31] V.P. Singh, R. Jasrotia, R. Kumar, P. Raizada, S. Thakur, K.M. Batoo, M. Singh, "A current review on the synthesis and magnetic properties of M-type hexaferrites materials" World J. Cond. Mater Phys., **8**, 36-61 (2018) *DOI* : 10.4236/*wjcmp*.2018.82004

[32] C.R. Silva and C. Airoldi "Acid and base catalysts in the in the hybrid silica sol-gel process" J. of Colloid and Interface Sc., **195**, 381-387 (1997).

[33] Meyerhofer, "Characteristics of resist films produced by spinning" Jr. Appl.Phys., **49**, 3993-3997 (1978).

[34] Sharmistha Lahiry : unpublished SEM photographs of $Ba_{0.4}Sr_{0.6}TiO_3$ films.

[35] R. M. Guppy, A. Atkinson, "The cracking behaviour of sol-gel films", British Ceramic proceedings, **49**, 203-214, (1992).

[36] D. Bokov, A.T. Jalil, S. Chupradit, W. Suksatan, M.J. Ansari I.H. Shewael, G.H. Valiev and E. Kianfar, "Nanomaterial by sol-gel method: Synthesis and Application" Advances in Mat. Sc. and Engineering, **2021** (2021). *https* : *//doi.org*/10.1155/2021/5102014

[37] S.B. Riffat and G. Qiu, "Areview of state-of-the-art aerogel applications in buldings" Int. J. Low-Carbon technol. **8**, 1-6, 2013.

[38] P.H. Tewari, A.J. Hunt and K.D. Lofftus, "Ambient temperrature supercritical drying of transparent silica aerogels" Mater. Lett. **3**, 363-367 (1985).

[39] S.S. Jadhav, S.E. Shirsath, B.G. Toksh, S.M. Patange, S.J. Shukla and K.M. Jadhav, "Structural properties and cation distribution of Co-Zn nanoferrites" Int. Jr. Mod. Phys.B, **23**, 5629-5638 (2009). *DOI* : 10.1142/*S*021797920905225*X*

[40] S.S. Jadhav, S.E. Shirsath, S.M. Patange and K.M. Jadhav, "Effect of Zn substitution on magnetic properties of nanocrystalline cobalt ferrite" J. Appl. Phys., **108**, 093920, (2010).

[41] D. Lisjak and M. Drofenik, "Mechanism of low temperature formation of Barium hexaferrite" J. European Ceramic Soc., **27**, 4515-4520 (2207). *https* : *//doi.org*/10.1016/0955 − 2219(94)90072 − 8

[42] J.P. Wang, L. Ying, M.L. Zhang, Y.J. Qiao and X. Tin, "Comparison of the sol-gel method with the coprecipitation technique for preparation of hexagonal Barrium Ferrite" Chem Res. in Chinese Univs., **24** 525-528 (2008). *https* : *//doi.org*/10.1016/*S*1005 − 9040(08)60110 − 5

[43] V. Harikrishnan, P. Saravanan, R.E. Vizhi, D.r. Babu, V. Vinod, P. Kejzlar and M. Cernik "Effect of annealing temperature on the structural and magnetic properties of CTAB capped $SrFe_{12}O_19$ platelets" J. of Magnetism and Magnetic Mat., **401** 775-783 (2016). *https* : *//doi.org*/10.1016/*j.mmm*.2015.10.122

[44] T. Slatineanu, E. Diana, V. Nica, V. Onacea, O.F. Caltum, A.R. Jordan and M.N. Palamaru, "Influence of the chelating/combustion agents on the structure and magnetic properties of zinc ferrite", Cent. Eur.J.Chem. **10**, 1799, (2012).

[45] F.L. Traversa, F. Bonani , Y.V. Pershin and M. Di Ventra, "Dynamic Computing Random Access Memory" Nanotechnology, **25**, 285201 (2014).

[46] L.C. Sengupta, S. Sengupta, "Novel ferroelectric materials for phased array antennas" IEEE Transactions on Ultrasonic Ferroelectric and Frequency control, **44**, (6) 792-797 (1997).

[47] A. Outzourhit, J.U. Trefny, T. Kito, B. Yarar, "Tunability of the dielectric constant of $Ba_{0.1}Sr_{0.9}TiO_3$ ceramics in paraelectric state" J. Mater. Res., **10**, 1411 (1995).

[48] N.A.Vainos, M.C. Gower, "High-fidelity phase conjugation and real-time orthoscopic three dimensional image projection in $BaTiO_3$" J Opt Soc Am B, **8**, 2355-2362 (1991).

[49] Irzaman, R. Siskander, Aminullah and H. Alatas, "Characterization of Barium Strontium Titanate films as light and temperature sensors and its implementation on automatic drying system model", Integrated Ferroelectrics, **168**, 130-150 (2016). DOI:10.1080/10584587.2016.1159537.

[50] F. Faridawati, A. Y. Rohedi, E. Minarto, G. Yudoyono, T. Widihartanti, YH Pramono, N Yuningtyas, "The Comparison of optical properties between $Ba_{0.25}Sr0.75TiO_3$ and $Ba_{0.75}Sr_{0.25}TiO_3$ thin films as the light sensor application", Jr. of Physics: Conference Series **1825**, 012079 (2021). DOI10.1088/1742-6596/1825/1/012079.

[51] J. Iskander, H Syafutra, J. Juansah and Irzaman,"Characterization of electrical and optical properties on ferroelectric photodiode of Barium strontium titanate $(Ba_{0.5}Sr_{0.5}TiO_3)$ films based on annealing time difference and its development as light sensor on satellite sensor technology", Procedia Environmental Sciences **24**, 324-328 (2015).

[52] V. Kavitha, V. Raghavendran, N Sethupathi, S. Sagadevan, V.Sasirekha, J.M.Pearce and J. Mayaandi, "Microwave assisted synthesized Gadolinium Doped Barium Strontium titanate Nanostructures: Structural and Optical properties for DSSC applications", Malaysian Nano-An International Journal, **1**, 71-82 (2021).

[53] E.K. Palupi, H. Alatas, Irzaman, Y. Suryana, A. Aridarma, R. Umam, B.B. Andriana and H. Sato, "Optimization of Optical properties of $Ba_{0.2}Sr_{0.8}TiO_3$ thin films for a glucose sensor implementation" Biomedical Spectroscopy and Imaging **9**, 63-71 (2020).

[54] S. Lahiry and A. Mansingh, "Sol-Gel derived $Ba_xSr_{1-x}TiO_3$ films for microwave applications" Ferroelectrics **329**, 39-42, (2005).

[55] P. Amrit, S. Jain, M. Tomar, V. Gupta, B. Joshi, "Synthesis and characterization of sol-gel derived non-toxic CZTS thin films without sulfurization" International Jr. of

Applied Ceramic Technology, **17** 1194-1200, (2020).

[56] R. K. Sonker, B. C. Yadav, V. Gupta, M. Tomar, "Synthesis of CdS nanoparticles by sol-gel method as low temperature NO_2 sensor", Materials Chemistry and Physics, **239**, 121975-121976 (2020).

[57] K.Volodina, "A synergistic biocomposite for wound healing and decreasing scar size based on sol–gel alumina" RSC Advances. **4** 60445–60450 (2014). *doi* : $10.1039/C4RA09015B$.

[58] V.V.Vinogradov , A. V. Vinogradov, V. E. Sobolev,I.P. Dudanov,V. V. Vinogradov "Plasminogen activator entrapped within injectable alumina: a novel approach to thrombolysis treatment" Journal of Sol-Gel Science and Technology. **73** 501–505 (2014). $doi : 10.1007/s10971 - 014 - 3601 - 4$.

[59] V. V.Vinogradov, D. Avnir, "Exceptional thermal stability of industrially-important enzymes by entrapment within nano-boehmite derived alumina" RSC Adv. **5** 10862–10868 (2015). *doi* : $10.1039/C4RA10944A$

[60] R. Gupta, N. K. Chaudhary, Chaudhary, "Entrapments of biomolecules in sol-gel matrix for applications in biosensors : problems and future prospects" Biosens Bioelectron, **22** 2387-99 (2007).

Some Applications of Lorentz Oscillator Model

Vishwamittar

Retired from Department of Physics, Panjab University, Chandigarh – 160014.
Contact Address: #121, Sector-16, Panchkula – 134113 (Haryana).
email address: vm121@hotmail.com

** The article is dedicated with immense reverence to late Nana ji (Sh. Bhagwan Das Ji), late Taya Ji (Sh. Jai Dayal Ji & Sh. Chetananand Ji), late phoopha Ji (Sh. Issar Das Ji) and late Maan Ji (Smt. Lachhmi Devi Ji).*

Submitted on 27-01-2023

Abstract

This article is devoted to the description of the Lorentz oscillator model, which refers to the classical concept that electrons in an atom behave as forced damped harmonic oscillators under the influence of an oscillating electric field. This idea has been used to derive expressions for complex dielectric function, complex refractive index and normal incidence reflectivity and their detailed analysis. These quantities have also been discussed for the Drude model for metals, which can be considered as a special case of the Lorentz model. Some typical applications of these models and their combination have also been dealt with. The fascinating thing about these models is that despite being classical in nature they lead to reasonably reliable results for otherwise quantum mechanical systems. An effort has been made to present the material in a pedagogical manner so that it can be easily followed by undergraduate students.

1 Introduction

The 1902 physics Nobel laureate Lorentz (July 18,1853 – Feb. 4, 1928) became a cynosure in the history of physics by 'completing what was left unfinished by his predecessors and preparing the ground for the fruitful reception of new ideas based on the quantum theory' [1]. His outstanding contributions are refinement of Maxwell's electromagnetic theory including works in optics; general theory of electrical and optical phenomena of moving bodies; derivation of Lorentz force law which describes dynamics of a charged particle in the presence of electric and magnetic fields; insightful conceptualization of electron, its mathematical theory and use to explain Zeeman effect (the splitting of atomic spectral lines in the presence of magnetic field); and ingenious idea of local time and derivation of Lorentz transformations (which can be used to calculate the earlier proposed
Lorentz-Fitzgerald length contraction) that constitute the natural outcome of Einstein's special theory of relativity. Even before the discovery of electron in 1897, he argued that atoms are composed of charged particles and that the light originated from their oscillations in an atom. Later, he proposed the so-called Lorentz oscillator model (LOM) to account for the anomalous dispersion in dielectric substances in the framework of classical physics. Besides, he published research papers on general theory of relativity and delivered lectures on Schrödinger's wave mechanics. Interestingly,

he spent nearly eight years in developing mathematical models for flood control dams in his country, the Netherlands, and his findings have been recognized
as one of the greatest works in hydraulic engineering. In fact, the dictum 'talent hits a target that others miss, and genius hits a target that others do not even see' by the celebrated 19th century German philosopher Schopenhauer appropriately describes spectacular creative work carried out by the legendary Lorentz.

In the end of 1905, when the structure of atoms was not yet established, Lorentz in his paper entitled 'The absorption and emission lines of gaseous bodies', put forward the idea that in the presence of an oscillating electric field, electrons in an atom behave as driven velocity-dependent-damped harmonic oscillators – the LOM [2]. The formulae derived by using the time-dependent position vector of these electrons quite well describe the electric polarization and, hence, dielectric function and optical properties of various types of materials [3-12]. In other words, the LOM provides a classical theory for understanding interaction between electromagnetic (e.m.) radiation and matter. It is indeed amazing that despite being a completely classical concept, in later works, this model fitted adequately in the realm of quantum mechanics and has been fruitfully used in analyzing various electrical and optical properties of insulators, undoped as well as doped semiconductors, and ionic crystals [3,6,9,10,12]. In fact, strictly speaking all these features of solids are properly explained in terms of band structure, which is an outcome of their quantum mechanical description.

Recently, with a view to incorporating some quantum mechanical aspects in the formalism of this model, the oscillator has been quantized using the Bohr and the Bohr-Sommerfeld theories and quantum mechanical selection rules, establishing relationship between the oscillator impedance and the energy eigenvalues of hydrogen-like atoms [13,14]. Model so obtained has been named quantum impedance Lorentz oscillator by the authors - Zhao and coworkers. They have shown that their modified model can be used to analyze linear and nonlinear properties of many dielectric materials containing hydrogen-like atoms.

However, prior to introduction of LOM, Drude (1900, just 3 years after the discovery of electron), in his publication on 'electron theory of metals', assumed that a metal is composed of positively charged immobile particles submerged in a sea of mobile negatively charged electrons. He treated the motion of electron gas as classical entities under the influence of constant uniform electric field in the framework of kinetic theory, with positive particles as scattering centers and obtained an expression for DC conductivity of metals. In fact, the Drude model (DM) can be treated as a special case of LOM and has been found to be very useful in getting insight into the optical properties of metals.

It is interesting to note that despite their numerous shortcomings, a combination of DM and LOM is quite commonly used to analyze experimental data for optical properties of conducting materials. It is usually referred to as Drude-Lorentz Oscillator Model (DLOM). Besides, some improved versions making use of the concepts of these models and even including confining potentials have also been developed. These are applicable not only to bulk materials but also to nanoparticles and systems falling under the purview of nonlinear optics. Of course, these have their own merits and demerits. Some of the relevant references have been well summarized in [15]. It may also be mentioned that some softwares based on the LOM and DLOM are available for analysis of optical spectra of solids.

The principal purpose of this article is to delineate upon LOM and derivation of expressions for different electric and optical quantities, and to discuss the DM for metals (as a special case of LOM). In fact, both these models provide fairly good qualitative results for some solids and are, therefore, quite useful in making preliminary predictions. Some illustrative examples of these models and DLOM have also been included.

2 The Lorentz Oscillator and its Solution

Following Lorentz, we take an atom to be composed of an electron of electric charge $-q$ and mass m bound to an infinitely massive stationary nucleus / positive ion core by a hypothetical spring characterized by force constant k. On being slightly displaced from its equilibrium position, the classically treated electron executes simple harmonic motion of natural or free angular frequency $\omega_0 = \sqrt{k/m}$. Sometimes, the characteristic frequency ω_0 is referred to as fundamental or resonant frequency. This oscillatory motion experiences a velocity-dependent viscous resistance or damping, with coefficient γ, caused by collisions, radiative losses, etc. In the presence of an external harmonic electric field of angular frequency Ω, $\boldsymbol{E}(t) = \boldsymbol{E_0}e^{-i\Omega t}$(as it occurs in the description of travelling e.m. waves), the electron becomes a driven damped harmonic oscillator described by the following equation of motion,

$$\ddot{\boldsymbol{r}}(t) + \gamma\dot{\boldsymbol{r}}(t) + \omega_0^2\boldsymbol{r}(t) = -\frac{q}{m}\boldsymbol{E_0}e^{-i\Omega t}. \quad (1)$$

Here, $\boldsymbol{r}(t)$ is the instantaneous displacement of the electron from its equilibrium position. Note that γ has dimension of inverse time and is, therefore, also called damping rate. It may be pointed out that the Lorentz force arising from the interaction of electronic charge with the magnetic field of an e.m. wave has been omitted because the electron velocity is very small as compared to the speed of light.

As demonstrated in the Appendix, for sufficiently large times the complementary solution of Eq. (1) giving rise to transients will vanish and only the particular integral, is left. Thus, the steady state solution can be written as

$$\boldsymbol{r}(t) = -\frac{q}{m}\frac{1}{(\omega_0^2-\Omega^2)-i\gamma\Omega}\boldsymbol{E_0}e^{-i\Omega t} = -\frac{q}{m}\left\{\frac{(\omega_0^2-\Omega^2)+i\,\gamma\Omega}{(\omega_0^2-\Omega^2)^2+(\gamma\Omega)^2}\right\}\boldsymbol{E_0}e^{-i\Omega t}. \quad (2)$$

We have not used any subscript with $\boldsymbol{r}(t)$ to indicate steady state, for convenience. Note that in this state the electron oscillates with the angular frequency Ω of the field. In fact, explicit dependence of $\boldsymbol{r}(t)$ on Ω is quite clear from Eq. (2). Furthermore, it is implicitly assumed that the motion of the electron is such that it is always associated with the same nucleus / ion core.

Writing $(\omega_0^2 - \Omega^2) = A\cos\theta$ and $\gamma\Omega = \mathrm{A}\sin\theta$ so that $A = \{(\omega_0^2 - \Omega^2)^2 + (\gamma\Omega)^2\}^{1/2}$ and $\theta = tan^{-1}\{\gamma\Omega/(\omega_0^2 - \Omega^2)\}$, Eq. (2) becomes

$$\boldsymbol{r}(t) = -\frac{q}{m}\frac{1}{\left\{(\omega_0^2-\Omega^2)^2+(\gamma\Omega)^2\right\}^{1/2}}\boldsymbol{E_0}e^{-i(\Omega t-\theta)}. \quad (3)$$

It may be noted that the complex nature of the amplitude in Eq. (2) has been taken care of by introducing the phase angle θ. Furthermore, Eq. (3) shows that at any time t, the displacement of the oscillating electron lags behind the driving electric field $\boldsymbol{E}(t)$ by an angle θ. In other words, there is a time delay between the applied field and the resulting motion of the electron. Obviously, the phase difference θ is quite small when $\Omega \ll \omega_0$ $(\Omega \to 0)$, rises to $\pi/2$ for Ω close to ω_0 and further increases to π when $\Omega \gg \omega_0 (\Omega \to \infty)$. Also, for a specific value of γ, the denominator in the expression in Eq. (3) is minimum and the amplitude is maximum when $\Omega = \omega_0$. This justifies ω_0 being called the resonant frequency.

3 Dielectric Materials in the Framework of LOM

Recall that an electric dipole is an arrangement of two equal and opposite charges $(\pm Q)$ separated by a distance r. It has dipole moment $\boldsymbol{p} = Q\boldsymbol{r}$, where $\boldsymbol{r}$ and, hence, $\boldsymbol{p}$ is a vector directed from negative charge to the positive one. When an atom is subjected to an external static uniform electric field, the electron orbits (particularly those of the valence electrons) get distorted and the otherwise coincident centers of positive and negative charges (the nucleus and the electron cloud, respectively) get shifted relative to each other because these experience forces in opposite direction. These so

displaced charges create an electric dipole whose moment is aligned along the field and the atom is said to be polarized. In other words, the applied electric field induces a dipole moment in the atom. If the applied electric field is oscillatory in nature, then the separation between the centres of positive and negative charges will also be oscillatory and this will lead to an electric dipole with oscillatory moment. In the LOM, since the electron is taken as a classical particle it can be assumed to be located at the position of maximum probability of the electron cloud. Furthermore, as the nucleus has been assumed to be infinitely heavy, the applied electric field $\boldsymbol{E}(t)$ causes a shift only in the electron (which now behaves as a forced oscillator). In the present discussion, $\boldsymbol{r}(t)$ has been assumed to be directed from the stationary positive nucleus / ion core to the negatively charged electron, which is opposite to the sign convention for the electric dipole. Accordingly, the instantaneous electric dipole moment induced by the displaced electron in the associated atom (in the framework of LOM) will be given by $-\boldsymbol{p}(t) = q\boldsymbol{r}(t)$**.** Substituting for $\boldsymbol{r}(t)$ from Eq. (2) and using $\boldsymbol{E}(t)$ in place of $\boldsymbol{E_0}e^{-i\Omega t}$ there, we have

$$\boldsymbol{p}(t) = \frac{q^2}{m}\left\{\frac{(\omega_0^2-\Omega^2)+i\,\gamma\Omega}{(\omega_0^2-\Omega^2)^2+(\gamma\Omega)^2}\right\}\boldsymbol{E}(t). \qquad (4)$$

Note that $\boldsymbol{p}(t)$ is also given by $\varepsilon_0\alpha(\Omega)\boldsymbol{E}(t)$, where $\varepsilon_0 = 8.85\times10^{-12}$ F m^{-1} is electric permittivity of vacuum and $\alpha(\Omega)$ is atomic polarizability determined by the exact structure of the atom. Equating these two expressions for $\boldsymbol{p}(t)$, we get Lorentz polarizability for an atom as

$$\alpha(\Omega) = \frac{q^2}{m\varepsilon_0}\left\{\frac{(\omega_0^2-\Omega^2)+i\,\gamma\Omega}{(\omega_0^2-\Omega^2)^2+(\gamma\Omega)^2}\right\}. \qquad (5)$$

Thus, both $\boldsymbol{p}(t)$ and $\alpha(\Omega)$ are complex quantities.

If the number of such electrons per unit volume (in some material) is N , then instantaneous complex electric polarization (which is dipole moment per unit volume) of the collection will be

$$\boldsymbol{P}(t) = N\boldsymbol{p}(t) = \frac{Nq^2}{m}\left\{\frac{(\omega_0^2-\Omega^2)+i\,\gamma\Omega}{(\omega_0^2-\Omega^2)^2+(\gamma\Omega)^2}\right\}\boldsymbol{E}(t). \quad (6)$$

Here, we have assumed that response of all the electrons in the solid is identical so that all of these have the same $\boldsymbol{p}(t)$. Once again, $\boldsymbol{P}(t)$, which is macroscopic property of the substance, also depends upon Ω and is out of phase with respect to $\boldsymbol{E}(t)$ as discussed at the end of section 2. Now, polarization is related to electric susceptibility $\chi(\Omega)$ **,** sometimes referred to as first-order susceptibility, through $\boldsymbol{P}(t) = \varepsilon_0\chi(\Omega)\,\boldsymbol{E}(t)$ so that

$$\chi(\Omega) = N\alpha(\Omega) = \frac{Nq^2}{m\varepsilon_0}\left\{\frac{(\omega_0^2-\Omega^2)+i\,\gamma\Omega}{(\omega_0^2-\Omega^2)^2+(\gamma\Omega)^2}\right\}. \quad (7)$$

While writing the preceding expression for $\boldsymbol{P}(t)$, it is presumed that the material is isotropic in nature. Note that $\sqrt{Nq^2/m\varepsilon_0}$ has dimensions of angular frequency and is called plasma frequency, which is characteristic of the material. Denoting this by ω_p , we have

$$\chi(\Omega) = \omega_p^2\left\{\frac{(\omega_0^2-\Omega^2)+i\,\gamma\Omega}{(\omega_0^2-\Omega^2)^2+(\gamma\Omega)^2}\right\}, \qquad (8)$$

which too is complex.

Next, electric permittivity of a dielectric material is given by $\varepsilon = \varepsilon_0\varepsilon_r$, where $\varepsilon_r\ (= 1+\chi)$ is known as relative electric permittivity of the medium. Thus,

$$\varepsilon_r(\Omega) = 1 + \omega_p^2\left\{\frac{(\omega_0^2-\Omega^2)+i\,\gamma\Omega}{(\omega_0^2-\Omega^2)^2+(\gamma\Omega)^2}\right\}. \qquad (9)$$

Obviously, $\varepsilon_r(\Omega)$ too is a complex quantity and is also referred to as dielectric function. For $\Omega\to0$, the so-called DC limit or static value of the external electric field, Eq. (9) gives $\varepsilon_r(0) \equiv \varepsilon_r(\Omega\to0) = 1+(\frac{\omega_p}{\omega_0})^2$. Similarly, at the other extreme, when $\Omega\to\infty$, we have $\varepsilon_r(\infty) \equiv \varepsilon_r(\Omega\to\infty = 1$. Note that both ε_r0 and $\varepsilon_r\infty$ are real and independent of damping coefficient γ. Combining these two results, we get

$$\omega_p^2 = \omega_0^2\{\varepsilon_r(0) - \varepsilon_r(\infty)\}. \qquad (10)$$

Hence, Eq. (9) can also be written as

$$\varepsilon_r(\Omega) = \varepsilon_r(\infty) + \left[\frac{\omega_0^2\{\varepsilon_r(0)-\varepsilon_r(\infty)\}\{(\omega_0^2-\Omega^2)+i\,\gamma\Omega\}}{(\omega_0^2-\Omega^2)^2+(\gamma\Omega)^2}\right]. \qquad (11)$$

Now, writing $\varepsilon_r(\Omega) = \varepsilon_r'(\Omega) + i\varepsilon_r''(\Omega)$, and thus separating the real and imaginary parts in Eq. (9), we have

$$\varepsilon_r'(\Omega) = 1 + \frac{\omega_p^2(\omega_0^2-\Omega^2)}{(\omega_0^2-\Omega^2)^2+(\gamma\Omega)^2} \qquad (12)$$

and

$$\varepsilon_r''(\Omega) = \frac{\omega_p^2\gamma\Omega}{(\omega_0^2-\Omega^2)^2+(\gamma\Omega)^2}\,. \qquad (13)$$

We can also use Eq. (10) to eliminate ω_p^2 in these expressions. Note that for a particular value of other parameters, both $\varepsilon_r'(\Omega)$ and $\varepsilon_r''(\Omega)$ will decrease with increase in the value of γ. It may also be pointed out that $\varepsilon_r''(\Omega)$ vanishes when either $\Omega = 0$ or $\gamma = 0$. This implies that the imaginary part of dielectric function is intimately associated with oscillatory nature of applied electric field and damping. Thus, it is an outcome of dissipation of energy of the oscillatory external field in the medium.

It may be noted that the sign of the term added to unity in Eq. (12) will be positive or negative depending on whether Ω is smaller or larger than ω_0. Thus, this term is antisymmetric with respect to ω_0. It must be emphasized that $\varepsilon_r'(\Omega)$ will certainly be positive for $\Omega < \omega_0$, while its sign for $\Omega > \omega_0$ will be determined by the relative magnitudes of the second term and unity. On the other hand, Eq. (13) is always positive whether $\Omega < \omega_0$ or $\Omega > \omega_0$ implying that $\varepsilon_r''(\Omega)$ is symmetric about ω_0 and it will never become negative.

As a follow up of the statement made after Eq. (9), we note that $\varepsilon_r'(0) = 1 + (\frac{\omega_p}{\omega_0})^2$, $\varepsilon_r'(\infty) = 1$, and $\varepsilon_r''(0) = \varepsilon_r''(\infty) = 0$. We now look at the physical aspects of the result pertaining to the imaginary part of the dielectric function in the light of the statements made after Eq. (13). In the DC limit, all the dipoles are essentially aligned along the applied electric field (which is basically static), and these do not undergo any movement as there is no change in the field. Therefore, there is no energy loss at all and $\varepsilon_r''(0) = 0$. On the other hand, when the electric field frequency Ω is extremely large, the oscillations of the induced dipoles fail to keep pace with this because their natural frequency is quite small as compared to Ω and again there is no movement. The consequent absence of energy dissipation results in $\varepsilon_r''(\infty) = 0$.

However, if Ω has a nonzero finite value then we consider the following cases.

(i) If interaction of the oscillating electrons with their surroundings is negligible so that damping can be taken as zero for all values of Ω, then substituting $\gamma = 0$ into Eqs. (12) and (13), we get

$$\varepsilon_r'(\Omega) = 1 + \frac{\omega_p^2}{(\omega_0^2-\Omega^2)} \qquad (14)$$

and

$$\varepsilon_r''(\Omega) = 0. \qquad (15)$$

Clearly, $\varepsilon_r'(\Omega)$ will tend to $+\infty$ when Ω approaches ω_0 from below and it will be $-\infty$ for Ω approaching ω_0 from above, with a discontinuity at $\Omega = \omega_0$ (the resonance frequency). Furthermore, $\varepsilon_r''(\Omega) = 0$ implies no energy loss, which is a consequence of γ being zero.

(ii) From Eq. (12), it is clear that $\varepsilon_r'(\Omega)$ will be zero, if $\omega_p^2(\omega_0^2 - \Omega^2) = -\{(\omega_0^2 - \Omega^2)^2 + (\gamma\Omega)^2\}$. Solving this quartic equation in Ω, we find that $\varepsilon_r'(\Omega) = 0$, when $\Omega_0 = \sqrt{\frac{1}{2}\{A \pm \sqrt{B}\}}$, where $A = \omega_p^2 + 2\omega_0^2 - \gamma$ and $B = \omega_p^4 - \gamma^2(2\omega_p^2 + 4\omega_0^2 - \gamma^2)$. Since angular frequency cannot be negative, we have considered only the positive root for Ω_0. Thus, $\varepsilon_r'(\Omega)$ versus Ω plot will cross the Ω −axis twice. However, if

$\gamma > \left\{2\omega_0^2 + \omega_p^2 - 2\omega_0\sqrt{\omega_0^2 + \omega_p^2}\right\}^{1/2}$, then B becomes negative making Ω_0 a complex quantity meaning thereby that $\varepsilon_r'(\Omega)$ never becomes zero and remains positive for all values of Ω. Furthermore, for negligibly small values of γ, $A \approx \omega_p^2 + 2\omega_0^2$ and $B \approx \omega_p^4$ so that $\Omega_0 \approx \omega_0$ and $\sqrt{\omega_0^2 + \omega_p^2}$. In fact, these cross overs of $\varepsilon_r'(\Omega)$ can be used to guess values of ω_0 and ω_p for fitting the experimental data to this model.

(iii) If the applied field frequency Ω is reasonably smaller than ω_0 and γ is also such that $(\gamma\Omega)^2$ can be neglected as compared to $(\omega_0^2 - \Omega 22$, then Eqs. (12) and (13) become $\varepsilon_r'(\Omega \ll \omega_0) \approx 1 + \frac{\omega_p^2}{(\omega_0^2 - \Omega^2)}$ and $\varepsilon_r''(\Omega \ll \omega_0) \approx 0$. To look at, these are the same expressions as obtained in Eqs. (14) and (15) but here $\Omega \ll \omega_0$ (very low applied-field frequency limit). Also, γ and ε_r'' have nonzero but extremely small values.

(iv) For $\Omega = \omega_0$, $\varepsilon_r'(\omega_0) = 1$ and $\varepsilon_r''(\omega_0) = \omega_p^2/\gamma\omega_0$. Thus, the former is unity for all γ, while the latter varies inversely as γ.

(v) When the driving field frequency Ω is significantly larger than ω_0 so that $(\omega_0^2 - \Omega^2) \approx -\Omega^2$ and γ is nonzero but small enough that $(\gamma\Omega)^2 \ll (\omega_0^2 - \Omega^2)^2$, then from Eqs. (12) and (13), we have

$$\varepsilon_r'(\Omega \gg \omega_0) \approx 1 - \left(\frac{\omega_p}{\Omega}\right)^2 \qquad (16)$$

and

$$\varepsilon_r''(\Omega \gg \omega_0) \approx 0. \qquad (17)$$

Thus, for sufficiently large Ω, $\varepsilon_r' < 0$ for $\Omega < \omega_p$ and it becomes positive when $\Omega > \omega_p$.

The preceding considerations reveal that for Ω away from ω_0, $\varepsilon_r''(\Omega)$ is quite small as compared to $\varepsilon_r'(\Omega)$ and it becomes more important when the value of Ω is close to that of ω_0. Thus, the dielectric function will behave as a complex quantity (implying energy losses) mainly for applied field frequencies near the natural frequency.

Next, extrema in ε_r' as function of Ω occur when $\frac{d\varepsilon_r'(\Omega)}{d\Omega} = 0$. Simplifying the expression so obtained, we finally get the relevant physically meaningful values of Ω as $\Omega_1' = \omega_0\sqrt{1 - (\gamma/\omega_0)}$ and $\Omega_2' = \omega_0\sqrt{1 + (\gamma/\omega_0)}$ with the restriction that $\gamma < \omega_0$. Thus, in the presence of damping, $\Omega_1' < \omega_0$ and $\Omega_2' > \omega_0$. The corresponding values of $\varepsilon_r'(\Omega)$ are found to be

$$\varepsilon_r'(\Omega_1') = 1 + \frac{\omega_p^2}{\gamma(2\omega_0 - \gamma)} \qquad (18)$$

and

$$\varepsilon_r'(\Omega_2') = 1 - \frac{\omega_p^2}{\gamma(2\omega_0 + \gamma)}. \qquad (19)$$

Obviously, the former is local maximum (peak) while the latter is local minimum (dip). Also, since $\gamma < \omega_0$, $\varepsilon_r'(\Omega_1')$ will always be positive irrespective of the value of γ. On the other hand, $\varepsilon_r'(\Omega_2')$ will be negative if $\frac{\omega_p^2}{\gamma(2\omega_0 + \gamma)} > 1$, which is so if $\gamma < \omega_0\left(\sqrt{1 + \left(\frac{\omega_p}{\omega_0}\right)^2} - 1\right)$. For higher values of γ, $\varepsilon_r'(\Omega_2')$ will be positive.

To make the above-mentioned aspects visually clear, we have plotted $\varepsilon_r'(\Omega)$ vs Ω for Eq. (12) in Figs. 1 and 2. Note that the parameters ω_0, ω_p, and γ appearing in this equation have units rad s^{-1} and their magnitudes are $\sim 10^{15}$ or so. However, we shall express these in energy units, eV, by multiplying with $\hbar = 6.58 \times 10^{-16}$ eV s^{-1}. Thus, strictly speaking ω_0, ω_p, and γ as used hereafter are $\hbar\omega_0$, $\hbar\omega_p$, and $\hbar\gamma$, respectively. Accordingly, Ω too is taken in eV and refers to photon energy. It may be mentioned that Ω lies between 1.65 and 3.26 eV for the visible region.

Guided by the fact that for a good number of dielectric materials ω_p and ω_0 lie between 10 and 15 eV, and between 8 and 13 eV, respectively, we have taken $\omega_p = 13.5$ eV and $\omega_0 = 10$ eV. In fact, these are the values we have later used for fitting the experimental data for silica in Section 5. Note

that both the chosen values are in the extreme ultraviolet region. The γ values used in Fig. 1 are 0, 0.05 and 0.2 eV while these are 1.0, 4.0 and 7.0 eV for Fig. 2. In Fig.1, the Ω values have been taken from 9 eV to 11 eV and $\varepsilon_r'(\Omega)$ values from -300 to 300 rather than the actual values obtained, to make the plots for non-zero γ to be clearly noticeable. Consequently, the Ω values higher than ω_0 , for which $\varepsilon_r'(\Omega)$ undergoes change from negative values to positive ones are not visible. In all the cases depicted in Fig. 1, $\varepsilon_r'(\Omega)$ changes sign at $\Omega \approx 16.8$ eV, which is

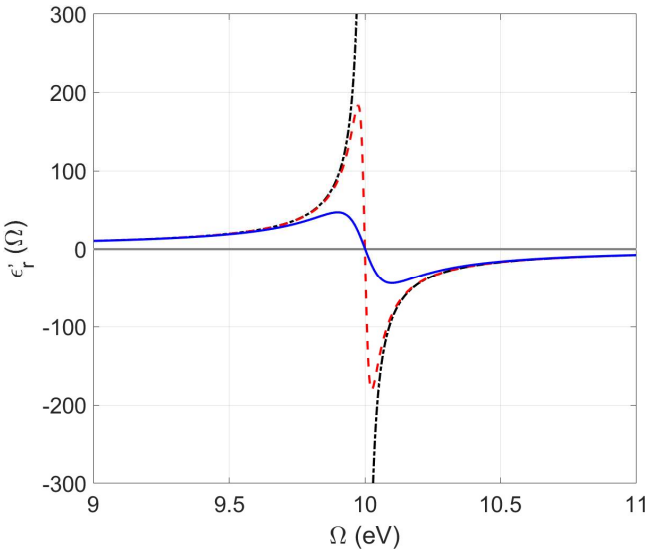

Fig. 1. Plots showing angular frequency dependence of $\varepsilon_r'(\Omega)$ for $\omega_p = 13.5$ eV, $\omega_0 = 10$ eV, and $\gamma = 0$ (black dash-dot line), $\gamma = 0.05$ eV (red dashed line), and $\gamma = 0.2$ eV (blue solid line).

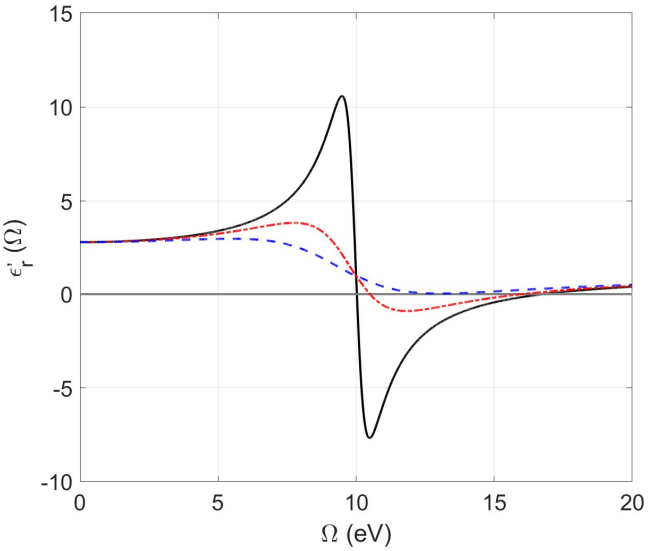

Fig. 2. $\varepsilon_r'(\Omega)$ vs Ω plots for $\omega_p = 13.5\,eV$, $\omega_0 = 10\,eV$, and $\gamma = 1.0$ eV (black solid line), $\gamma = 4.0$ eV (red dash-dot line), and $\gamma = 7.0$ eV (blue dash-dash line).

consistent with the value determined from $\Omega_0 = \sqrt{\omega_0^2 + \omega_p^2}$ found earlier. As far as higher values of γ are concerned, in Fig. 2 the crossover occurs at $\Omega_0 = 16.61$ eV for $\gamma = 1.0$ eV, and at $\Omega_0 = 16.0$ eV for $\gamma = 4.0$ eV. However, sign does not change for $\gamma = 7.0$ eV.

Coming to the expression for $\varepsilon_r''(\Omega)$, Eq. (13), the condition for occurrence of extrema in ε_r'', which is always positive, as function of Ω leads to local maximum (peak) at

$$\Omega'' = \left[\frac{2\omega_0^2 - \gamma^2}{6}\left\{1 + \sqrt{1 + \frac{12\omega_0^4}{(2\omega_0^2 - \gamma^2)^2}}\right\}\right]^{1/2}. \quad (20)$$

For very small value of γ ($\ll \omega_0$), Ω'' is quite close to ω_0 and decreases slightly with increase in γ; in fact, Ω''= 0.97 ω_0 when $\gamma = 0.5\ \omega_0$.

The above consideration shows that the peak in $\varepsilon_r''(\Omega)$ essentially occurs for Ω reasonably near ω_0. Now, for $\Omega \approx \omega_0$, $\omega_0^2 - \Omega^2 = (\omega_0 + \Omega)(\omega_0 - \Omega) \approx 2\omega_0(\omega_0 - \Omega)$. Accordingly, Eq. (13) for $\varepsilon_r''(\Omega)$ can be written as

$$\varepsilon_r''(\Omega \approx \omega_0) \approx \frac{\omega_p^2}{2\omega_0}\left\{\frac{\frac{\gamma}{2}}{(\omega_0-\Omega)^2+\left(\frac{\gamma}{2}\right)^2}\right\}. \qquad (21)$$

Here, the expression in $\{...\}$ is π times the Lorentzian function with peak at $\Omega = \omega_0$ and γ as full width at half maximum. Therefore, $\varepsilon_r''(\Omega)$ vs Ω plot (which is clearly symmetric with respect to ω_0) is usually said to have Lorentzian shape. It is clear from Eq. (21) that the location of the peak in the $\varepsilon_r''(\Omega)$ graph is given by ω_0 and the peak height is determined by $\omega_p^2/\omega_0\gamma$. Since $\varepsilon_r''(\Omega)$ represents dissipation of energy of the oscillatory field, its peak position ω_0 is sometimes called the absorption angular frequency. Also, the range of Ω values for which magnitude of $\varepsilon_r''(\Omega)$ is large is referred to as region of resonant absorption. In contrast, if we substitute the preceding expression for $\omega_0^2 - \Omega^2$ into Eq. (12), we get

$$\varepsilon_r'(\Omega) \approx 1 + \frac{\omega_p^2}{2\omega_0}\frac{(\omega_0-\Omega)}{(\omega_0-\Omega)^2+(\gamma/2)^2}. \qquad (22)$$

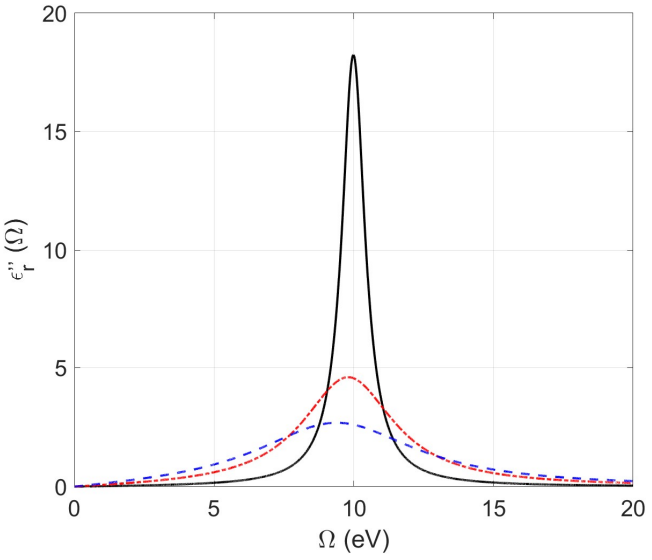

Fig. 3. Variation of $\varepsilon_r''(\Omega)$ with Ω for the parameters and legends as used in Fig. 2.

This too brings out the fact that the second term in this expression is an odd function of $(\omega_0 - \Omega)$ and, hence, antisymmetric about ω_0.

The variation of $\varepsilon_r''(\Omega)$ with the applied field frequency Ω has been projected in Fig. 3, for the parameters used in Fig. 2 and it corroborates the observations made above. It is pertinent to note that the plots are peaked nearly around $\Omega = \omega_0$ with little shift towards lower Ω values as γ increases. Thus, energy absorption is maximum for Ω close to ω_0. Also, from Figs. 1- 3, we note that an increase in damping makes the peaks in $\varepsilon_r'(\Omega)$ and $\varepsilon_r''(\Omega)$ vs Ω plots shorter and broader. This is in consonance with the fact that the value of γ provides a measure of the width of these peaks.

Having dwelt upon various aspects of $\varepsilon_r(\Omega)$, we come to some optical properties of the material. Recall that if the phase velocity of an e.m. wave in a medium is v_{ph}, then its refractive index is given by $n = c/v_{ph} = \sqrt{\varepsilon\mu/\varepsilon_0\mu_0} = \sqrt{\varepsilon_r\mu_r}$, where $\mu\ (= \mu_0\mu_r)$ is magnetic permeability of the substance and μ_r is its relative permeability. For the paramagnetic and diamagnetic substances (the so-called non-magnetic materials), μ_r differs from unity by about $10^{-4} - 10^{-6}$ so that for these, we can take $n(\Omega) = \sqrt{\varepsilon_r(\Omega)}$. Thus, the index of refraction of such a substance is a complex quantity, given by

$$n(\Omega) = \left[1 + \omega_p^2\left\{\frac{(\omega_0^2-\Omega^2)+i\,\gamma\Omega}{(\omega_0^2-\Omega^2)^2+(\gamma\Omega)^2}\right\}\right]^{1/2}. \qquad (23)$$

Writing $n(\Omega) = n'(\Omega) + in''(\Omega)$ and using the fact that $n^2(\Omega) = \varepsilon_r(\Omega) = \varepsilon_r'(\Omega) + i\varepsilon_r''(\Omega)$, we get $\varepsilon_r'(\Omega) = \{n'(\Omega)\}^2 - \{n''(\Omega)\}^2$ and $\varepsilon_r''(\Omega) = 2n'(\Omega)n''(\Omega)$. Eliminating $n''(\Omega)$ from these two equations, and solving the resulting quadratic equation in $\{n'(\Omega)\}^2$, we finally get

$$n'(\Omega) = \left\{\frac{\sqrt{\{\varepsilon_r'(\Omega)\}^2+\{\varepsilon_r''(\Omega)\}^2} + \varepsilon_r'(\Omega)}{2}\right\}^{1/2}. \qquad (24)$$

Similarly, elimination of $n'(\Omega)$ from the preceding two equations yields

$$n''(\Omega) = \left\{\frac{\sqrt{\{\varepsilon_r'(\Omega)\}^2+\{\varepsilon_r''(\Omega)\}^2} - \varepsilon_r'(\Omega)}{2}\right\}^{1/2} . \quad (25)$$

These equations give exact relations for the real and imaginary parts of refractive index in terms of the real and imaginary parts of dielectric function. From Eq. (25), we find that $n''(\Omega)$ is zero or nonzero depending on whether $\varepsilon_r''(\Omega)$ is zero or not. Since $\Omega \neq 0$ for e.m. waves, in view of remarks made in the paragraph after Eq. (13), we infer that imaginary part of the refractive index too has its origin in nonzero value of γ. Hence, it pertains to dissipation or absorption of energy of the e.m. radiation passing through the material. Thus, $n''(\Omega)$ is responsible for the attenuation of the incident beam. The real part $n'(\Omega)$ is the conventional refractive index we come across while discussing transmission of light through a medium. The dependence of refractive index on the frequency of light indicates dispersion.

It may be pointed out that for $\gamma = 0$, $\varepsilon_r'(\Omega)$ and $\varepsilon_r''(\Omega)$ are given by Eqs. (14) and (15), respectively, so that Eqs. (24) and (25) yield

$$n'(\Omega) = \sqrt{\varepsilon_r'(\Omega)} = \left\{1 + \frac{\omega_p^2}{(\omega_0^2-\Omega^2)}\right\}^{1/2}, \quad (26)$$

and $n''(\Omega) = 0$. Thus, e.m. radiation passes through such an ideal medium without any absorption or attenuation.

However, if γ is nonzero but very small and $\Omega \ll$
ω_0, then, since $\varepsilon_r''(\Omega \ll \omega_0) \approx 0$, we get from Eqs. (24) and (25), $n''(\Omega \ll \omega_0) \approx 0$ and $n'(\Omega \ll$ *ω0 ≈εr′Ω≪ω0 =1+ωp2ω02−Ω21/2.* But for $\Omega \ll \omega_0$, $\frac{1}{(\omega_0^2-\Omega^2)} = \frac{1}{\omega_0^2}\left\{1 - \frac{\Omega^2}{\omega_0^2}\right\}^{-1} \approx \frac{1}{\omega_0^2}\left\{1 + \frac{\Omega^2}{\omega_0^2}\right\}$ so that

$$n'(\Omega \ll \omega_0) \approx \left[1 + \frac{\omega_p^2}{\omega_0^2}\left\{1 + \frac{\Omega^2}{\omega_0^2}\right\}\right]^{1/2}. \quad (27)$$

Furthermore, for nonzero but very small γ and $\Omega \gg \omega_0$, which practically is the case for X-ray frequencies, we have on substituting Eqs. (16) and (17) into Eqs. (24) and (25),

$$n'(\Omega \gg \omega_0) \approx \sqrt{\varepsilon_r'(\Omega \gg \omega_0)} = \sqrt{1 - \left(\frac{\omega_p}{\Omega}\right)^2}, \quad (28)$$

and $n''(\Omega \gg \omega_0) \approx 0$. Thus, $n(\Omega \gg \omega_0) \approx n'(\Omega \gg \omega_0)$. Note that, for $\omega_0 \ll \Omega < \omega_p$, $n(\Omega)$ is imaginary implying that in the X-ray region, the dielectric substances having small ω_0 values completely absorb radiation if $\Omega < \omega_p$. However, for $\Omega > \omega_p$, the refractive index is real but less than unity, which corresponds to the situation that phase velocity of the e.m. wave in the material is higher than the speed of light in vacuum. Furthermore, it approaches unity when $\Omega \gg \omega_p$.

The dependence of $n'(\Omega)$ and $n''(\Omega)$ on Ω for the parameters mentioned in the caption for Fig. 2 has been illustrated graphically in Figs. 4 and 5, respectively. A look at these plots shows that $n'(\Omega)$ has peak close to ω_0 and it attains minimum value near $\Omega \approx \omega_p$ and then increases again. The relevant magnitudes depend on γ and the width of the flat part of the minimum decreases as γ increases. On

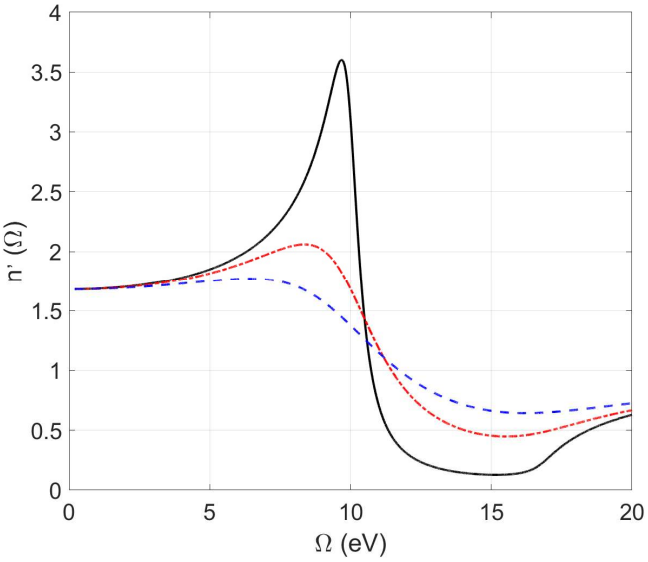

Fig. 4. Spectral dependence of $n'(\Omega)$ for the parameters and legends as described in Fig. 2.

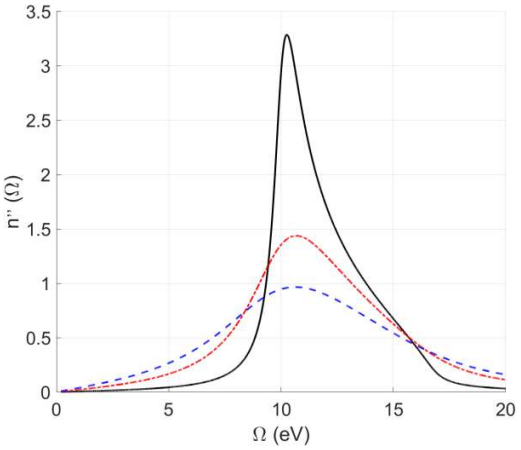

Fig. 5. Dependence of $n''(\Omega)$ on Ω for the parameters and legends as listed in Fig. 2.

the other hand, $n''(\Omega)$ are maximum for Ω lying between ω_0 and ω_p and tend to zero for higher values of Ω. It may be mentioned that the rise in $n'(\Omega)$ values with increase in Ω (i.e., decrease in incident wavelength of e.m. radiation) is known as normal dispersion because this is in accord with what we observe when white light passes through a prism. In contrast the sharp fall in $n'(\Omega)$ with increase in Ω is called anomalous dispersion. It is pertinent to note that anomalous dispersion occurs over the range of Ω values for which $n''(\Omega)$ has its peak (Fig. 5), i.e., the medium is highly absorbing. Consequently, experimental observation of anomalous dispersion is not that easy.

The fact that both $n'(\Omega)$ and $n''(\Omega)$ are quite close to zero for small values of γ and $\Omega \geq \omega_p$ (see Figs. 4 and 5 and Eq. (28)) needs special consideration. As mentioned earlier also, refractive index is obtained by dividing speed of light in vacuum with the phase velocity $v_{ph} = \lambda\,\Omega/2\pi$, where λ is wavelength of the relevant e.m. wave in the medium. Therefore, $n(\Omega) \approx 0$ implies that v_{ph} and, hence, λ are infinitely large. The wavelength being infinite means that all the electrons in the solid are oscillating in phase.

Another physically observable optical quantity of interest is the normal incidence reflection coefficient, reflectivity, or reflectance of the medium. It gives the fraction of the power associated with the incident e.m. wave reflected from the surface of the material. For the air-solid boundary, it is defined as [3,5]

$$R(\Omega) = \left|\frac{n(\Omega)-1}{n(\Omega)+1}\right|^2 = \frac{\{n'(\Omega)-1\}^2+\{n''(\Omega)\}^2}{\{n'(\Omega)+1\}^2+\{n''(\Omega)\}^2}\,. \qquad (29)$$

As a special case, note that for $\Omega \ll \omega_0$ as well as for $\Omega \gg \omega_0$,

$$R(\Omega) \approx \frac{\{n'(\Omega)-1\}^2}{\{n'(\Omega)+1\}^2}\,. \qquad (30)$$

With a view to bring out the dependence of $R(\Omega)$ on various parameters, we have shown $R(\Omega)$ as function of Ω in Fig. 6, for $\omega_p = 13.5$ eV, $\omega_0 = 10$ eV, and $\gamma = 0,\ 0.2,\ 1.0,\ 4.0,$ and 7.0 eV. A perusal of this figure reveals that the damping rounds out the corners of the plots and that an increase in γ decreases the maximum value of reflectance, which is unity or 100% for $\gamma = 0$. Also, for a particular value of γ, $R(\Omega)$ is maximum when

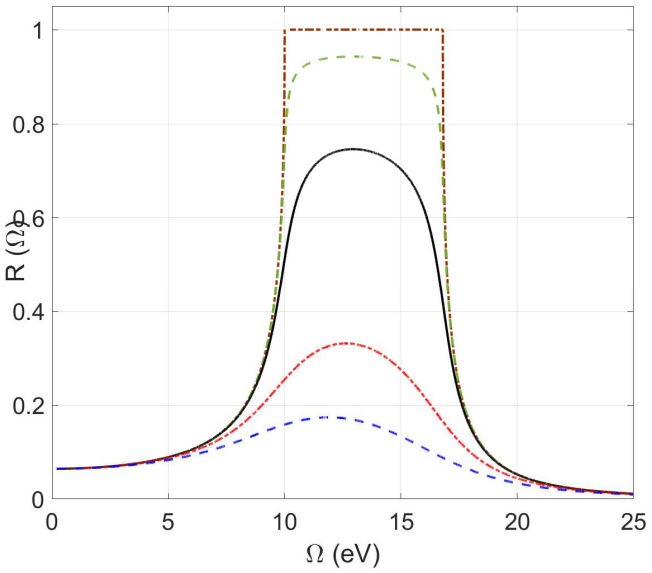

Fig. 6. Reflectivity $R(\Omega)$ vs Ω plots for $\omega_p = 13.5$ eV, $\omega_0 = 10$ eV, and $\gamma = 0.0$ (dark brown

dash-dot line), $\gamma = 0.2$ eV (green dash-dash line) $\gamma = 1.0$ eV (black solid line), $\gamma = 4.0$ eV (red dash-dot line), and $\gamma = 7.0$ eV (blue dash-dash line).

$n'(\Omega)$ is minimum. This is understandable because for $n'(\Omega) \to 0$, Eq. (29) gives $R(\Omega) \to 1$, which is its maximum possible value.

From a perusal of the plots in Figs. 4 – 6 and the discussion of the expressions for $n'(\Omega)$, $n''(\Omega)$, and $R(\Omega)$, it can be inferred that for Ω reasonably smaller than ω_0 and significantly higher than ω_p, the dielectric materials are transparent to the incident e.m. waves. However, for Ω close to ω_0, these show maximum absorption while they are strongly reflective when Ω values lie between ω_0 and ω_p and are even somewhat higher than the latter. In order to make this conclusion clearer, we have shown in Fig. 7, dependence of $n'(\Omega)$, $n''(\Omega)$, and $R(\Omega)$ on Ω for an oscillator system with parameter values $\omega_p = 12$ eV, $\omega_0 = 2.5$ eV, and $\gamma = 1$ eV as a typical representative; here ω_0 is in the visible region and quite less than ω_p, which is at variance with the case depicted in Figs. 4 – 6.

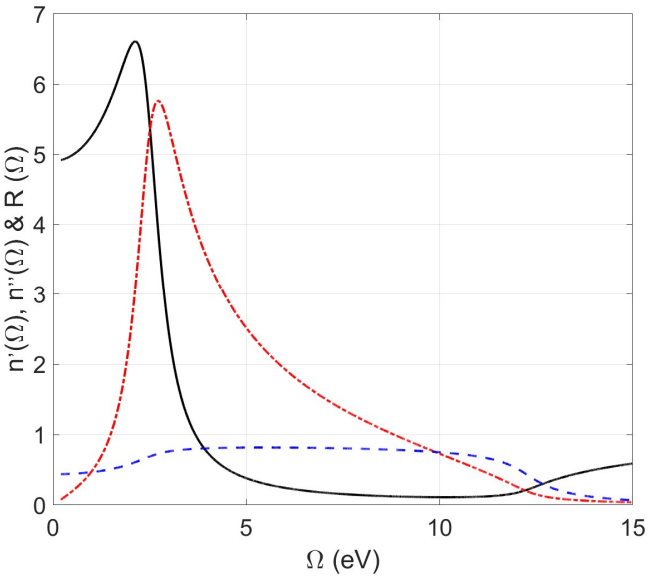

Fig. 7. $n'(\Omega)$ (black solid line), $n''(\Omega)$ (red dash-dot line), and $R(\Omega)$ (blue dash-dash line), as functions of Ω for an oscillator with parameter values $\omega_p = 12$ eV, $\omega_0 = 2.5$ eV, and $\gamma = 1$ eV.

So far, we have assumed that all the Lorentz oscillators in a collection are completely identical. However, a substance can have Lorentz oscillators of different types because the electrons experience different binding and damping forces or the atoms / ion cores with which the electrons are associated have different nature. Suppose that N_j of these in unit volume are of one type represented by subscript j. Denoting their natural angular frequency, and damping coefficient by $\omega_{0,j}$ and γ_j, respectively, the electric susceptibility of this group of Lorentz oscillators will be given by

$$\chi_j(\Omega) = \frac{N_j q^2}{m\varepsilon_0}\left\{\frac{\left(\omega_{0,j}^2-\Omega^2\right)+i\,\gamma_j\Omega}{\left(\omega_{0,j}^2-\Omega^2\right)^2+\left(\gamma_j\Omega\right)^2}\right\}; \quad (31)$$

(see, Eq. (7)). Representing the plasma frequency of this category by $\omega_{p,j}$, we have $\omega_{p,j}^2 = N_j q^2/m\varepsilon_0$ so that

$$\chi_j(\Omega) = \omega_{p,j}^2\left\{\frac{\left(\omega_{0,j}^2-\Omega^2\right)+i\,\gamma_j\Omega}{\left(\omega_{0,j}^2-\Omega^2\right)^2+\left(\gamma_j\Omega\right)^2}\right\}. \quad (32)$$

Also, total electric susceptibility of the system comprising different types of oscillators such that $N = \sum_j N_j$ will be given by $\chi(\Omega) = \sum_j \chi_j(\Omega)$.

Taking the fraction of Lorentz oscillators of type j to be $f_j = N_j/N$, we have $\omega_{p,j}^2 = f_j\omega_p^2$. Accordingly, the relative electric permittivity of this system will be given by

$$\begin{aligned}\varepsilon_r(\Omega) &= 1 + \textstyle\sum_j \chi_j(\Omega)\\ &= 1 + \omega_p^2 \textstyle\sum_j f_j\left\{\frac{\left(\omega_{0,j}^2-\Omega^2\right)+i\,\gamma_j\Omega}{\left(\omega_{0,j}^2-\Omega^2\right)^2+\left(\gamma_j\Omega\right)^2}\right\} \quad (33)\end{aligned}$$

It may be mentioned that f_j is usually referred to as oscillator strength. Also, a quantum mechanical treatment of the problem leads to an expression which looks like Eq. (33) but has different

meaning of $\omega_{0,j}$ as well as f_j . The real and imaginary parts of Eq. (33) are

$$\varepsilon_r'(\Omega) = 1 + \omega_p^2 \sum_j \frac{f_j\left(\omega_{0,j}^2 - \Omega^2\right)}{\left(\omega_{0,j}^2 - \Omega^2\right)^2 + \left(\gamma_j \Omega\right)^2} \qquad (34)$$

and

$$\varepsilon_r''(\Omega) = \omega_p^2 \sum_j \left\{ \frac{f_j \gamma_j \Omega}{\left(\omega_{0,j}^2 - \Omega^2\right)^2 + \left(\gamma_j \Omega\right)^2} \right\}, \qquad (35)$$

respectively. These have been depicted in Fig. 8 for a system comprising two types of oscillators with $\omega_p = 13.5$ eV , $\omega_{0,1} = 10$ eV, $\omega_{0,2} = 12$ eV, $\gamma_1 = \gamma_2 = 1.0$ eV, and $f_1 = f_2 = 0.50$.

While using Eq. (34) for real systems, sometimes the factor 1 on the right-hand side has to be replaced by a greater number corresponding to the value of $\varepsilon_r'(\infty)$ to take care of the contribution of oscillators with higher $\omega_{0,j}$ which are not covered in the summation.

The expression for complex index of refraction is now modified to read

$$n(\Omega) = \left[1 + \omega_p^2 \sum_j f_j \left\{ \frac{\left(\omega_{0,j}^2 - \Omega^2\right) + i\,\gamma_j \Omega}{\left(\omega_{0,j}^2 - \Omega^2\right)^2 + \left(\gamma_j \Omega\right)^2} \right\} \right]^{1/2} \qquad (36)$$

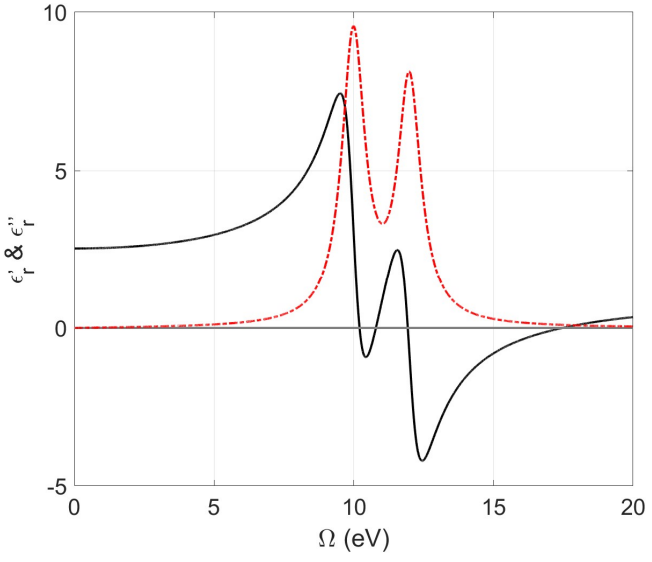

Fig. 8. Spectral dependence of $\varepsilon_r'(\Omega)$ (black solid line) and $\varepsilon_r''(\Omega)$ (red dash-dot line) for a two-oscillator system with $\omega_p = 13.5$ eV, $\omega_{0,1} = 10$ eV, $\omega_{0,2} = 12$ eV, $\gamma_1 = \gamma_2 = 1.0$ eV, and $f_1 = f_2 = 0.5$.

Similarly, Eqs. (24), (25), and (29) for $n'(\Omega)$, $n''(\Omega)$, and $R(\Omega)$, respectively, too are recast for a many-oscillator system. Fig. 9 depicts dependence of these three quantities on Ω for the two-oscillator system considered in Fig. 8.

4 Drude Model for Conducting Substances as an Extension of LOM

According to the DM for a metal the positively charged ion cores are fixed like those in the LOM, but the negatively charged electrons wander around like gas molecules without any constraint of being attached to a particular nucleus or ion core. As such, there is no restoring force acting on an electron and, thus, $\omega_0 = 0$. Furthermore, since an electron is not
hooked up to a specific core, we preferably describe its motion in terms of its instantaneous velocity $\boldsymbol{v}(t)$. However, an electron in the conducting material does experience damping mainly due to its scattering caused by the interaction with the stationary cores, impurities, and crystal imperfections present and with other electrons.

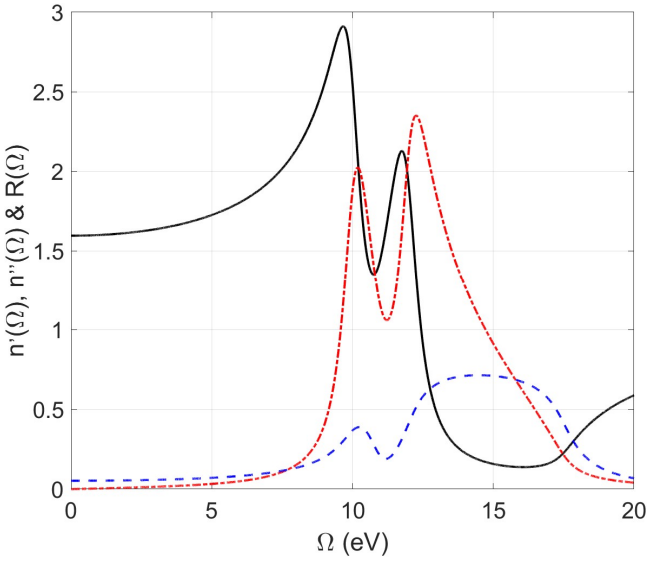

Fig. 9. Plots displaying $n'(\Omega)$ (black solid line), $n''(\Omega)$ (red dash-dot line), and $R(\Omega)$ (blue dash-dash line), as function of Ω for the two-oscillator system having parameter values mentioned in the caption of Fig. 8.

Therefore, the differential equation governing the motion of such an electron under the influence of an applied harmonic electric field $\boldsymbol{E}(t) = \boldsymbol{E_0}e^{-i\Omega t}$, can be written as

$$\dot{\boldsymbol{v}}(t) + \gamma \boldsymbol{v}(t) = -\frac{q}{m}\boldsymbol{E_0}e^{-i\Omega t}. \qquad (37)$$

The homogeneous solution of this first-order nonhomogeneous linear differential equation contains $e^{-\gamma t}$, which becomes zero for large values of t. As in the case of LOM, this too represents transients. Finally, in this case also we are left with the nonhomogeneous solution, the so-called steady state solution, which reads

$$\boldsymbol{v}(t) = -\frac{q}{m}\frac{1}{\gamma - i\Omega}\boldsymbol{E_0}e^{-i\Omega t} = -\frac{q}{m}\frac{\gamma + i\Omega}{\gamma^2+\Omega^2}\boldsymbol{E_0}e^{-i\Omega t}. \qquad (38)$$

Proceeding as has been done in going from Eq. (2) to Eq. (3), it can be shown that $\boldsymbol{v}(t)$, which also oscillates with angular frequency Ω, is out of phase with respect to the external electric field $\boldsymbol{E}(t)$ by an angle $\varphi = tan^{-1}(\Omega/\gamma)$. Obviously, φ increases from 0 to $\pi/2$ as Ω is varied from 0 to extremely large value. In fact, for DC electric field $\boldsymbol{E_0}$ ($\Omega = 0$), velocity is constant and from Eq. (38), it can be written as $\mathbf{v}(\Omega = 0) = -\frac{q\boldsymbol{E_0}}{m\gamma}$. This is called the drift velocity of electrons.

The electric current density produced by all the free electrons with number density N is given by

$$\boldsymbol{J}(t) = -Nq\mathbf{v}(t) = \frac{Nq^2}{m}\frac{\gamma + i\Omega}{\gamma^2+\Omega^2}\mathbf{E}(t). \qquad (39)$$

Since the current density is also given by $\boldsymbol{J}(t) = \sigma(\Omega)\mathbf{E}(t)$, where $\sigma(\Omega)$ is dynamic electrical conductivity of the material, we have

$$\sigma(\Omega) = \frac{Nq^2}{m}\frac{\gamma + i\Omega}{\gamma^2+\Omega^2} = \varepsilon_0\omega_p^2\frac{\gamma + i\Omega}{\gamma^2+\Omega^2}. \qquad (40)$$

This is usually called Drude conductivity and is, obviously, frequency-dependent complex quantity. Here too the solid is taken to be isotropic.

If the applied electric field is constant $\boldsymbol{E_0}$ ($\Omega = 0$), then steady or DC electric current density and corresponding electric conductivity are, respectively, given by $\boldsymbol{J}(\Omega = 0) = \frac{Nq^2}{m\gamma}\boldsymbol{E_0}$ and $\sigma(\Omega = 0) = \frac{Nq^2}{m\gamma}$. Note that this is nothing but Ohm's law with resistivity $\rho = m\gamma/Nq^2$. It may also be pointed out that in this model, all the free electrons contribute to $\boldsymbol{J}$. However, this is in violation of their quantum description, according to which under the influence of applied electric field only a small fraction of electrons in the occupied states below the Fermi level acquire sufficient energy to get excited to the empty energy levels above this to participate in electrical conduction.

Furthermore, the dielectric function $\varepsilon_r(\Omega)$ is related to electrical conductivity $\sigma(\Omega)$ through $\varepsilon_r = 1 + i\frac{\sigma(\Omega)}{\varepsilon_0\Omega}$ so that the Drude complex dielectric function for a conducting material is given by

$$\varepsilon_{r,D}(\Omega) = 1 - \frac{\omega_p^2}{\Omega}\left(\frac{\Omega - i\gamma}{\Omega^2+\gamma^2}\right). \qquad (41)$$

This is the same result as we obtain by putting $\omega_0 = 0$ in Eq. (9) for $\varepsilon_r(\Omega)$ in LOM implying that the DM can be considered as a special case of the Lorentz model. The real and imaginary parts of $\varepsilon_{r,D}(\Omega)$ are

$$\varepsilon'_{r,D}(\Omega) = 1 - \frac{\omega_p^2}{\Omega^2+\gamma^2} \text{ and } \varepsilon''_{r,D}(\Omega) = \frac{\gamma}{\Omega}\frac{\omega_p^2}{\Omega^2+\gamma^2}, \qquad (42)$$

respectively. Note that like $\varepsilon''_r(\Omega)$, $\varepsilon''_{r,D}(\Omega) = 0$ when $\gamma = 0$, meaning thereby that $\varepsilon''_{r,D}(\Omega)$ too is related to damping and, hence, to absorption of energy associated with the applied electric field.

Next, the refractive index of a conducting nonmagnetic material will be given by

$$n_D(\Omega) = \sqrt{\varepsilon_{r,D}(\Omega)} = \left\{1 - \frac{\omega_p^2}{\Omega}\left(\frac{\Omega - i\gamma}{\Omega^2+\gamma^2}\right)\right\}^{\frac{1}{2}}, \quad (43)$$

with relevant expression for the real and imaginary parts $n'_D(\Omega)$ and $n''_D(\Omega)$. Also, Eqs. (24), (25), and (29) too hold good for $n'_D(\Omega)$, $n''_D(\Omega)$, and normal incidence reflectance $R_D(\Omega)$ with appropriate replacement of $\varepsilon'_r(\Omega)$, $\varepsilon''_r(\Omega)$, $n'(\Omega)$, and $n''(\Omega)$.

It may be mentioned that in the case of conducting materials, generally, γ is quite small as compared to ω_p. Now, we consider the following five situations.

(i) For the ideal case $\gamma = 0$, Eqs. (42) and (43) yield

$$\varepsilon'_{r,D}(\Omega) = 1 - \left(\frac{\omega_p}{\Omega}\right)^2, \ \varepsilon''_{r,D}(\Omega) = 0; \quad (44)$$

$$n'_D(\Omega) = \left\{1 - \left(\frac{\omega_p}{\Omega}\right)^2\right\}^{\frac{1}{2}}, \text{ and } n''_D(\Omega) = 0. \quad (45)$$

As expected, the expressions for $\varepsilon'_{r,D}(\Omega)$ and $n'_D(\Omega)$ are special cases of relevant expression in Eqs. (14) and (26) with $\omega_0 = 0$. Note that $\varepsilon'_{r,D}(\Omega)$ is negative for $\Omega < \omega_p$ having quite large magnitude for low values of Ω. It becomes zero when $\Omega = \omega_p$ and increases with increase in Ω value, becoming unity when $\Omega \gg \omega_p$. Furthermore, $n'_D(\Omega)$ and, hence, $n_D(\Omega)$ is imaginary when $\Omega < \omega_p$ implying that the ideal metal is completely opaque to the relevant e.m. radiation. It is less than unity for $\Omega > \omega_p$, and for Ω much larger than ω_p, we can write $n'_D \approx 1 - \frac{1}{2}\left(\frac{\omega_p}{\Omega}\right)^2$.

(ii) For nonzero γ, $\varepsilon''_{r,D}(\Omega)$ is always positive, but $\varepsilon'_{r,D}(\Omega)$ will be negative if $\Omega < \sqrt{\omega_p^2 - \gamma^2}$ and positive for $\Omega > \sqrt{\omega_p^2 - \gamma^2}$. Combined with Eqs. (22) and (23) these imply that $n''_D(\Omega) > n'_D(\Omega)$ for $\Omega < \sqrt{\omega_p^2 - \gamma^2}$ and reverse will be true when $\Omega > \sqrt{\omega_p^2 - \gamma^2}$.

(iii) When Ω is quite small as compared to ω_p and comparable with γ so that $\omega_p^2 \gg \Omega^2 + \gamma^2$, then from Eq. (42) we see that $\varepsilon'_{r,D}(\Omega \ll \omega_p)$ will be negative with quite large magnitude while $\varepsilon''_{r,D}(\Omega \ll \omega_p)$ will be positive and reasonably large depending on the value of γ/Ω. Consequently, $n''_D(\Omega \ll \omega_p)$ will be much larger than $n'_D(\Omega \ll \omega_p)$. Furthermore, dominance of $n''_D(\Omega)$ in the expression for $R(\Omega)$ (Eq. (29)), indicates that $R_D(\Omega \ll \omega_p)$ will be reasonably close to unity. Physically, these features imply that at quite low frequencies ($\Omega \ll \omega_p$), the electric field cannot penetrate the metal and that most of the e.m. radiation will be reflected by it.

(iv) If $\Omega = \omega_p$ implying that $\frac{\omega_p^2}{\gamma^2+\Omega^2} \approx 1$ (assuming that γ is quite small) then $\varepsilon'_{r,D}(\omega_p) \approx 0$ and $\varepsilon''_{r,D}(\omega_p) = \frac{\gamma}{\omega_p} \ll 1$. Thus, both $\varepsilon_{r,D}(\omega_p)$ and $n_D(\omega_p) \approx 0$. However, if γ is not very small then $\varepsilon'_{r,D}(\omega_p)$, $\varepsilon''_{r,D}(\omega_p)$, $n'_D(\omega_p)$ and $n''_D(\omega_p)$ are nonzero and their magnitudes will depend on the value of γ. Furthermore, since $n'_D(\omega_p)$ and $n''_D(\omega_p)$ are nonzero though reasonably small $R_D(\omega_p)$ will still be high and will depend upon the value of γ.

(v) For $\Omega > \omega_p$, $\gamma \ll \Omega$ and $\Omega^2 + \gamma^2 \approx \Omega^2$. Therefore, $\varepsilon'_{r,D}(\Omega > \omega_p) = 1 - \left(\frac{\omega_p}{\Omega}\right)^2 > 0$ and $\varepsilon''_{r,D}(\Omega > \omega_p) \approx 0$. In this case, from Eqs. (24) and (25), we have

$$n'_D(\Omega > \omega_p) \approx \sqrt{\varepsilon'_{r,D}(\Omega > \omega_p)} = \left\{1 - \left(\frac{\omega_p}{\Omega}\right)^2\right\}^{1/2}$$

and $n''_D \approx 0$ so that $R_D(\Omega > \omega_p) \approx \{n'_D(\Omega) - 1\}^2/\{n'_D(\Omega) + 1\}^2$. Thus, $n'_D(\Omega)$ and,

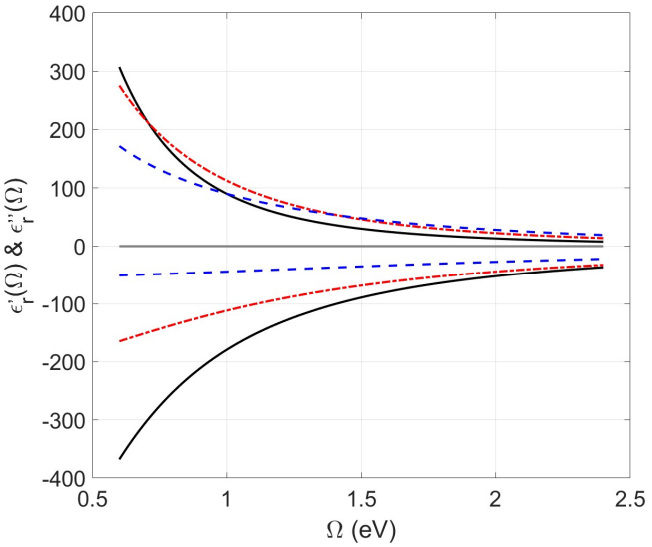

Fig. 10. Plots for $\varepsilon'_{r,D}(\Omega)$ (below the zero line) and $\varepsilon''_{r,D}(\Omega)$ (above the zero line) as function of Ω for a conducting material with $\omega_p = 15$ eV and $\gamma = 0.5$ eV (black solid line), $\gamma = 1.0$ eV (red dash-dot line), and $\gamma = 2.0$ eV (blue dash-dash line). Note that both the axes have been highly truncated.

hence, $n_D(\Omega)$ become nonzero when Ω exceeds ω_p, and attain maximum value 1 for $\Omega \gg \omega_p$. Obviously, $R_D(\Omega \gg \omega_p)$ will be zero. In other words, at very high frequencies, the free electron contribution is unimportant.

To bring out various aspects discussed above, we have plotted $\varepsilon'_{r,D}(\Omega)$ and $\varepsilon''_{r,D}(\Omega)$ as function of Ω for a metal characterized by $\omega_p = 15\ eV$ and $\gamma = 0.5, 1.0,$ and $2.0\ eV$ in Fig. 10. Note that ω_p lies between 9 and 20 eV for most of the conducting materials and that we have taken $\omega_p = 15\ eV$ to analyze the experimental data for aluminium in Section 5. Since magnitudes of $\varepsilon'_{r,D}(\Omega)$ and $\varepsilon''_{r,D}(\Omega)$ are quite high and we wanted to clearly bring out the effect of change in γ value, we have taken Ω values from 0.6 eV to 2.4 eV rather than keeping these sufficiently higher than the ω_p value. However, it must be mentioned that the value of $\varepsilon'_{r,D}(\Omega)$ changes from negative to positive at Ω = 14.99, 14.97, and 14.87 eV for $\gamma = 0.5, 1.0,$ and 2.0 eV, respectively, which are in accord with the relation

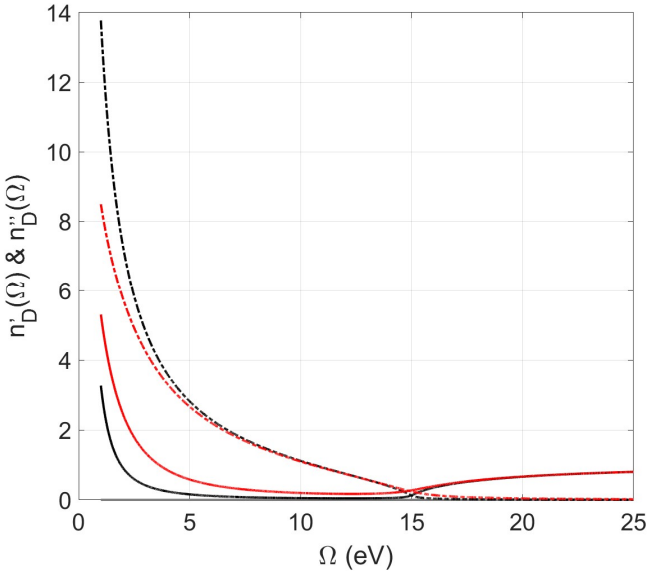

Fig. 11. Graphic representation of $n'_D(\Omega)$ (solid line) and $n''_D(\Omega)$ (dash-dot line) vs Ω for $\omega_p = 15$ eV and $\gamma = 0.5$ eV (black) and 2.0 eV (red).

$\Omega = \sqrt{\omega_p^2 - \gamma^2}$ found above. Furthermore, $\varepsilon'_{r,D}(\omega_p)$ and $\varepsilon''_{r,D}(\omega_p)$ have values 0.001 and 0.033 for $\gamma = 0.5$ eV, and 0.018 and 0.131, respectively, for $\gamma = 2.0$ eV. The corresponding values for $\gamma = 0.1$ eV are 4×10^{-5} and 0.007.

The plots for $n'_D(\Omega)$ and $n''_D(\Omega)$ vs Ω (varied from 1 eV to 25 eV) for $\omega_p = 15$ eV and $\gamma = 0.5$ and 2.0 eV have been projected in Fig. 11. These exhibit predominance of $n''_D(\Omega)$ for $\Omega < \omega_p$. However, for $\Omega > \omega_p, n''_D(\Omega) \approx 0$ and $n'_D(\Omega)$ becomes nonzero approaching 1 for $\Omega \gg \omega_p$. As mentioned in the discussion of case (iv) above, $n'_D(\omega_p)$ as well as $n''_D(\omega_p)$ are nonzero for the γ values considered here. These have values 0.131 and 0.127 for γ = 0.5 eV, and 0.27 and 0.24 for γ = 2.0 eV. However, their values for γ = 0.1 eV are 0.058 and 0.057, respectively.

The effect of γ on the variation of $R_D(\Omega)$ with Ω has been shown by plotting the graphs for $\omega_p = 15$ eV, and $\gamma = 0.0, 0.1, 0.5, 1.0,$ and 2.0 eV in Fig. 12. Here too, the presence of damping leads to

smoothing of corner and departure of the maximum reflectivity from unity. These considerations show

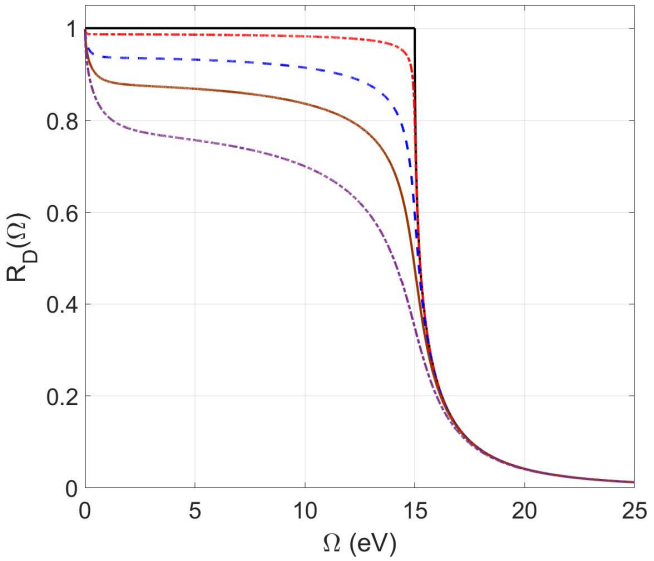

Fig. 12. Spectral dependence of $R_D(\Omega)$ for $\omega_p = 15$ eV, and $\gamma = 0.0$ (black solid line), $\gamma = 0.1$ eV (red dash-dot line), $\gamma = 0.50$ eV (blue dash-dash line), $\gamma = 1.0$ eV (brown solid line), and $\gamma = 2.0$ eV (purple dash-dot line).

that the metals are immensely reflective for the e.m. radiation with frequencies less than their respective plasma frequencies and are transparent when $\Omega > \omega_p$. This explains why metals are very good reflectors of visible light and transparent to x-rays; their ω_p values lie in the ultraviolet region. This situation is sometimes called ultraviolet transparency of metals.

It is worth mentioning that the electrons bound to the atoms in the conducting materials act as Lorentz oscillators and, therefore, analysis of their experimental data pertaining to the electrical and optical properties discussed here must be carried out employing models involving many Lorentz oscillators along with the DM. This arrangement constitutes the so-called DLOM. Furthermore, if the material contains more than one metal then expressions for different physical quantities in the DM are also modified to include more terms with appropriate values of the plasma frequencies, damping constants, and fraction of the electrons of a particular type (see, e.g. [10]).

It is pertinent to point out that the way we have introduced the many oscillators LOM in the preceding section, ω_p is fixed and $\sum_j f_j = 1$. However, while analyzing the optical spectra of materials using this model or its combination with the Drude model (the DLOM), more than one values of ω_p are used and even f_j larger than unity are employed (see, e.g. [9] and [10]).

5 Some Illustrative Applications of LOM, DM and DLOM

In this section, we demonstrate some representative applications of the formulae derived in sections 3 and 4 by considering analysis of experimental data pertaining to optical constants for a wide range of angular frequencies / photon energies in respect of materials of different types. We have directed our attention to optical properties rather than the dielectric functions because the former are themselves defined in terms of the latter and because their experimental investigation is relatively easy. Furthermore, the choice of the examples discussed has mainly been guided by the availability of easily accessible data in the literature.

Before proceeding further, it may, however, be emphasized that our aim is to illustrate the applications and not to claim the high quality of agreement between the model calculations and the experimental data. Otherwise also, as pointed out earlier too, the models discussed in this article are classical in nature and are being used for analyzing the properties which are properly understood in the framework of quantum mechanical description.

(i). Rutile (TiO_2) crystal, which is a large band-gap semiconductor, is a substance having quite a high refractive index in the visible region. It is used for the manufacture of certain optical elements, and in photocatalysis and dilute magnetism. The experimental values of $n'(\Omega)$ and $n''(\Omega)$ for Ω values from 0.83 eV to 6.20 eV have been taken

from [16] and have been used to determine corresponding $R(\Omega)$ values employing Eq. (29). All these optical parameters as function of Ω are shown in Fig. 13. It may be mentioned that $n'(\Omega)$, $n''(\Omega)$,

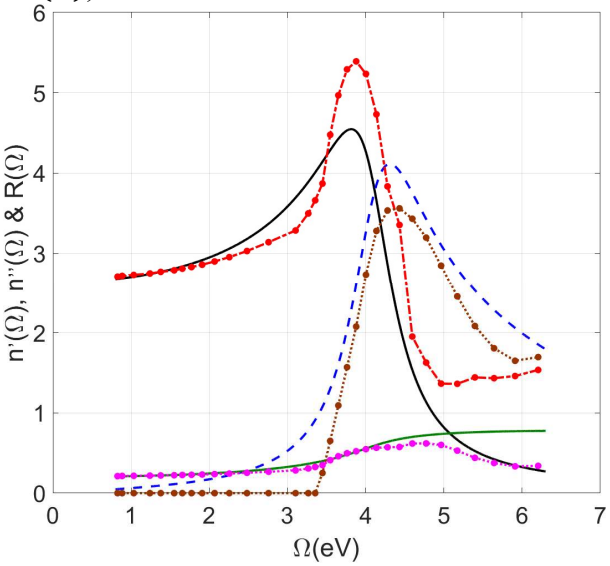

Fig. 13. A comparison of single oscillator-based LOM plots for $n'(\Omega)$ (black solid line), $n''(\Omega)$ (blue dash-dash line), and $R(\Omega)$ (dark green solid line) obtained by using $\omega_p = 10.0\,eV$, $\omega_0 = 4.1\,eV$, and $\gamma = 0.85$ eV with the experimental data [16] for $n'(\Omega)$ (red points and dash-dot line), $n''(\Omega)$ (dark brown points and dot-dot line), and $R(\Omega)$ (pink points and dot-dot line) for TiO_2 crystal.

and $R(\Omega)$ have peaks of 5.39, 3.56, and 0.62 at Ω = 3.88, 4.32, and 4.77 eV, respectively. A reasonably acceptable fit to this single-peak data using the LOM has been obtained with $\omega_p = 10.0\,eV$, $\omega_0 = 4.1\,eV$, and $\gamma = 0.85$ eV. The corresponding plots have also been included in Fig. 13. However, it may be mentioned that model calculations based on $\omega_p = 10.0\,eV$, $\omega_0 = 4.08\,eV$, and $\gamma = 0.60$ eV led to a very good fit for $n'(\Omega)$ but a poor one for $n''(\Omega)$. Similarly, a commendably good fit for $n''(\Omega)$ but not for $n'(\Omega)$ was obtained with $\omega_p = 9.40\,eV$, $\omega_0 = 4.18\,eV$, and $\gamma = 0.95$ eV. However, in both these cases the agreement between model calculations and experimental results for $R(\Omega)$ was relatively poor. In fact, these observations show that a single-oscillator model is inadequate to analyze the data for TiO_2 crystal.

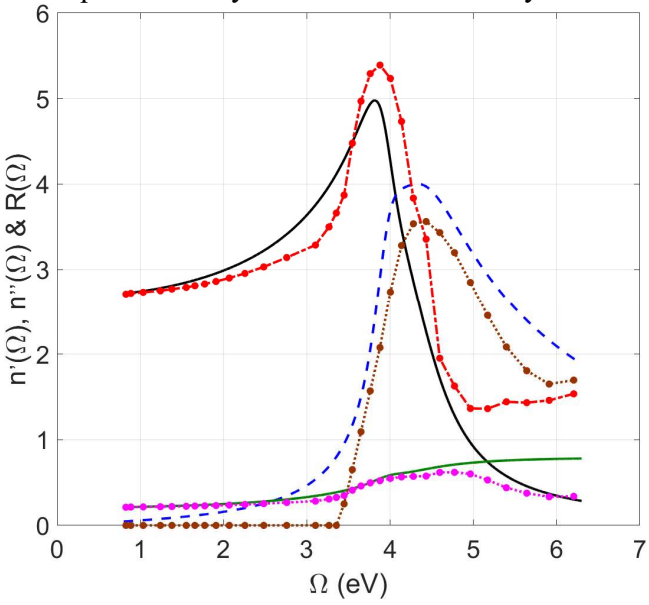

Fig. 14. Model calculations for TiO_2 crystal employing two oscillators with parameters $\omega_p = 10.30\,eV$, ω_{01} = 3.95 eV, $\gamma_1 = 0.45$ eV, f_1= 0. 30, and ω_{02}= 4.25 eV, $\gamma_2 = 1.0$ eV, f_2= 0.70. Legends for the model calculations and the experimental data are the same as in Fig. 13.

Accordingly, a two-oscillator fit was carried out and the outcome together with the parameters used is depicted in Fig. 14. Obviously, the fits are better than those displayed in Fig. 13.

(ii). Silica (SiO_2) is a well-known insulator and is used in microelectronics, in structural materials, in production of glass and optical fibers, and as an additive in the food and pharmaceutical industries. We could get experimental data for SiO_2 crystal for $n'(\Omega)$ up to Ω = 5.91 eV [16] and extracted the values for $n''(\Omega)$ for Ω up to 19.4 eV from Fig.1 in

[15]. These are projected in Fig. 15. Note that the values of $n''(\Omega)$ are close to 0 for Ω up to 8 eV and it has four peaks of magnitudes: 1.48, 1.08, 0.95, and 0.92 at $\Omega = 10.2$, 11.4, 14.2, and 17.2 eV, respectively. We have not calculated experimental $R(\Omega)$ values because of the lack of nonzero values

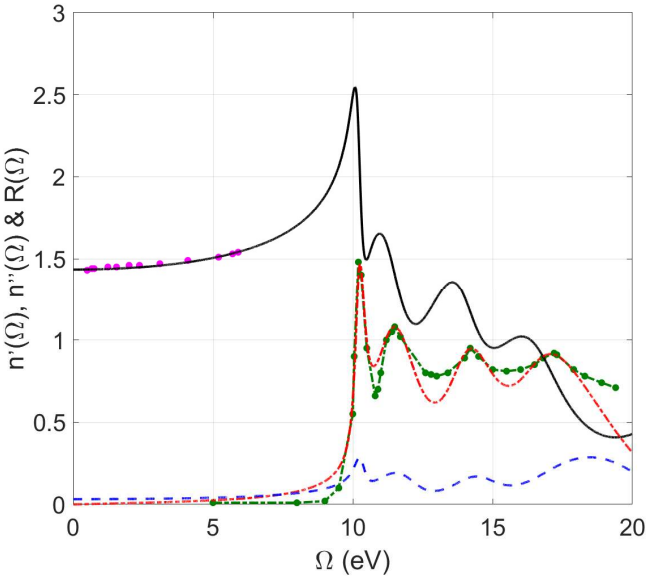

Fig. 15. Plots showing LOM fitting of available experimental data pertaining to $n'(\Omega)$ (pink points [16]) and $n''(\Omega)$ (green points with dash-dot line extracted from Fig. 1 in [15]) for crystalline SiO_2 with four oscillators having parameters $\omega_p = 13.5\,eV$, $\omega_{01} = 10.2$ eV, $\gamma_1 = 0.35$ eV, $f_1 = 0.10$, $\omega_{02} = 11.3$ eV, $\gamma_2 = 1.65$ eV, $f_2 = 0.28$, $\omega_{03} = 14.0$ eV, $\gamma_3 = 1.9$ eV, $f_3 = 0.26$, $\omega_{04} = 16.7$ eV, $\gamma_4 = 2.8$ eV, and $f_4 = 0.36$. The model-based curves are black solid line for $n'(\Omega)$), red dash-dot line for $n''(\Omega)$, and blue dash-dash line for $R(\Omega)$.

of both $n'(\Omega)$ and $n''(\Omega)$ over the same spectral range. A reasonably good fit to the data shown in Fig. 15 has been obtained using four oscillators with parameters listed in the caption to this figure. The model-based plots for $n'(\Omega)$, $n''(\Omega)$, and $R(\Omega)$ are also included in the figure. It should be possible to improve the fit by considering a higher number of oscillators.

(iii). Plots for optical parameters of alkali metals as function of Ω are quite simple and do not show any structure. These are well accounted for by DM. As typical representative of these we have displayed experimental data for reflectivity $R_e(\Omega)$ vs Ω

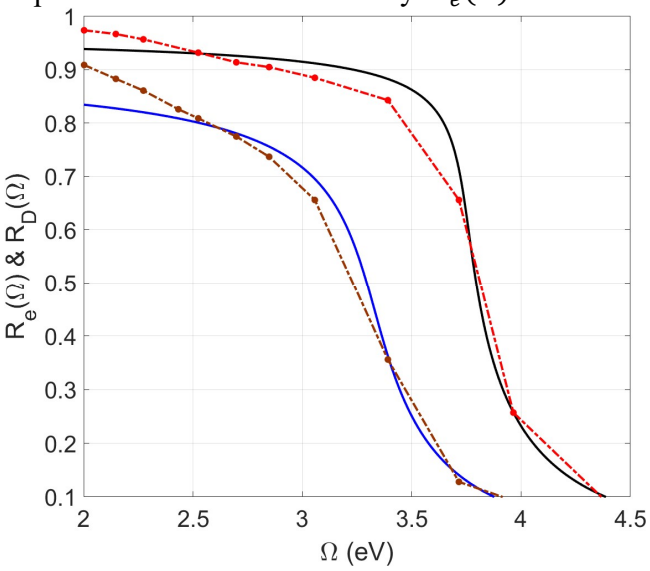

Fig. 16. Reflectance vs Ω for K and Rb. The dash-dot lines with points represent the experimental data $R_e(\Omega)$ from [17] while the full lines are for the outcome $R_D(\Omega)$ determined from the DM using parameters given in the text. The upper curves are for K and the lower ones for Rb.

graphs for potassium (K) and rubidium (Rb) reported by Monin and Boutry [17] in Fig. 16. The corresponding DM based results $R_D(\Omega)$ obtained by using $\omega_p = 3.75\,eV$, $\gamma = 0.1$ eV for K and $\omega_p = 3.32\,eV$, $\gamma = 0.24$ eV for Rb also constitute the content of this figure. The agreement between the model calculations and the experimental data for the two metals is reasonably good.

In contrast with alkali metals, optical properties of other metals like aluminium, silver, gold, copper, chromium, etc. are not explained by DM alone. These require DM combined with many-oscillator Lorentz model. As an example, we have considered aluminium (Al) because this can be safely considered as a free electron gas system

despite being a non-alkali metal. The experimental data for $n_e'(\Omega)$, $n_e''(\Omega)$, and $R_e(\Omega)$ for Ω up to 20 eV has been taken from [18] and plotted in Fig. 17. The presence of a peak in the first and dips in the last two at Ω close to 1.5 eV is quite clear. This is an

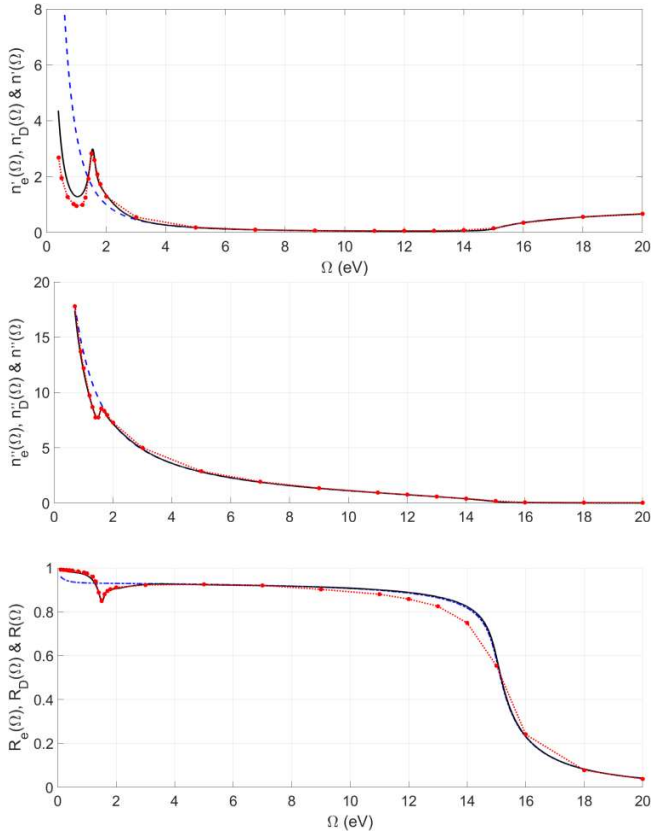

Fig. 17. Plots depicting experimental data $n_e'(\Omega)$, $n_e''(\Omega)$, and $R_e(\Omega)$ (red points joined with dot-dot line) [18]; DM fitting with $\omega_p = 15.0$ eV, $\gamma = 0.55$ eV (blue dash-dash line), and excellent DLOM fit obtained with four oscillators having parameters $\omega_p = 15.0\,eV$, $\gamma_0 = 0.04$ eV, $f_0 = 0.51$ (DM contribution), $\omega_{01} = 0.12$ eV, $\gamma_1 = 0.35$ eV, $f_1 = 0.23$, $\omega_{02} = 1.56$ eV, $\gamma_2 = 0.23$ eV, $f_2 = 0.04$, $\omega_{03} = 1.80$ eV, $\gamma_3 = 1.35$ eV, $f_3 = 0.19$, $\omega_{04} = 4.3$ eV, $\gamma_4 = 5.0$ eV, and $f_4 = 0.03$ (black solid line) for aluminium.

indication of departure from the DM behaviour, which too is shown in the figure; the parameters used to get this plot are $\omega_p = 15.0\,eV$, $\gamma =$ 0.55 eV. An impressive fit to the experimental data is obtained using DLOM with four oscillators with the parameters listed in the caption of Fig. 17; the relevant optical parameters have been denoted by $n'(\Omega)$, $n''$and $R(\Omega)$.

(iv). In ionic solids like sodium chloride, potassium chloride, rubidium bromide, etc. both cations and anions are charged and undergo vibrations about their equilibrium positions in the crystal lattice. As
such, these can be treated as Lorentz oscillators with equal and opposite charges, and mass that of the relevant ion. Obviously, masses of these oscillators are much higher, and their fundamental angular frequencies are much smaller as compared to the corresponding quantities for electronic oscillators considered in section 2. Generally, their resonant frequencies lie in the infrared region. In addition, the valence electrons of the cations as well as the anions can also be treated as Lorentz oscillators having high characteristic frequencies. Consequently, the dielectric and optical properties of these types of crystals get contributions from ionic as well as electronic oscillators and their experimental data have been analyzed using numerous-oscillators LOM. As an example, it may be mentioned that reflectance vs Ω plot for potassium chloride has about six sharp peaks with maximum value of about 0.3, and some broad peaks for Ω between 7 eV and 22 eV [3]. Obviously, its analysis will involve many Lorentz oscillators.

(v). A plasma is an electrically conducting medium having nearly equal number of positively charged ions and electrons, produced at high temperatures and / or very low number density. The ions and electrons can move around independently of each other. Since the electrons are not bound to any ion, like metals, a plasma does not have any characteristic resonant frequency, i.e., $\omega_0 = 0$. Furthermore, because of low number density (N) ω_p is quite small ($\sim 4 \times 10^{-5} - 4 \times 10^{-3}\,eV$) and the collisions of electrons are essentially negligible implying that $\gamma = 0$. Thus, a plasma essentially

corresponds to the first case discussed in Section 4. Accordingly, for a plasma $\varepsilon_r(\Omega) = 1 - \left(\omega_p/\Omega\right)^2$, which is a real quantity. Also, $n(\Omega) = \sqrt{1 - \left(\omega_p/\Omega\right)^2}$. Both of these are close to unity for very large Ω values. Note that $n(\Omega)$ is imaginary for $\Omega < \omega_p$ and real but less than unity for $\Omega > \omega_p$. Furthermore, from $\gamma = 0$ case in Fig.12, we infer that a plasma will be 100% reflective for e.m. waves of frequency $\Omega < \omega_p$ and highly transmissive for Ω significantly higher than ω_p. This is in consonance with the fact that ionosphere, which is a plasma layer around the earth having $\omega_p \sim 10^8$ rad s^{-1}, reflects back the radio signals of lower frequencies extending the range of receiving stations on the earth and is transparent to the signals with higher frequencies (the so-called short waves) enabling communication with satellites in space.

6 Epilogue

It is worth mentioning that at extremely high angular frequencies ($\Omega \to \infty$), the dielectric function is real and unity in LOM as well as DM. Physically, this means absence of polarization of the medium which is so because the electrons do not respond to the applied field. Under these conditions, there is neither refraction nor absorption and only high transmission of the incident e.m. wave.

We close the article by quoting Wooten [3], 'Both the Lorentz and Drude models are largely ad hoc, but still useful as starting points and for developing a feeling for optical properties. …many features of these classical models have quantum mechanical counterparts which are easily understood as generalizations of their classical analogs'.

Acknowledgement
The author is beholden to the learned referee for the thoughtful suggestions which have led to an overall improvement of the presentation of the article.

Appendix : Analysis of Complementary and Particular Integral Solutions for a One-dimensional Forced Oscillator

The equation of motion giving dynamical balance of forces for a one-dimensional forced damped harmonic oscillator corresponding to the one described by Eq. (1) can be written as

$$\ddot{x}(t) + \gamma\dot{x}(t) + \omega_0^2\, x(t) = Fe^{-i\Omega t}. \qquad \text{(A1)}$$

Here, $x(t)$ is instantaneous displacement, F is the amplitude of the applied force and other symbols have the same meaning as in Eq. (1). The general solution of this second-order nonhomogeneous linear differential equation with constant coefficients consists of two parts: (i) the complementary or homogeneous solution, $x_{CF}(t)$, and (ii) the particular or nonhomogeneous solution, which is also called particular integral, $x_{PI}(t)$. For an underdamped oscillator satisfying the condition $\gamma < 2\omega_0$, these solutions are given by

$$x_{CF}(t) = Ae^{-\gamma t/2} sin\,(\omega t + \theta) \qquad \text{(A2)}$$

with A as amplitude, $\omega = \omega_0\sqrt{1 - \frac{\gamma^2}{4\omega_0^2}}$ as damped angular frequency, and θ as initial phase; and

$$x_{PI}(t) = \frac{1}{(\omega_0^2 - \Omega^2) - i\gamma\Omega} Fe^{-i\Omega t}$$

$$= \left\{\frac{(\omega_0^2 - \Omega^2) + i\,\gamma\Omega}{(\omega_0^2 - \Omega^2)^2 + (\gamma\Omega)^2}\right\} Fe^{-i\Omega t}. \qquad \text{(A3)}$$

Accordingly, for the complete solution of Eq. (A1), we have

$$x(t) = x_{CF}(t) + x_{PI}(t). \qquad \text{(A4)}$$

Note that for an oscillator having initial displacement x_0 and initial velocity v_0,

$$A = \frac{\sqrt{\omega^2 {x_0}^2 + (v_0 + \frac{\gamma x_0}{2})^2}}{\omega}, \quad \text{and} \quad \theta = tan^{-1}\left(\frac{\omega x_0}{v_0 + \frac{\gamma x_0}{2}}\right). \tag{A5}$$

Also, in Eq. (A2), since $e^{-\frac{\gamma t}{2}}$ is a uniformly decreasing function of time, $x_{CF}(t)$ describes oscillations about the equilibrium position with continuously diminishing amplitude $Ae^{-\frac{\gamma t}{2}}$ till it becomes zero. Note that the oscillations $x_{CF}(t)$ are usually referred to as transients and effective or damped amplitude $Ae^{-\frac{\gamma t}{2}}$ is said to define the envelope of decay of $x_{CF}(t)$. Obviously, the decrease in amplitude is fast if γ is large and vice versa. To appreciate the effect of damping parameter γ on $x_{CF}(t)$ in a better way, we note that $Ae^{-\frac{\gamma t}{2}}$ will be 0.1 % of A at time $T = \frac{-2 \ln (0.001)}{\gamma} = \frac{13.82}{\gamma}$. Thus, for $t > T$, $Ae^{-\frac{\gamma t}{2}}$ and hence $x_{CF}(t)$ may be essentially taken as zero.

Next, simplifying Eq. (A3), we can write its real part as

$$x'_{PI}(t) = B\cos(\Omega t - \varphi), \tag{A6}$$

where

$$B = \frac{F}{\sqrt{\left(\omega_0^2 - \Omega^2\right)^2 + (\gamma\Omega)^2}}, \text{ and } \varphi = tan^{-1}\left(\frac{\gamma\Omega}{\omega_0^2 - \Omega^2}\right). \tag{A7}$$

In fact, this is the same expression as we obtain by considering the nonhomogeneous term as $F\cos(\Omega t)$ in Eq. (A1). Clearly, $x'_{PI}(t)$ is an oscillatory function with constant amplitude B.

From experimental observation point of view, a complete solution for Eq. (1) can be written as

$$x(t) = x_{CF}(t) + x'_{PI}(t). \tag{A8}$$

As argued above, for sufficiently large times $t > T$, the transients vanish and only the particular solution is left, and we have

$$x(t) = x'_{PI}(t). \tag{A9}$$

This is said to give a steady state solution to the problem.

To elaborate this aspect in a proper perspective, we have plotted $x_{CF}(t)$, $x'_{PI}(t)$, and $x(t) = x_{CF}(t) + x'_{PI}(t)$ for a damped forced oscillator characterized by (arbitrarily chosen) parameters ω_0 = 4.0 rads^{-1}, γ = 1.0 s^{-1}, x_0 = 0.03 m, v_0 = 0.50

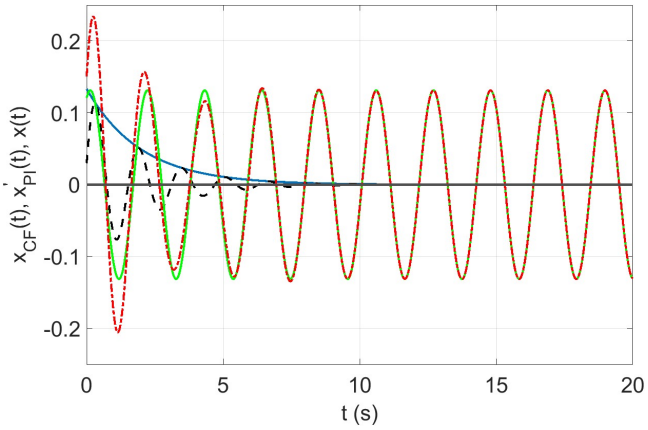

Fig. A1. Plots showing time variation of $x_{CF}(t)$ (black dashed line), $x'_{PI}(t)$ (green solid line), and $x(t)$ (red dash-dot line) for a forced oscillator having parameter values listed in the text. Blue solid line represents the envelope of decay of $x_{CF}(t)$.

ms^{-1}, F = 1.0 N, and Ω = 3.0 rads^{-1} so that ω = 3.97 rads^{-1}, A = 0.13 m, θ = 0.23 rad, B = 0.13 m, and φ = 0.40 rad, in Fig. A1. This clearly shows that for small t values $x(t)$ gets contribution from both $x_{CF}(t)$ and $x'_{PI}(t)$, while for reasonably large times $(t > T = 13.82\ s)$ $x_{CF}(t) = 0$ and $x(t) = x'_{PI}(t)$, the steady state solution. We can extend this treatment straightaway for a forced one-dimensional harmonic oscillator to the case of relevant three-dimensional oscillator.

References

[1] The Nobel Foundation, *Nobel Lectures - Physics 1901-1921,* (Elsevier, Amsterdam, 1967).
[2] H. A. Lorentz, Proc. Koninklijke Akademie van Wetenschappen (Netherlands) **8**, 591 (1906).
[3] F. Wooten, *Optical Properties of Solids,* (Academic Press, New York, 1972).
[4] I. F. Almog, M.S. Bradley, and V. Bulovic, The Lorentz Oscillator and its Applications, https://ocw.mit.edu>resources>mit6_007s11_ lorentz (2011).
[5] A. Zangwill, *Modern Electrodynamics*, (Cambridge University Press, Cambridge, 2012).
[6] M. J. Mageto, C. M. Maghanga, and M. Mwamburi, Afr. Rev. Phys. **7:0011,** 95 (2012).
[7] D. J. Griffiths, *Introduction to Electrodynamics*, (Pearson, London, 2013).
[8] P. Hofmann, *Solid State Physics: An Introduction,* (Wiley-VCH, Weinheim, 2015).
[9] R. C. Rumpf, *Electromagnetic Properties of Materials – Lorentz and Drude Models, https://*empossible.net/wp-content/uploads/2018/ 03/Lecture-2-Lorentz-and-Drude-models.pdf (2016)
[10] D. Marasinghe, *Drude-Lorentz Analysis of the Optical Properties of the Quasi-two-Dimensional Dichalcogenides 2H-$NbSe_2$ and 2H-$TaSe_2$*, https://etd.ohiolink.edu›rws_etd›send_file›send (2018).
[11] Ph. W. Courteille, *Electrodynamics*, https://www.ifsc.usp.br ›ElectroDynamicsScript (2021).
[12] J. S. Colton, Lorentz Oscillator Model, http://www.physics.byu›docs›phy442-summer21 (2021).
[13] J. Zhu, J. Zhang, Y. Li, and others, AIP Advances **5**, 117217 (2015).
[14] J. Zhang, K. Li, Z. Fang, and others, AIP Advances **11**, 075218 (2021).
[15] A. R. Forouhi and I. Bloomer, J. Phys. Common. **5**, 025002 (2021).
[16] http://www.filmetrics.com/refractive index data base.
[17] J. Monin and G. A. Boutry, Phys. Rev. B **9**, 1309 (1974).
[18] H. J. Hagemann, W. Gudat, and C. Kunz, DESY SR-74 / 7 (1974).